NGT-21-002-080
NGT-80001

AERONAUTICS

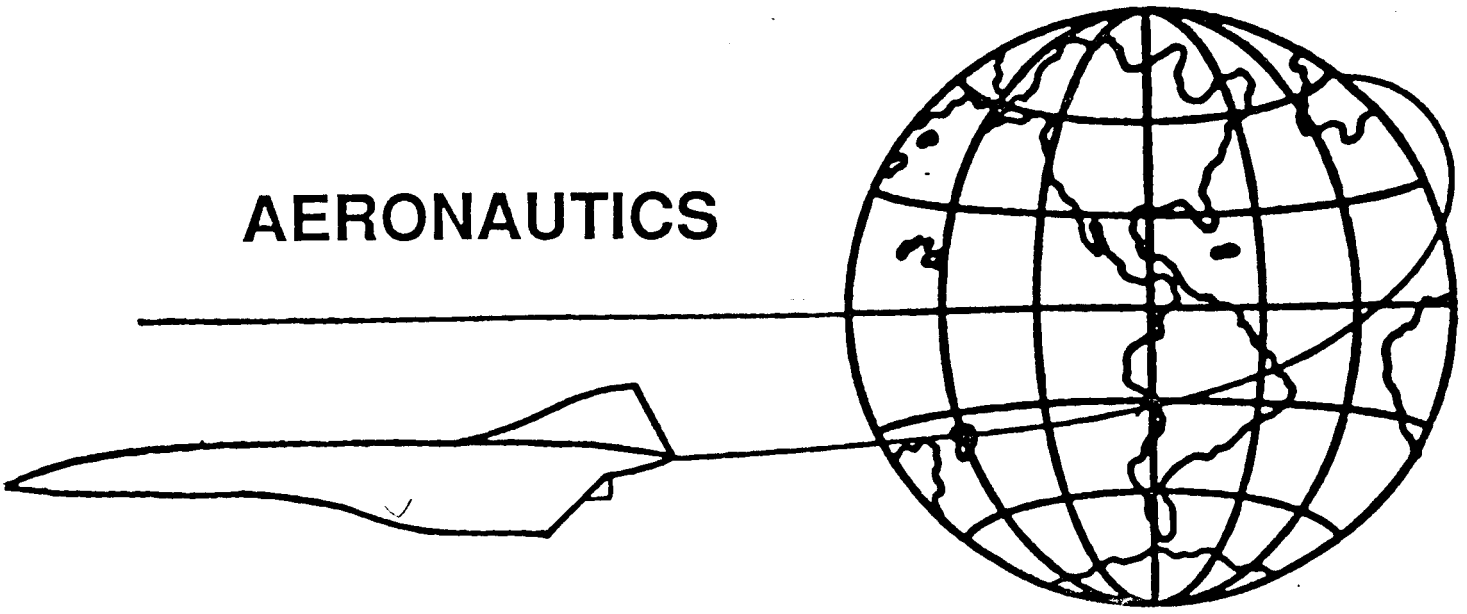

CALIFORNIA STATE POLYTECHNIC UNIVERSITY, POMONA

NASA / USRA ADVANCED DESIGN PROGRAM

JUNE 11, 1988

VOLUME 1

NASA / USRA ADVANCED DESIGN PROJECT

California State Polytechnic University, Pomona
Aerospace Engineering Department

Final Report 1987-1988

Volume I

THE FLYING DIAMOND

A Joined Aircraft Configuration Design Project

Design Team Members:

Chris Ball — Project Leader
Joe Czech
Bryan Lentz
Daryl Kobashigawa
Curtis Oishi
David Poladian

1.0 Introduction

The aircraft design course at the California State Polytechnic University, Pomona (CSPUP) during the 1987-1988 academic year participated in the design program funded and assisted by both the Universities Space Research Association (USRA) and the National Aeronautics and Space Administration (NASA) to independently investigate the planform effects of four different configurations on a high speed civilian transport (HSCT) aircraft. The four different configurations under investigation were:

(1) Joined Wing
(2) Oblique Wing
(3) Caret
(4) Blended-Wing-Body

The management of the progress of the aircraft's design was accomplished by means of a "Matrix Management". Each student in the design class belonged to two different design teams. According to his or her particular field of interest, a student was assigned to an academic discipline and to one of the above aircraft configurations. The four academic disciplines were:

(1) Aerodynamics
(2) Propulsion
(3) Noise and Pollution
(4) Structures and Heat Transfer

Team leaders were elected by the design course members to manage the progress of each of the individual aircraft configurations. The matrix management program allowed individual team members to develop a better understanding of the mechanics by which the aircraft design process blends together the different areas of engineering, while at the same time, further develop the technical background in his or her field of interest.

This report consists of the results of the analysis conducted on the Joined Wing Configuration. The design team for the Joined Wing configuration consisted of six (6) students, two from the Aerodynamics group, two from the Propulsion group and one each from the Noise and Pollution group and the Structures and Heat Transfer group. The design course extended over two academic quarters for a total of twenty weeks.

1.1 Mission Requirements and RFP

The RFP selected for the Joined Wing configuration was based upon an indepth study of current industry and NASA investigations upon the requirements necessary for a sucessful HCST aircraft. The RFP called for the design of a civilian transport aircraft capable of meeting the following restrictions:

Purpose	Commercial Transport
Payload	250 Passengers + Luggage
Range	6,500 Nautical Miles
Speed	Mach 3 - 6
Operating Field Limitations	11,500 Feet (Existing Airfields)
Maximum Weight	1,000,000 Pounds
Turn Around Time	1 Hour

The mission details (cruise altitude, and speed, transonic flight, etc) were not specified within the RFP, and these parameters were allowed to change to maximize the performance of each individual planform configuration. In addition to the above requirements, the existing regulations concerning transcontential flight, supersonic flight, passenger safety, noise, pollution and economics were considered during the design of the Joined Wing Configuration. The regulations concerning the airworthiness of commercial transport aircraft are under the jurisdiction of the Federal Aviation Administration (FAA). The Federal Aviation Regulation (FAR) which serves as a guideline for the standard of current day transport aircraft is Part 25 (Reference 8). This document also served in part to establish the mission requirements during the design of the Joined Wing Aircraft.

1.2 The Joined Wing Configuration

The joined wing configuration is an entirely new aircraft configuration originally envisioned by NASA and ACA Industries during the early 1980's. This aircraft employs a conventional fuselage and incorporates two wings joined together near their tips to form a diamond shape in both the plan view and the front view. Figure 1-1 shows the Joined Wing in three different views, illustrating the wing structure trademark. The motivation for the concept originated within the structures and aerodynamics disciplines. (Reference 47)

This novel arrangement of the lifting surfaces uses the rear wing as a horizontal tail and as a forward wing strut. The rear wing has its root at the tip of the vertical stabilizer and is structurally attached to the trailing edge of the forward wing. The attachment may occur at the tip of the forward wing or may be placed inboard. This arrangement of the two wings forms a truss structure which is inherently resistant to the aerodynamics bending loads

generated during flight. This allows for a considerable reduction in the weight of the lifting surfaces of the Joined Wing configuration.

The structural arrangement of the two wings create additional aerodynamic benefits. With smaller internal wing structures needed, the Joined Wing may employ thinner wings which are more suitable for supersonic and hypersonic flight, having less induced drag than conventional cantilever winged aircraft. Inherent in the Joined Wing configuration is also the capability of the generation of direct lift and side force, and thus, the performance characteristics may be greatly enhanced.

2.0 List of Symbols

α	Bypass Ratio	(--)
γ	Flight Path Angle	(Deg)
γ	Ratio of Specific Heats	(--)
μ	Coefficient of Friction	(--)
θ	Ray-Path Azimuth Angle	(Deg)
θ	Total to Static Temperature Ratio	(--)
ρ	Ambient Air Density	(Slugs/ Cu Ft)
σ	Dynamic Pressure Ratio	(--)
τ	Total Temperature Ratio	(--)
a	Acceleration of Air in Engine	(Feet / Square Second)
a_o	Free Stream Speed of Sound	(Feet / Second)
a_v	Speed of Sound at Altitude	(Feet / Second)
b	span	(Feet)
b_F	Front Wing Semi-span	(Feet)
b_R	Rear Wing Semi-span	(Feet)
c	Airfoil Cord Length	(Feet)
c_p	Specific Heat	(BTU / Slug Second)
d	Diameter of Engine	(Feet)
dP	Rise in Pressure	(Pounds / Square Feet)
e	Wing Planform Efficiency Factor	(--)
f	Frequency	(Hertz)
g	Gravity	(Feet / Second)
h	Altitude	(Feet)
l	Length of Engine	(Feet)
q	Dynamic Pressure ($=\frac{1}{2}\rho V^2$)	(Pounds / Sq Ft)
t	Airfoil Thickness	(Feet)
u	Air Velocity in Engine	(Feet / Second)
A	Inlet Capture Area	(Square Feet)
D	Drag	(Pounds Force)
E	Endurance Time	(Minutes)
F	Force Generated by Engine	(Pounds)

H	Atmospheric Scale Height	(Feet)
I	Specific Impulse	(Seconds)
K	Wing Drag Due To Lift Factor	(--)
L	Lift	(Pounds Force)
L	Aircraft Length	(Feet)
M	Mach Number	(--)
P	Pressure	(Pounds / Square Feet)
R	Range of Aircraft	(Feet)
S	Planform Area	(4615 Square Feet)
T	Thrust	(Pounds)
V	Aircraft Velocity	(Feet / Sec, or Knots)
W	Aircraft Weight	(Pounds)
C_{D_0}	Zero Lift Drag Coefficient	(--)
C_L	Lift Coefficient	(--)
Cj	Specific Fuel Consumption	(Pounds / Pounds - Hour)
H_G	Altitude of Ground Above Sea Level	(Feet)
K_L	Lift Shape Factor	(--)
K_P	Pressure Amplification Factor	(--)
K_R	Reflectivity Factor	(--)
K_V	Volume Shape Factor	(--)
L_W	Aircraft Length	(Feet)
P_G	Ground Atmospheric Pressure	(Pounds / Square Feet)
P_v	Pressure at Altitude	(Pounds / Square Feet)
S_{AM}	Maximum Cross Sectional Area	(Square Feet)
T_r	Thrust Required at Cruise	(Pounds)

SUBSCRIPTS:

A	Approach
a	Afterburner
B	Component Due to Base Drag
c	Compressor
f	Forward Wing
F	Final
FL	Field Length
GTO	Gross Take-Off
I	Inital
L	Component Due to Lift
max	Condition of the parameter maximum value
o	Condition in the Free Stream
p	Component Due to Pressure Drag
r	Rear Wing
ref	Reference
Stall	Stall Condition
t	Turbine
TO	Take-Off
V	Component Due to Volume
wave	Component Contributed by Wave Drag
wet	Quantity Refering to Total Exposed Area

3.0 Aircraft Sizing Methods

3.1 Mission Profile

The initial design process began with the selection of the mission profile. This mission profile needed to meet all of the requirements set forth in the RFP and be compatible with the FAR requirements. The mission profile selected for the Joined Wing Configuration is shown in Figure 3-1. As the design process progressed the details of the entire mission profile changed to optimize several performance parameters of the Joined Wing aircraft. The following sections describe the design process and the evolution of the mission profile selected and shown here.

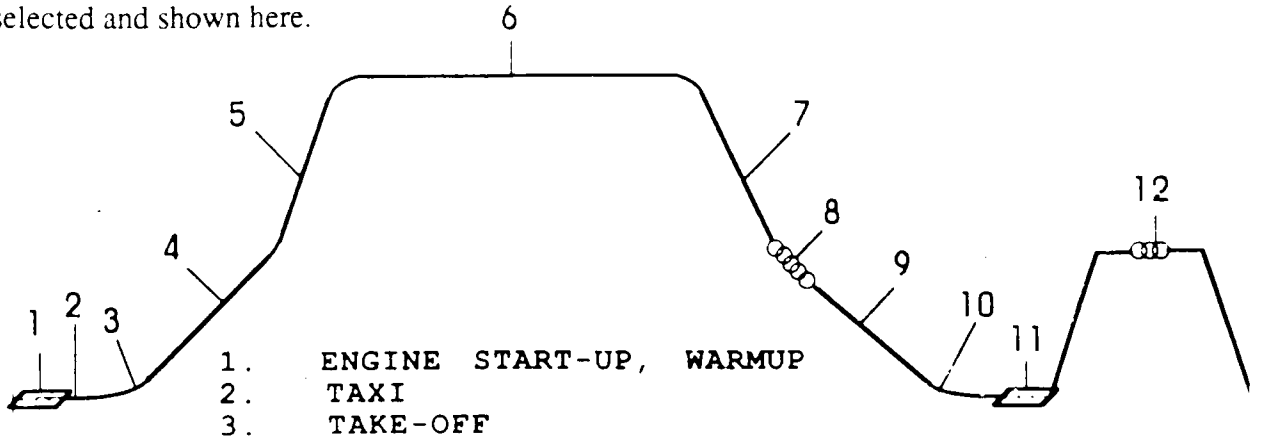

1. ENGINE START-UP, WARMUP
2. TAXI
3. TAKE-OFF
4. CLIMB TO MACH = 1.0
5. CLIMB TO CRUISE MACH AND ALTITUDE
6. CRUISE
7. DESCEND TO SUB-SONIC LOITER
8. 30 MINUTE SUB-SONIC LOITER
9. DESCEND TO LAND
10. LANDING
11. 5% FUEL RESERVES (FAR REQUIREMENT)

FIGURE 3-1

3.2 Fuel Weight Estimation

The sizing of the aircraft began with the initial take-off weight estimation. This gross take-off weight (W_{GTO}) estimation was then used to initially size the aircraft planform area and establish preliminary structure requirements. The take-off weight was broken down into three distinct categories: W_{Fuel}, W_{Fixed}, W_{Empty}. Each of these categories will now be considered and defined.

Fixed Weight: The fixed weight is comprised of the crew and equipment, passengers with luggage, and in-flight refreshments. Following the guidelines set in FAR 95.215 the minimum number of cabin members (flight attendants) must be two for the first 100

passengers, and one for every 50 passengers over 100. The capacity of the Joined Wing at 268 passengers required 6 cabin crew members. The cockpit was designed to accommodate two pilots and one observer. The total number of crew required was therefore determined to be nine. The weight for each crew member, by FAR regulation, is 215 pounds (175 + 40 for baggage). The weight allocated for each passenger is also 215 pounds (175 + 40 for baggage and in-flight refreshments). The total fixed weight is therefore:

$$W_{Fixed} = (\text{passengers + crew})*(\text{allocated weight/person}) =$$
$$W_{Fixed} = (268 + 9)*(215) = \underline{59,555 \text{ Lbs}}$$

Empty Weight: The use of historical data supplied an initial estimate for the aircraft empty structural weight (final calculations are incorporated in the final weight estimation, see section 3.2). According to Roskam (Ref 14) and Nicolai (Ref 11) there exists a linear relationship between the gross take-off weight and the empty weight for a conventional metal structured aircraft. The RFP for this current design established a weight limitation of 1,000,000 pounds, so the initial gross take-off weight used was 950,000 pounds. Using data supplied in Nicolai and Roskam, describing trends in similar heavier transports, an estimate for W_{Empty} of 400,000 pounds was used.

Fuel Weight: A preliminary estimate of the fuel required for the mission profile was accomplished by analyzing each of the eight segments of the entire aircraft mission. The eight segment mission profile was as follows:

1. Engine start-up and warm-up
2. Taxi to runway
3. Take-off
4. Accelerate and climb to cruise conditions
5. Cruise
6. Loiter (30 minutes)
7. Descent
8. Landing, taxi, shut-down

The calculation of the ratio of the initial weight to the final weight of each segment was determined. The product of all eight ratios will represent the total weight change due to the burning of fuel during the complete mission profile. The first three segments of the mission were mission profile independent and have been observed to be generally constant for the commercial transport class of aircraft (Nicolai Reference 11 and Roskam Reference

14). The following summary of the first three segments uses the historical trends presented in Nicolai:

Segment 1 - Engine start-up and warm-up:

$$(\frac{W_F}{W_I})_1 = 0.99$$

Segment 2 - Taxi to Runway:

$$(\frac{W_F}{W_I})_2 = 0.995$$

Segment 3 - Take-Off (Climb to 50 Feet):

$$(\frac{W_F}{W_I})_3 = 0.995$$

Segment 4 Accelerate and Climb to Cruise Conditions:

Using Reference 11, Nicolai Figure 5•6 based upon historical data trends (and assuming a 25% improvement in the fuel consumption with increasing efficiency based on future technology) the weight fraction for the climb-acceleration phase is :

$$(\frac{W_F}{W_I})_4 = 0.93$$

Segment 5 - Cruise:

Using the Brequet range equation, the relationship between range and fuel consumption in terms of (L/D), specific fuel consumption and cruise velocity is expressed as:

$$R = (\frac{V}{Cj})_{CR} (\frac{L}{D})_{CR} \ln (\frac{W_F}{W_I})_5$$

The range of our cruise is 4900 nautical miles (5635 statute miles) as defined in the mission profile. The specific fuel consumption (Cj) for preliminary estimations was set at 1.2 (see section 8.2.2). The L/D for cruise was established using the trends of values for similar aircraft weights and aspect ratios. Nicolai presented this data (Figure 5•6, Reference 11), and the trend indicates that the L/D above Mach 4.0 approaches 4.0. Thus an $(L/D)_{max}$ of 3.75 was used for this analysis. Finally we can solve for the weight fraction:

$$(\frac{W_F}{W_I})_5 = 0.43$$

Segment 6 - Loiter for 30 Minutes:

The Brequet endurance equation (Nicolai, Page) may be used to determine the fuel weight fraction used during the aircraft's loiter:

$$E = (\frac{1}{Cj})(\frac{L}{D})\ln (\frac{W_F}{W_I})_6$$

Assuming that the aircraft will loiter at 75% of its cruise specific fuel consumption and a $(L/D)_{max} = 4.0$ the weight fraction for the loiter segment becomes:

$$(\frac{W_F}{W_I})_6 = 0.894$$

Segment 7 - Descent:

References Nicolai (reference 11) and Roskam (Reference 14, Table 2•1) include data for weight fractions during aircraft descent using historical trends:

$$(\frac{W_F}{W_I})_7 = 0.985$$

Segment 8 - Landing, Taxi, and Engine Shut-down:

Roskam (reference 14, Table 2•1) supplies data for commercial transport aircraft:

$$(\frac{W_F}{W_I})_8 = 0.990$$

Reserves and Trapped Fuel:

The mission requirements set forth in FAR 25 require that 5% of the fuel required for the mission be kept aboard and cannot be used for range consideration. It was assumed that approximately one percent of the mission fuel is trapped and not available for use (Nicolai, Reference 11, Page 5-12).

Total Mission Fuel Requirements:

$$(\frac{W_{Final}}{W_{TO}}) = (\frac{W_F}{W_I})_1(\frac{W_F}{W_I})_2 \cdots\cdots (\frac{W_F}{W_I})_8 (1 + \text{Trapped} + \text{Reserves})$$

$$(\frac{W_{Final}}{W_{TO}}) = .3814$$

The total fuel required (by weight) for the Joined Wing mission profile was therefore:

$$(W_{Fuel}) = 342{,}247 \text{ Pounds}$$

The fuel weight breakdown according to mission segment is expressed graphically in Figure 3-2

3.3 Component Weight Determination:

The component weights of the aircraft were determined using the method outlined in reference 18. Since the method used equations applicable to conventional, aluminum-skinned aircraft and since the Joined Wing does not fall in that category, studies done in Reference 11 were utilized in conjunction with the weight equations to predict the weight of the joined wing. Specifically, the equations utilized were the ones which could adopt factors to further predict the weight of non-conventional aircraft. According to Reference 47 weight savings of up to 25% could be accomplished over conventional type of aircraft. This was used to predict the correct weight of the front and rear wings. Also, the rear wing was treated as a horizontal tail.

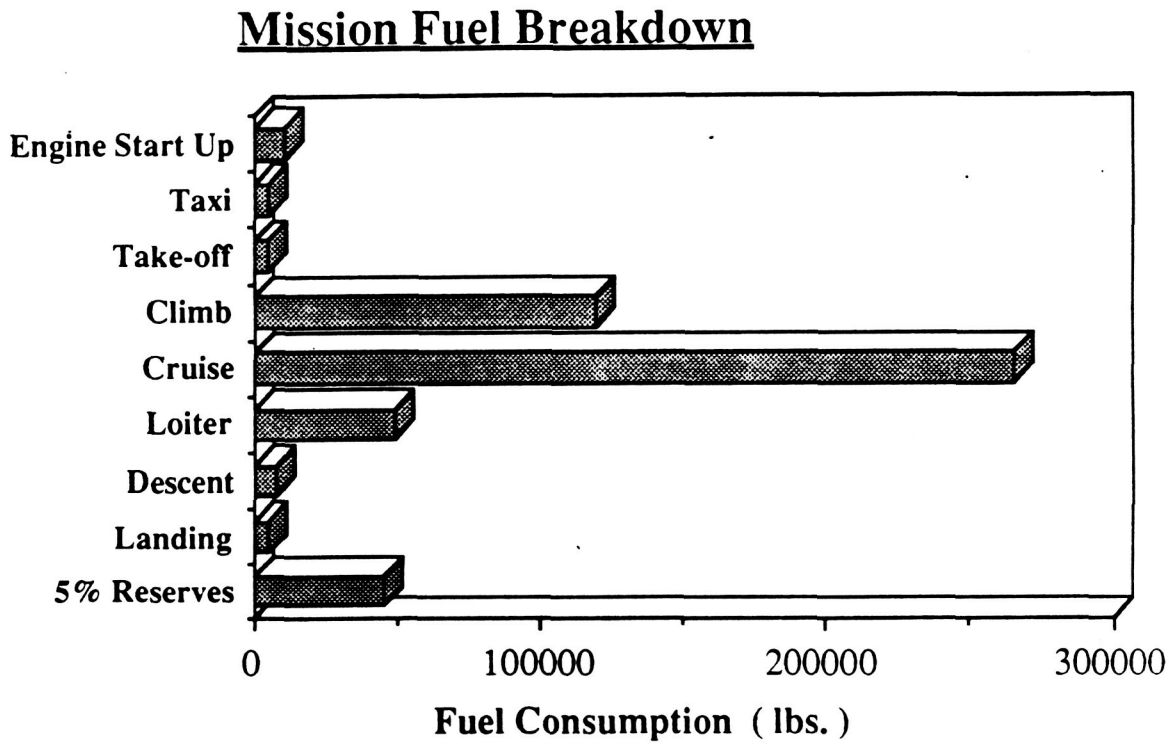

FIGURE 3-2

Since titanium will be used as a prinary material, a factor of 1.1 was introduced to account for the increased weight. The following were the component weights that were obtained.

COMPONENTS	WEIGHTS
Wing	202674.7
Fuselage	157309
Rear wing	10201
Vertical tail	7691
Landing gear	19130
Cowl/Duct weight	3172
Self-Sealing bladder cells	13736
Fuel system bladded cell backing and supports	3371
C.G. control system	652
Engine controls	249
Engine starting system	321
Surface controls,hydraulics, pneumatics	7463
Flight instrument indicators	89
Engine instrument indicators	41
Miscellaneous indicators	137
Electrical systems	5152.6
Flight deck seats	275
Passenger seats	8104
Lavatories and water prov.	487
Food provisions	501
Oxygen system	355
Cabin windows	686
Baggage and cargo handling provisions	997
Miscellaneous furnishings and equipment	706
Air conditioning and anti-icing	6033
Fuel	342247
Fixed weight	59555
Empty weight	558185
Total weight	900432

3.4 Configuration Sizing

3.4.1 Sizing Chart Summary:

The sizing chart which allowed for the determination of the preliminary design of the aircraft wing loading and the aircraft planform area was created using the data for three different portions of the mission profile. Take-off, landing and cruise conditions were all examined to best size the configuration see Figure 3-3.

Take-Off Sizing Requirements:

Reference 19, eqn 3-8 states that the take-off distance is proportional to the wing loading and inversely related to the aircraft thrust to weight ratio. Assuming a take-off distance of 11,500 feet (as determined by the RFP) the relationship between the take-off lift coefficient, thrust to weight ratio and the wing loading was expressed as:

$$\left(\frac{T}{W}\right)_{TO} = \frac{37.5\,(W/S)_{TO}}{S_{TO}\,\sigma\,C_{L_{max}}}$$

This equation may be graphically expressed on a sizing chart. Figure 3-3 is the sizing chart for the Joined Wing Configuration. The lines of constant C_{Lmax} illustrate the design requirements for the aircraft wing loading and thrust to weight ratio. The criteria to be met is shown by the shaded region fo the graph (ie: the requirement is met if the (T/W) and (W/S) are such that they are on the unshaded side of a given C_{Lmax} line).

Landing Sizing Requirements:

The requirements set forth in the Federal Aviation Regulations Part 25 for commercial civilian transport aircraft states that the landing field length be proportional to square of the approach velocity as:

$$S_{FL} = 0.3(V_A)^2$$

Thus, the approach speed for the joined wing configuration based on a operating field length of 11,500 feet was determined to be 195 knots (or 328 fps). The FAR requirement also states that the approach speed must be 130% that of the stall speed. Thus, the stall speed of the aircraft was determined to be 253.8 fps or 150.5 knots. Reference 11 (Page 3-6, eqn 6-1) discussed the wing loading relationship to the stall velocity for landing, and the resulting equation was:

$$\frac{W}{S} = \frac{1}{2}\rho V^2 C_{Lmax}$$

Assuming a standard sea level atmosphere, the landing requirements was then placed on the sizing chart. The vertical lines are the wing loading at a selected range of constant C_{Lmax} based upon the stall speed determined above.

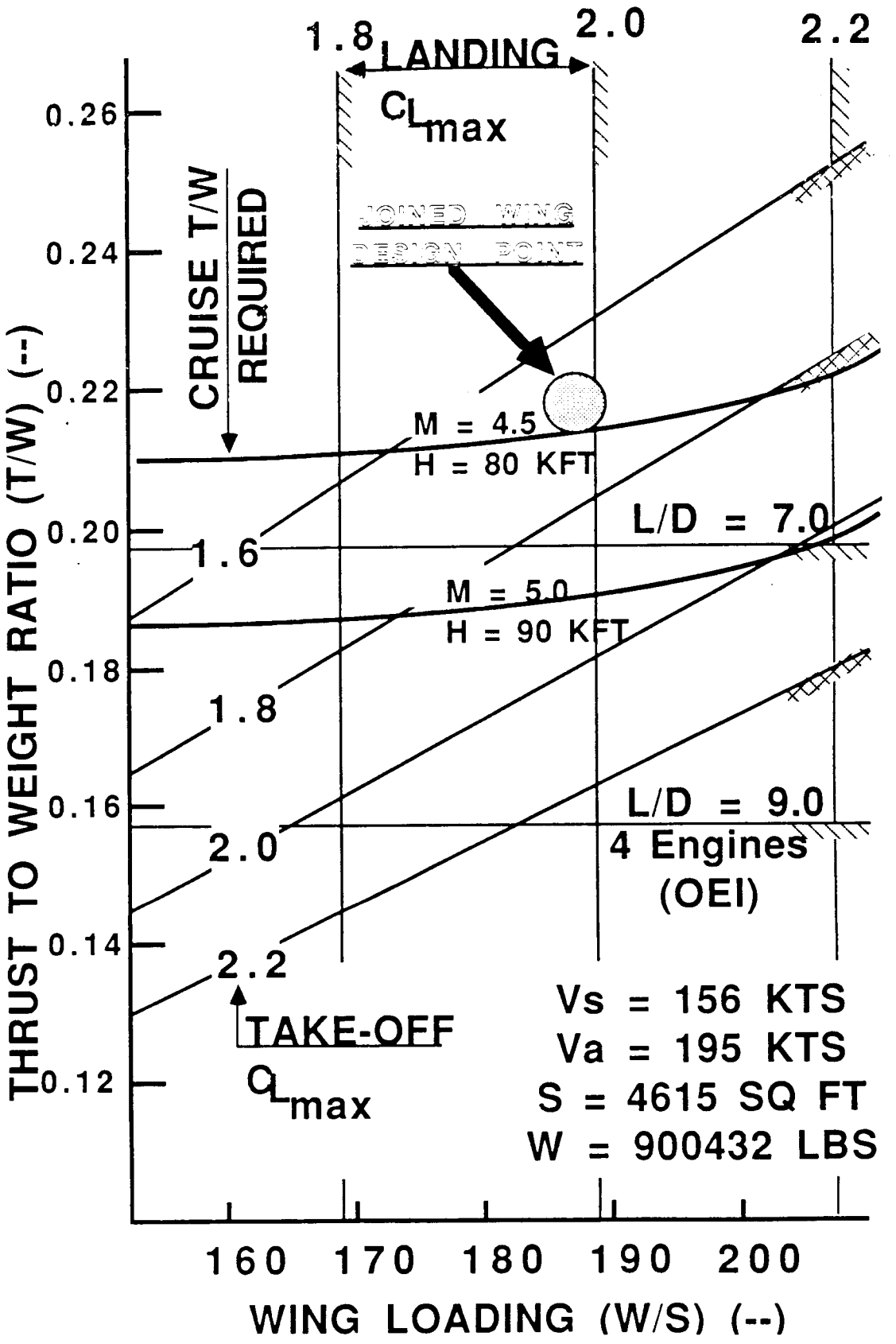
1.8
LANDING
2.0
2.2
$C_{L_{max}}$
JOINED WING
DESIGN POINT
CRUISE T/W
REQUIRED
0.26
0.24
0.22
0.20
0.18
0.16
0.14
0.12
THRUST TO WEIGHT RATIO (T/W) (--)
M = 4.5
H = 80 KFT
L/D = 7.0
1.6
M = 5.0
H = 90 KFT
1.8
L/D = 9.0
4 Engines
(OEI)
2.0
2.2
TAKE-OFF
$C_{L_{max}}$
Vs = 156 KTS
Va = 195 KTS
S = 4615 SQ FT
W = 900432 LBS
160
170
180
190
200
WING LOADING (W/S) (--)

Balked Landing Requirements (Landing Climb):

The landing requirements as set by FAR 25 state that the aircraft must meet the following requirements with one engine operating (OEI). (Roskam, Reference 19, eqn 3-31a):

$$\frac{T}{W} = [\frac{N}{N+1}] [(L/D)^{-1} + CGR]$$

Where N is the number of engines and CGR is equal to 0.021 (Roskam, Reference 19). These values may be presented on the sizing chart as lines of constant (L/D). For all engines operating the requirements are:

$$\frac{T}{W} = [(L/D)^{-1} + CGR]$$

Where CGR is 0.032. The shaded side of these lines is where the balked landing requirement is not met.

4.0 Configuration Development

4.1 Introduction

Before the designing of the plane began, much research on the Joined Wing configuration concept was necessary due to the lack of knowledge about the qualities and characteristics of this relatively new airplane configuration. As a result, many papers were gathered on the joined wing concept that were written by its pioneer, Julian Wolkovitch. Through the many suggestions and experimental results contained in these reports, the Joined Wing HSCT was designed.

4.2 Initial Planform Selection

One of the primary considerations when designing a plane of this size was trying to keep the weight down to a reasonable amount. Keeping this in mind, the placement of the point joining the front and rear wings was decided to be put at a point where the wing weight would be at its minimum. Through parametric studies, this point occurred when the span of the rear wing was 70% of the span of the front wing as in Figure 4-1 (Wolkovitch, Overview, ref. 47). By doing this, the weight savings in comparison to a conventional wing-body configuration was close to 25% (Wolkovitch, Overview, ref. 47) due to the natural truss-system that joined wing systems develop, they make the wings effictively stiffer than conventional cantilever wings. Thus with the higher natural stiffness, the amount of material needed in the box beams of the wings decreases in order to support the same aerodynamic loads. This higher stiffness also allowed the use of thinner airfoil sections for the wings which brought another positive aspect: less wave drag.

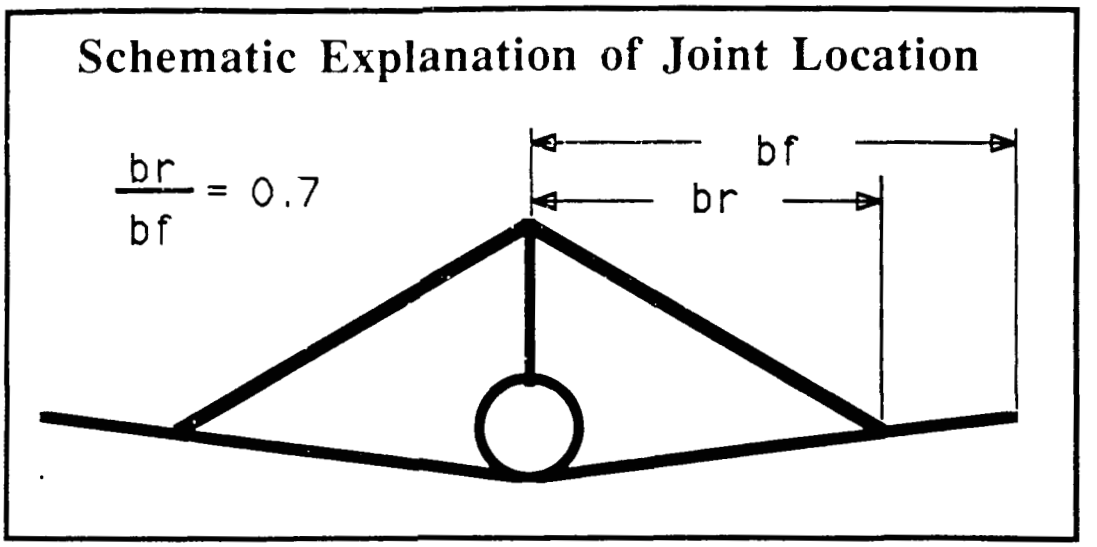

FIGURE 4-1

The way in which the front and rear wings were connected was in such a way that the wings did not overlap in a top view of the planform as in Figure 4-2. The reason for this was that if wings did overlap in top-view, then the narrow region between the front and rear wings would cause a venturi effect which would increase the parasite drag (Wolkovitch, Overview, ref. 47).

The position of the top of the vertical tail where the rear wings were connected had to be decided. As for the vertical placement, it was advantageous to put the rear wing/vertical tail joint as high as possible from the body for two reasons. First, span-efficiency factor increase as the vertical gap between the front and rear wing roots increase (Wolkovitch, 84-2471, ref. 50). Thus, for induced drag purposes, it was better to have a rather tall tail. Secondly, a large centerline gap reduces the effective de/da at the rear wing and thus ultimately increases the maximum lift coefficient (Wolkovitch, Overview, ref. 47). As for the longitudinal placement, the rear wing/vertical tail joint was placed further forward in relation to the wing joint location which effectively decreased the forward sweep of the rear wing. This was done to reduce the ratio of front wing lift curve slope to rear wing lift curve slope. In the event of an airplane stall, this reduced ratio would help the forward wing to stall before the rear wing which is a favorable dynamic stability characteristic (Wolkovitch, Overview, ref. 47).

Explanation of Forward Wing/Body Connection and Rear Wing Joint Location

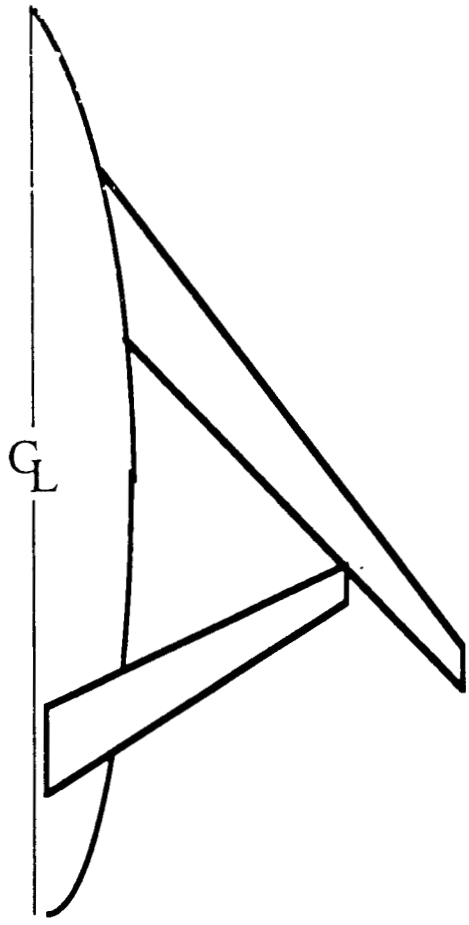

FIGURE 4-2

The reasoning for the connection placement of the front wing to the body was for subsonic and supersonic drag reasons. During subsonic flight, the flow tends to separate at this wing body intersection if the body is at its maximum cross-sectional area, but tends not to separate if this intersection is at a point where the body is still increasing in cross-sectional area (Wolkovitch, Overview, ref. 47), therefore, the wing-body intersection point was moved forward on the body. With the inersection point farther forward, the sweep angle of the forward wing was obviously increased which then helped to reduce wing supersonic wave drag.

The goal of deciding at what spanwise location to put the flaps was to try and achieve the maximum possible trim lift coefficient. This was done by making the moments induced on the front and rear wing roots as positively large as possible. This was achieved by placing the main flaps on the inboard front wing and the outboard rear wing (Wolkovitch, Overview, ref. 47).

As for the design of the twist and camber of the wings, reference 47 (Wolkovitch, Overview) conducted studies using a vortex-lattice program to determine, for low trimmed drag, the twist and camber characteristics of a joined wing. It is not essential to attain the optimum twist and camber exactly; linear or bilinear spanwise variations may be used instead. However, it is essential to "wash-out" the front wing so that its tip has less incidence than its root, and the rear should be "washed-in" with less incidence at its root than its tip. The rear wing should also incorporate less camber than the front wing.

Canards were employed for two reasons. One was that the vortices shed from the canards seemed to stabilize the boundary layer on the top of the forward wings and thus raise the C_{Lmax} (Wolkovitch, Overview, ref. 47). The second reason was that the increased lift on the front part of the plane helps with takeoff rotation.

The final geometric consideration was the placement of the engines. Because of the need for large inlet compression surfaces at high supersonic speed, using engine pods underneath the wings was ruled out. The only logical place to have the engines was underneath the body and use the forbody as a compression surface for the first part of the inlet.

Using all the basic geometry just discussed, a preliminary airplane design was derived. The sizing of the wing planform came from the sizing chart (Figure 3-3). The preliminary design point gave a lifting surface area of 4615 square feet. The preliminary body sizing was to account for the volume requirements for the number of passengers and the amount of fuel needed for the mission. A three-view drawing of the initial design for the Flying Diamond is found in Figure 4-3.

INITIAL THREE VIEW DRAWING

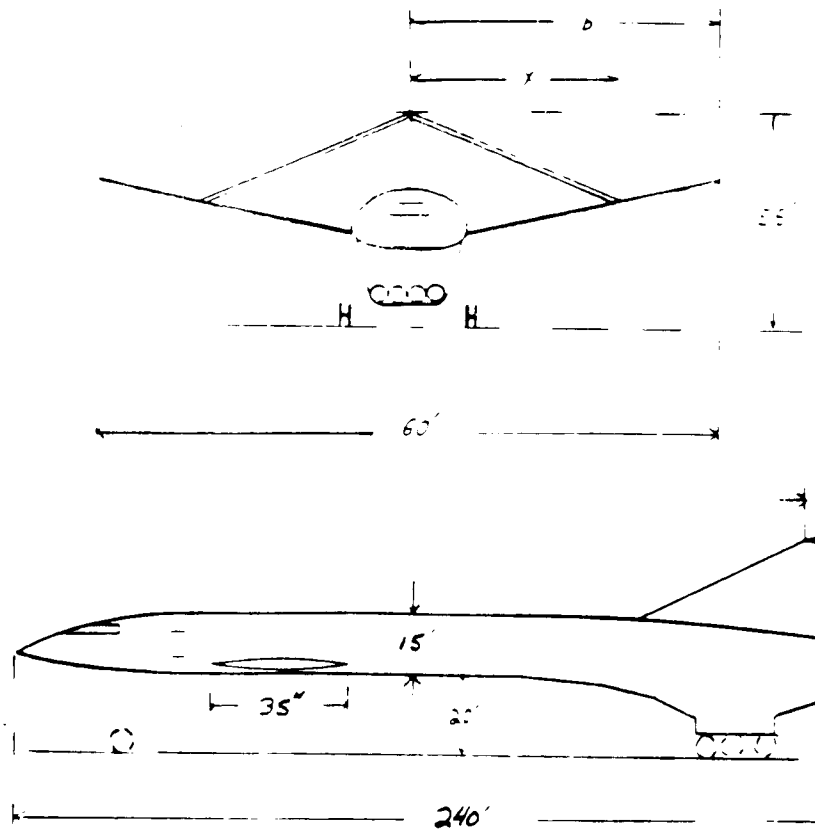

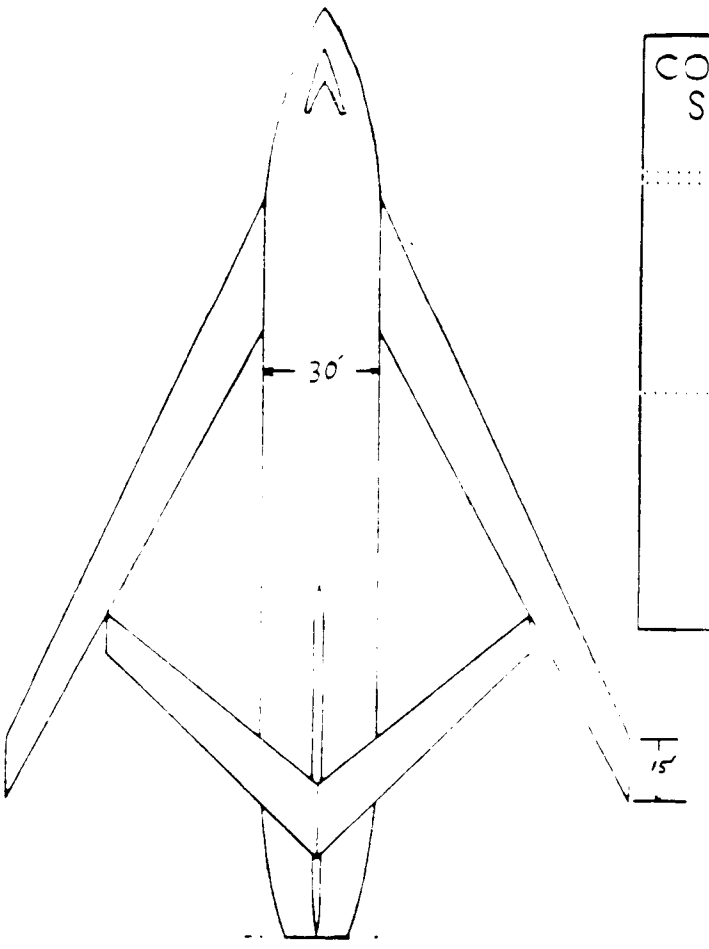

CONE ANGLE = 28°
S = 4900 sq ft
Ar = 5.4
Γ_F = 12.5°
Λ_F = 63.4°
λ_F = 0.43
Γ_R = -20.0°
Λ_R = -38.2°
λ_R = 0.59

FIGURE 4-3

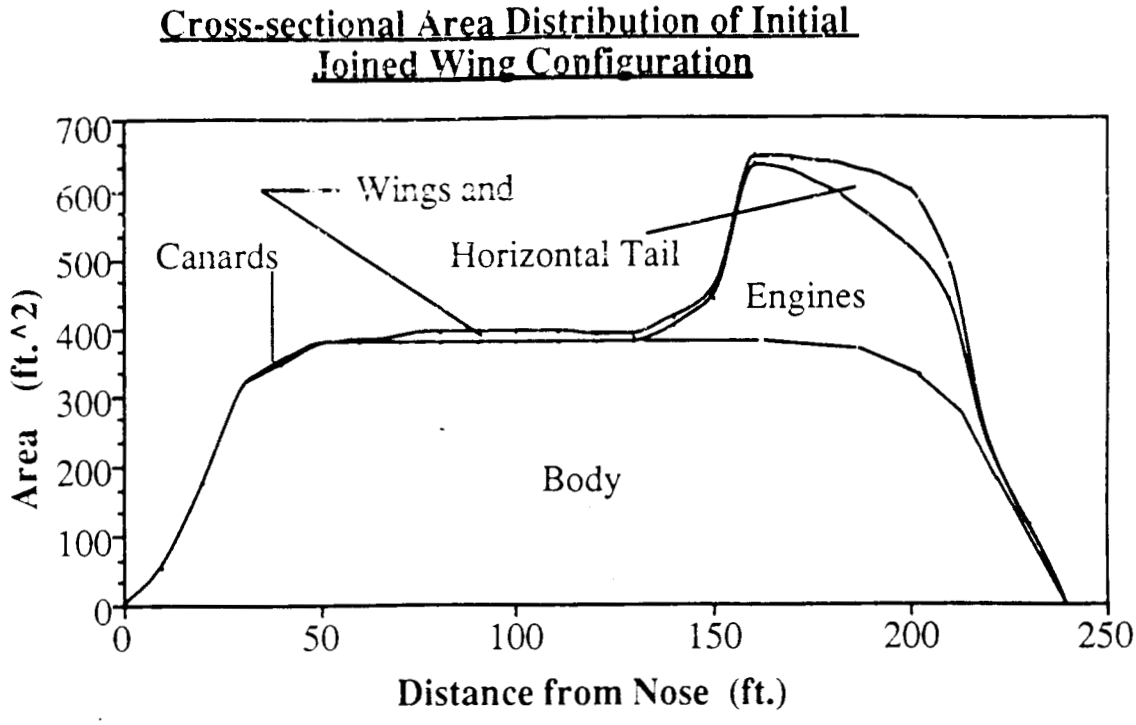

FIGURE 4-4

4.3 Area-Rule Criterion

In order to decide if this configuration was appropriate for supersonic flight, a cross-sectional area distribution was calculated. The area-rule states that for low transonic and supersonic wave drag, it is essential to have a continuous cross-sectional area distribution. It should not have any discontinuities or large and sudden "humps," (Nicolai, 13-1, ref. 11). From observing the area distribution of the preliminary design, Figure 4-4, it was apparent that th rplane did not meet the area-rule requirements. Therefore the body was reshaped in order to try and make the area distribution more parabolic in.

4.4 Body Contouring

Since the body was the main contributor to the total area it was the primary component of the plane to be manipulated. By an iterative process, the height and width distributions of the aircraft were changed in the longitudinal direction resulting in a "coke-bottling" of the body. An additional two feet was added to the height and an additional six feet was added to the width, increasing the area of the center section, while the sides of the top aft section of the body were shaved down, decreasing the area of the rear of the plane where the "bulge"in the area distribution had occurred. The result of this body contouring reshaped

the area distribution into a distribution that was acceptable to the area-rule criteria (Figure 4-5). Hence the final configuration for the Flying Diamond was as depicted in Figure 4-6.

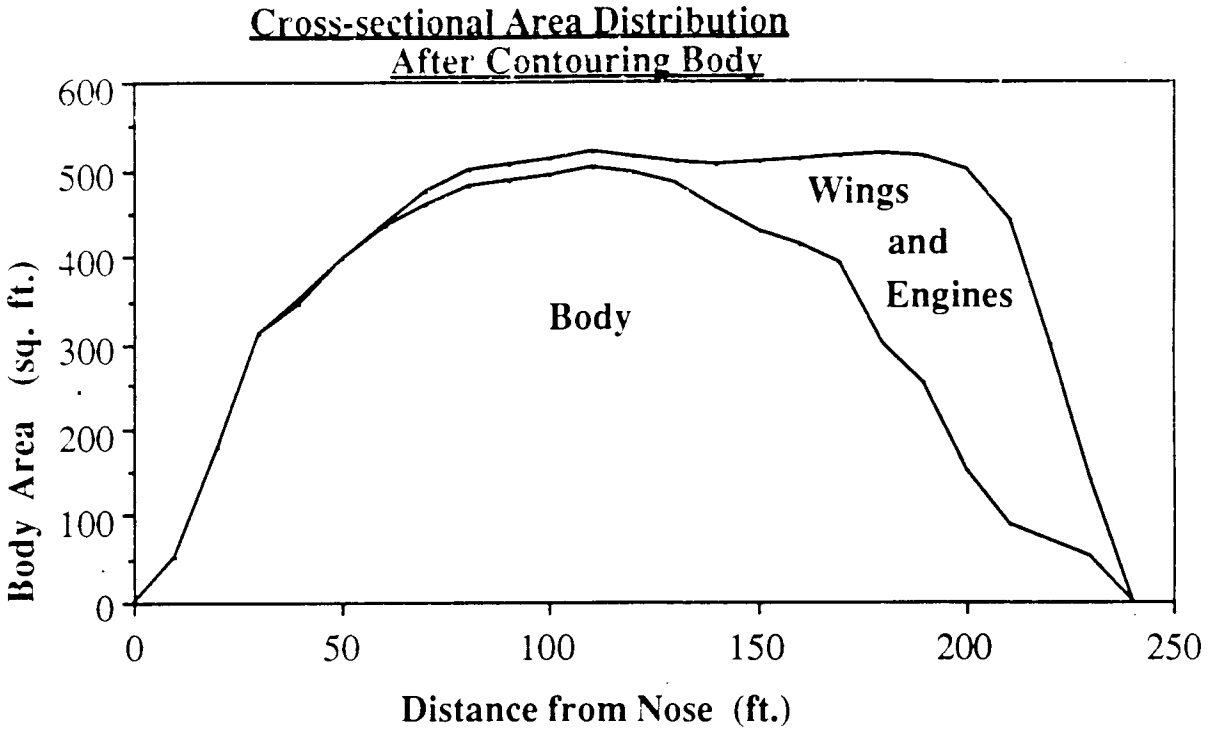

FIGURE 4-5

4.6 Interior Layout

The RFP requires, that in order for the aircraft to be economically feasible, it must hold at least 250 passengers. The Joined Wing HSCT holds 256 passengers. The dimensions of the seats, which are FAR 25 certified for resisting load factors, are described in Reference 9. The space required for the first class seats two across (double) are 41"long (L) x 49"wide (W). The space required to accommodate coach seats for two across (double) and three across (triple) is 38"L x 40" W and 38"L x 60"W respectively. The minimum width of the aisles is 20" and the minimum height of the ceiling is 43" at the seats and 76" in the aisle. From this, the overall dimensions of the passenger compartment were determined. The total length of the interior was 90.2 ft with a maximum width of 30 ft. The seating arrangement was designed to be space efficient while providing passenger comfort. The forward compartment holds 24 first class seats in an arrangement of three rows of two-across seating. This is standard among most major airlines. The rear compartment holds 232 coach seats which was divided into two sections.

FINAL THREE VIEW DRAWING

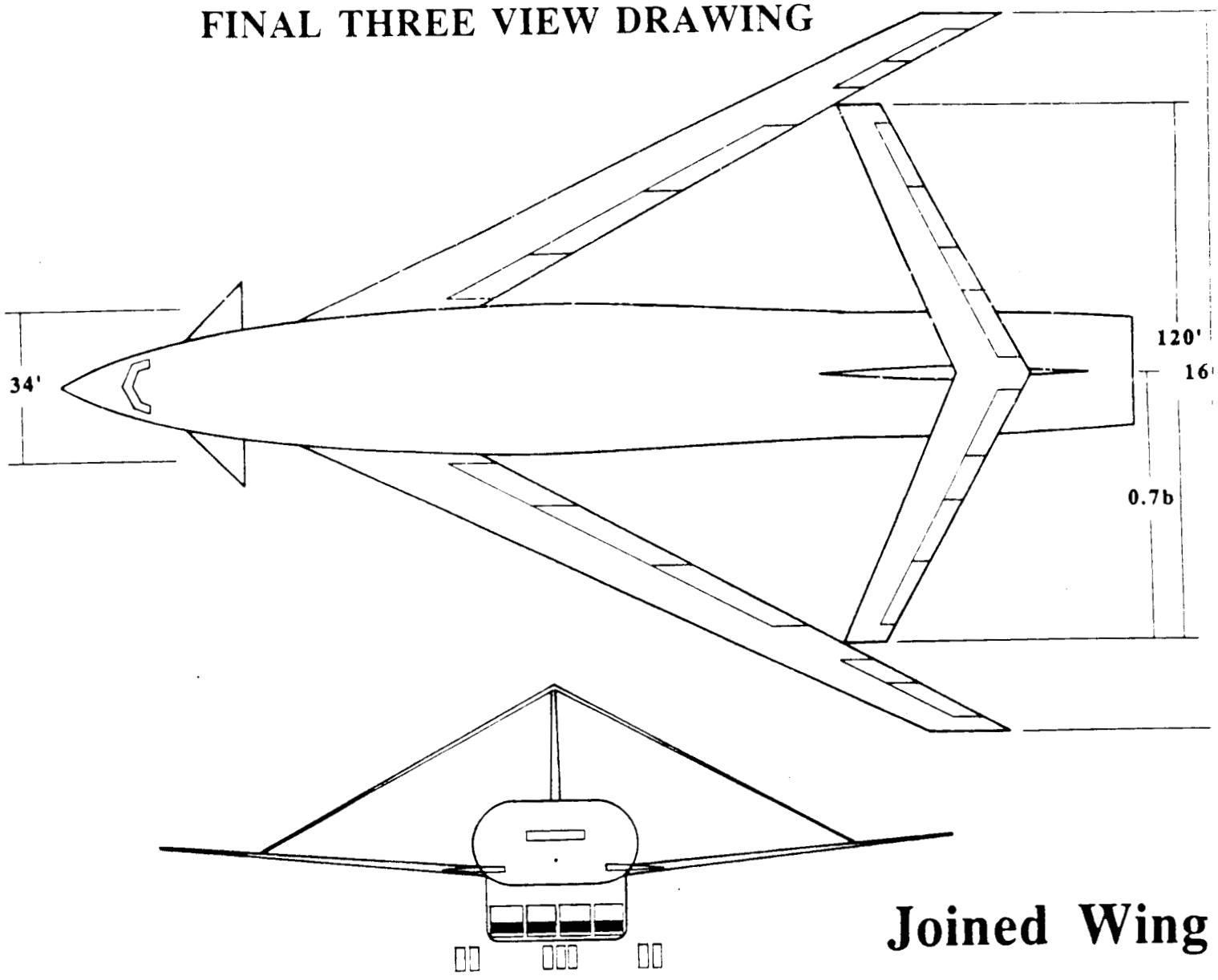

Joined Wing

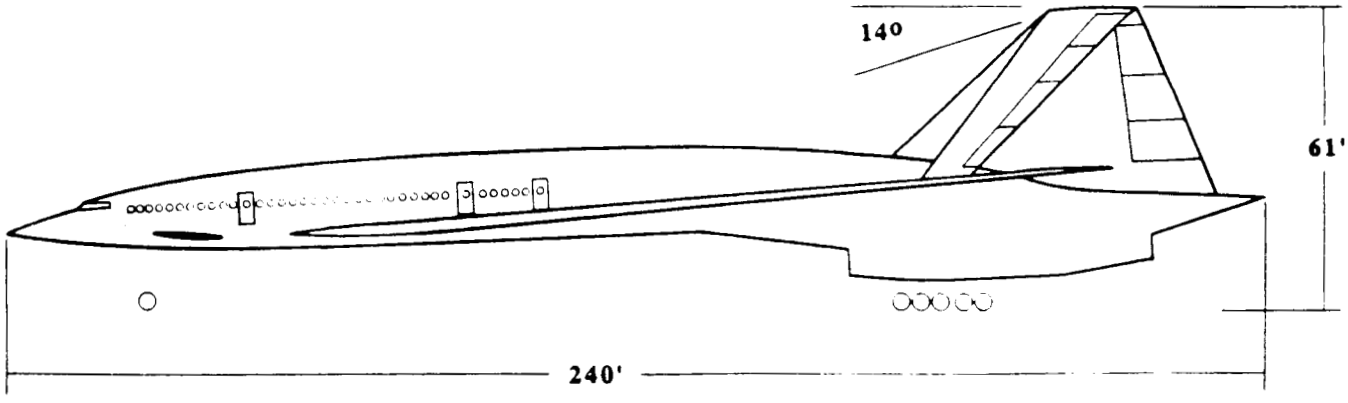

FIGURE 4-6

The first section has a three across - six across - three across (3-6-3) seating arrangement with 10 rows. The second section has a 3-4-4-3 seating arrangement with 8 rows. The addition of a third aisle in the second section was due to the FAR Part 25.817 restriction that stated on each side of an aisle, there be no more than three abreast seating. In addition to satisfying the FAR requirements, this additional aisle will add to passenger comfort. The first class and coach sections were separated by an area containing the main galley section, 6 lavatories, and two wardrobe storage compartments.

The number and size of these facilities was determined from other aircraft, similar in passenger capacity. This was all placed in one section to enhance turn-around time, which will be explained in section 13.2 To assist the passengers in flight, there will be 6 flight attendants, which reflects the industry standard ratio of attendants to passengers of 1:35. The ratio exceeds FAR 25 requirements. There exists an area above the passengers for storage of carry-on luggage.

4.7 Flight Deck Layout

The flight deck layout of the Flying Diamond incorporates the latest technologies into a simple design. It was designed for good visibility without the use of an articulated nose because of the complexity and the large weights associated with it. The layout of the flight deck is shown in Figure 4-7.

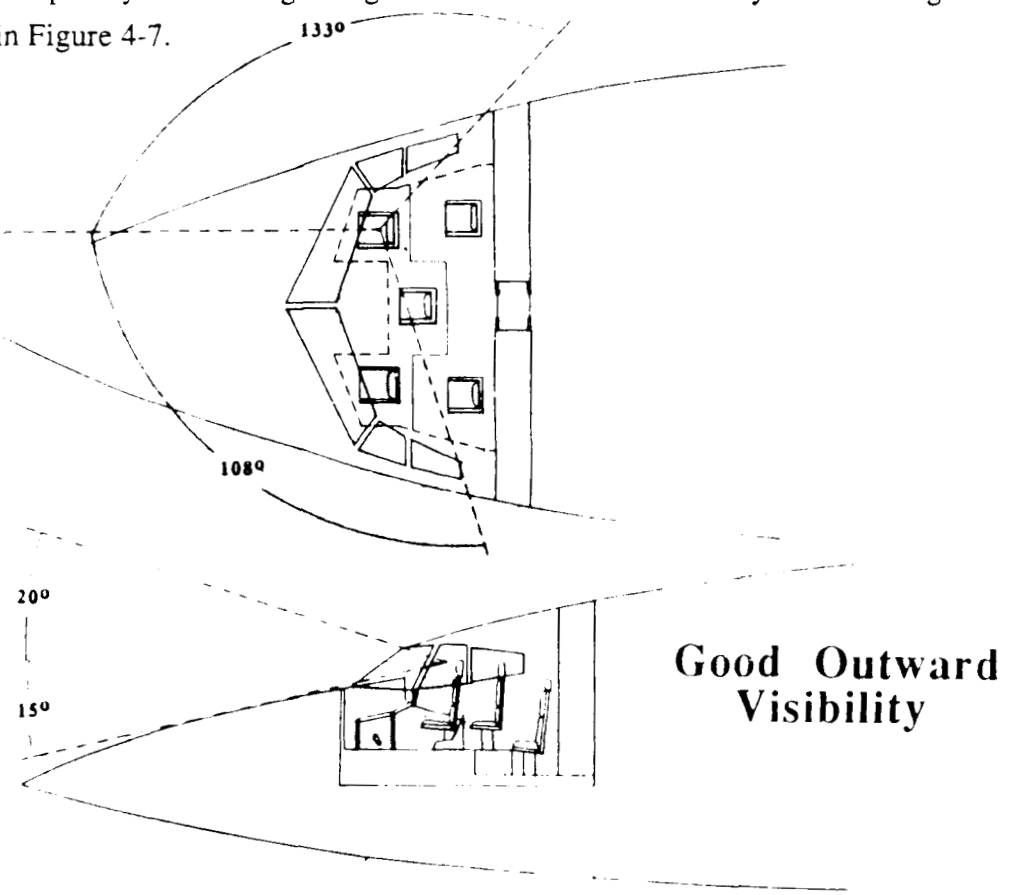

FIGURE 4-7

The dimensions for the flight deck were estimated by examining flight decks of similar aircraft. This resulted in a flight deck 12 ft long, with the width dependant on the fuselage shape. The outward visibility required by FAR Part 25 is met without the use of an articulated nose cone. The visibility over the nose is 15° and the upward visibility is 20°. The visibility to the side is 133° and 108° depending on the reference seat location. The HSCT flight deck was designed to have a visibility pattern similar to other aircraft which have been FAR 25 certified (the ideal visibility pattern is rarely met due to weight and drag penalties). The number of crew members was determined by examining similar aircraft crews, but also took into account the highly sophisticated nature of the aircraft. The HSCT will have one Captain, a First Officer, and a Flight Engineer. It will also be able to seat two observers, for training and other purposes.

The flight deck instrumentation layout was designed to reduce the pilot workload. The pilots can see and reach all important flight instruments and controls from their seated position. The instrument panel contains eight 8"x8" CRT color display monitors (Figure 4-8).

Instrument Panel Layout

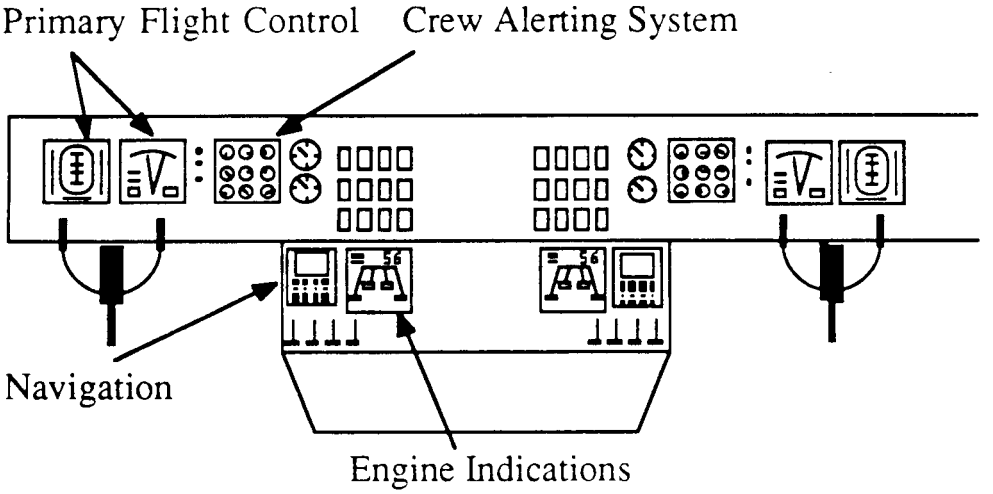

FIGURE 4-8

Each is able to provide many functions on one screen. These monitors will display the primary flight control instruments, navigation systems, engine indication systems, and crew alerting signals. These displays reduce the pilot workload by presenting an uncluttered panel which makes the instruments easier to see, allowing information at the touch of a button, and warning the pilot of danger without requiring the pilot to search for

the signal. In case the CRT displays should fail, the essential instruments for flight, such as the airspeed indicator, altimeter, compass, and fuel quantity indicator, are duplicated with conventional instruments. The flight controls controls are input through side-stick controllers, like the Airbus 320.

5.0 Aerodynamics

5.1 Drag Analysis:

For drag analysis the flight profile was divided into three phases; 1) Subsonic flight phase, 2) Transonic flight phase, and 3) Supersonic flight phase.

5.1.1 Subsonic Flight Phase

For subsonic flight it was assumed that the zero lift drag was mainly due to friction drag, and that the total drag was the sum of the component drags (Reference 11).

$$(C_{Do})_{total}=(C_{Do})_{F.W.}+(C_{Do})_{R.W.}+(C_{Do})_{F.}+(C_{Do})_{V.T.}$$

The equations given in Reference 11 were used to calculate the individual drag coefficients.

$$(C_{Do})_{F.W.}=C_f[1+L(t/c)+100(t/c)^4]R(S_{wet}/S_{ref})$$

$$(C_{Do})_{F.}=(C_{Df})_B+C_{Db}$$

$$(C_{Df})_B=C_f[1+60/(l_B/d)^3+0.0025(l_B/d)](S_s/S_{ref})$$

The above equations were also used to compute the drag coefficients of rear wing and vertical tail, with appropriate parameters. The skin friction was assumed to be turbulent at all times for conservatism. Also, the base drag was taken to be zero since the base area is almost negligible.

For induced drag the Oswald's efficiency factor was estimated from Reference 47 to be 0.9 at subsonic speeds. This value was used in the induced drag analysis and the following drag polars, Figure 5-1 was obtained for subsonic speeds.

$$(C_D)=(C_{Do})_{total} + K(C_L)^2$$

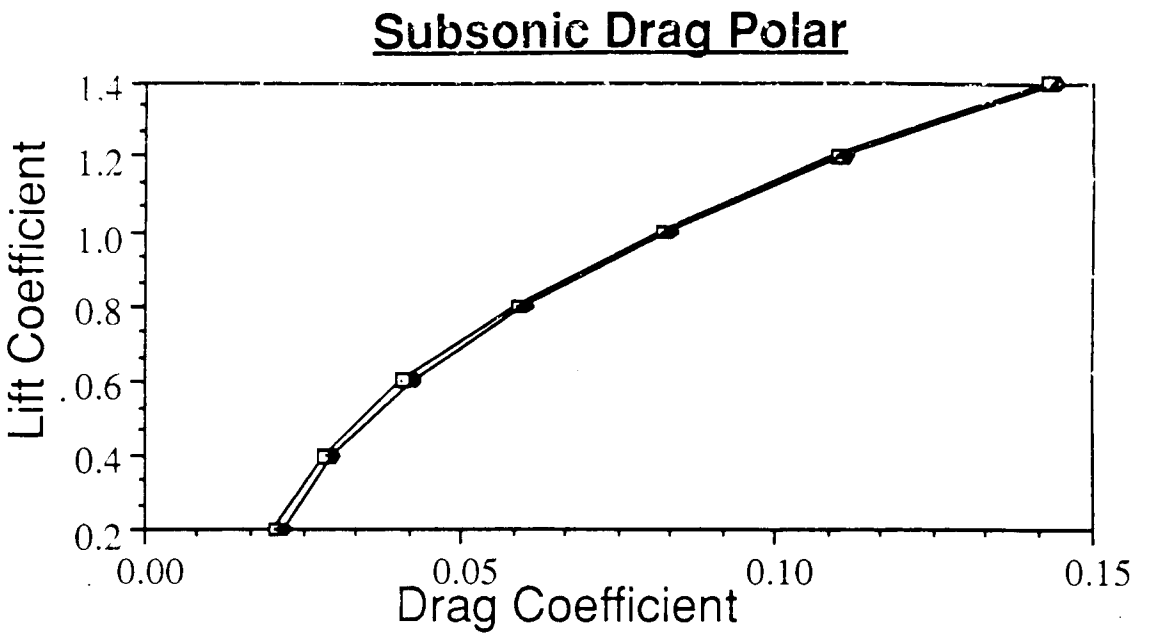

FIGURE 5-1

The subsonic methods were used for Mach numbers of up to 0.8.

5.1.2 Transonic Flight Phase:

In the transonic flight phase the major drag contributors were the friction drag, wave drag and induced drag. Again the methods of Reference 11 were used for the analysis. For lifting surfaces and vertical tail the following equation was used with appropriate parameters.

$$(C_{Do})=C_{Df}+C_{Dwave}=C_f[1+L(t/c)](S_{wet}/S_{ref})+C_{Dwave}$$

The wave drag was determined by constructing wave drag curves from experimental data that were corrected for sweep, aspect ratio and thickness using the von Karman similarity laws for transonic flow (Reference 11).

The transonic zero lift drag of the fuselage was divided into four sections: Friction drag, Pressure drag, Base drag and Wave drag.

$$(C_{Do})_B=(C_D)_f+(C_D)_p+(C_D)_b+(C_D)_{wave}$$

$$(C_D)_p=(C_f)_{M=.6}[60/(l_B/d)+0.0025(l_B/d)](S_s/S_{ref})$$

$$(C_D)_f=C_f(S_s/S_{ref})$$

The base drag was taken to be zero since the base area is negligible, and the flow was assumed to be turbulent. For body wave drag experimental data was used (ref. 11).

5.1.3 Supersonic Flight Phase:

During supersonic flight the main lifting surface drag contributions are due to friction and wave drag. The skin friction was calculated assuming turbulent flow and flat plate analogy (Reference 11), and the values were corrected for compressibility effects .

For wave drag two different equations were used and are identified below.
$(C_{Do})=(C_D)_f+(C_D)_{wave}$

$$(C_D)_f=C_f(S_{wet}/S_{ref})$$

$$(C_D)_{wave}=(B/b)(t/c)^2(S_e/S_{ref}) \text{ ----- Supersonic L.E.}$$

$$(C_D)_{wave}=B[\cot(\text{L.E. sweep})](t/c)^2(S_e/S_{ref}) \text{ ----- subsonic L.E.}$$

The induced drag coefficient factors for lifting surfaces were calculated using the methods of reference 45.

For fuselage the zero lift drag was divided into five sections: 1) Compressible turbulent skin friction drag, 2) Nose wave drag, 3) Fuselage afterbody wave drag, 4) Interference drag coefficient, 5) Body base drag (Reference 11).

$$(C_{Do})_B=C_f(S_s/S_{ref})+(C_D)_{N2}+(C_D)_A+(C_D)_{A(NC)}+C_{Db}$$

The skin friction drag was again calculated using the flat plate analogy and the base drag as before was taken to be zero. The nose wave drag, fuselage afterbody wave drag and interference drag coefficients were obtained from experimental data presented in Reference 11.

Zero lift drag coefficients are presented in Figure 5-2 and Figure 5-3 for both subsonic and supersonic flight regimes, and because of the high sweep the maximum zero lift drag occurs at Mach number around 1.4 to 1.5 (Reference 11).

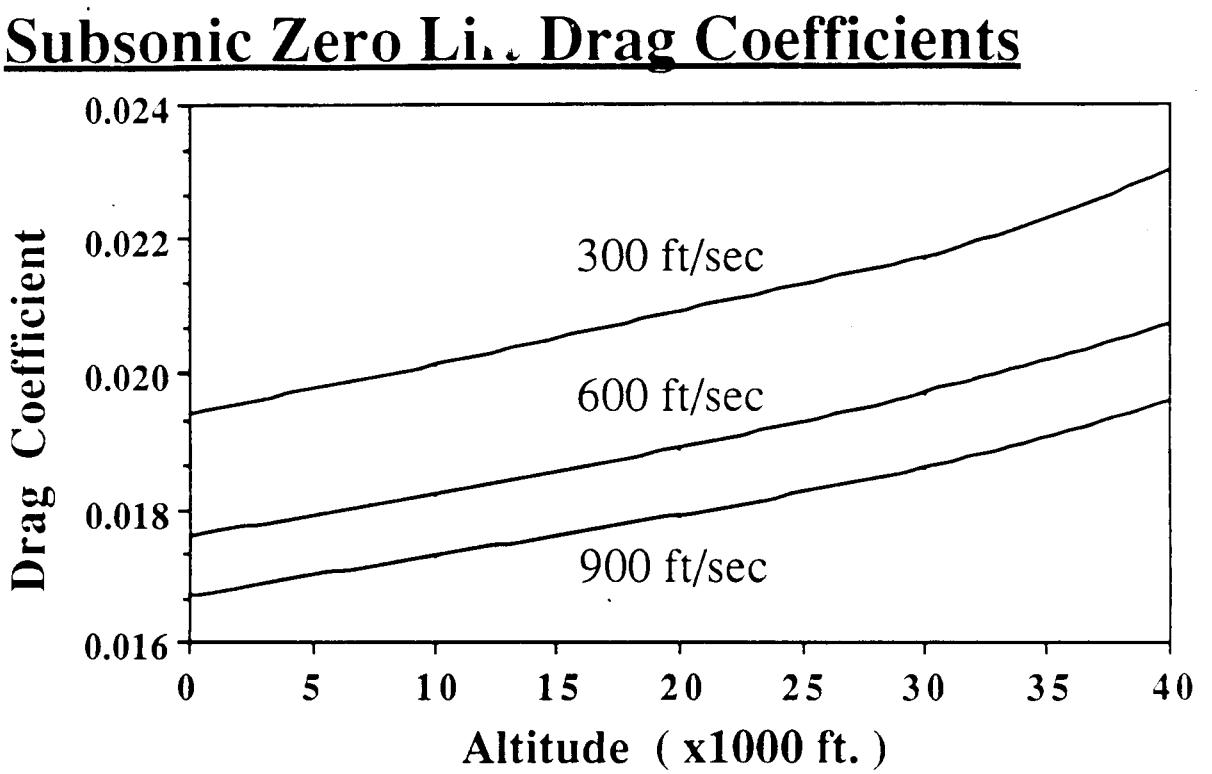

FIGURE 5-2

5.2 Lift Coefficient

The Joined wing configuration in general provides higher lift coefficients than the conventional configurations due to the fact that the rear lifting surface acts as a secondary wing structure rather than a horizontal tail. Thus, high lift devices can be installed on the rear wing resulting into high takeoff lift coefficients and shorter distances.

This advantage was used in the Flying Diamond design. Sixty percent span plain flaps , both on front and rear wings, were incorporated into the design. This resulted into a maximum combined lift coefficient of 2.4 which was sufficient for takeoff and landing. (Figures. 5-4 Cl curves with flaps deflected) (Ref. 11 Nicolai).

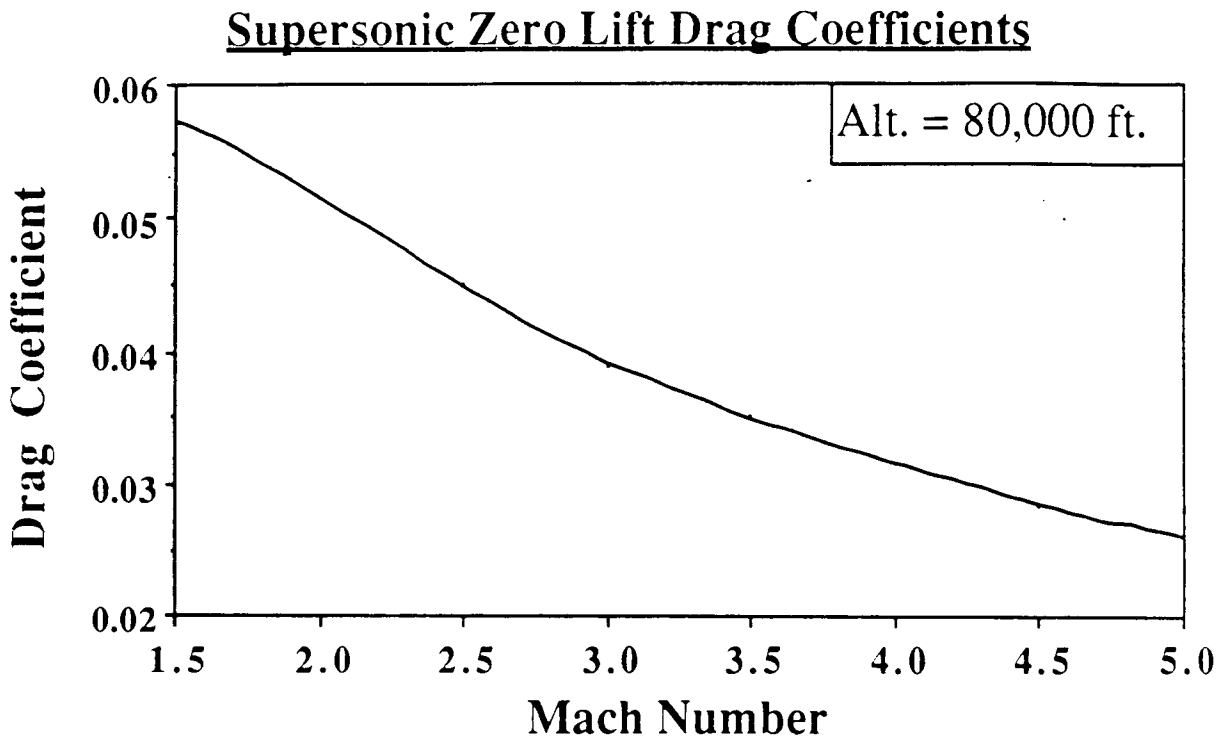

FIGURE 5-3

To determine if enough lift will be provided during climb and cruise phases, the lift coefficients were calculated using two different methods applicable to different mission phases.

For intermediate speed ranges (subsonic) the lift coefficients were calculated using the Vortex Lattice method. However, for supersonic climb and cruise phases the supersonic linear theory was used, corrected for three dimensional effects (ref. 11 Nicolai).

Since the Flying Diamond has an elliptical fuselage cross sectional area, at supersonic speeds it will generate almost 50 % of the lift. This was calculated using DATCOM's methods.

6.0 Performance

The performance analysis for the Joined Wing aircraft was computed in segments. Each segment of the mission profile from take-off to landing will be considered in the following sections.

6.1 Take-Off Distance Analysis

The take-off performance analysis was conducted using the methods presented in Nicolai (Reference 11, chapter 10). The regulations governing the take-off procedures for conventional commercial aircraft were found in FAR section 25 (Reference 8).

The total take-off distance is considered to be the distance required for an aircraft to accelerate from rest to take-off speed and climb over a 50 foot obstacle. The take-off portion is subdivided into four separate portions: ground roll, rotation distance, transition distance, and distance to climb to 50 feet. Each one of these portions will now be examined:

6.1.1 Ground Roll:

FAR 25 states that a civilian commercial transport must have a take-off velocity of greater than 110% its stall speed. The Joined Wing will be designed to meet and exceed this requirement and will take-off at a velocity that is 120% of its stall speed. The stall speed of the aircraft was determined by considering the conditions at which the lift generated is equal to the weight of the aircraft. At the aircraft's maximum lift coefficient the stall speed was determined using the definition of the lift coefficient and replacing the lift term with the weight of the aircraft (Ni ii, Reference 11, eqn 10-2):

$$V_{Stall} = 1.2\sqrt{\frac{2\,W_{TO}}{\rho\,S\,C_{Lmax}}}$$

The weight of the aircraft at take-off is equal to W_{GTO} times the fractional loss of fuel that is burned during the start-up, warm-up and the taxi portions of the mission profile (see Section 3•2), or:

$$W_{TO} = (900{,}432)(0.99)(0.995) = 886{,}970.5 \text{ Pounds}$$

C_{Lmax} was determined from Section 5.2 to be 2.4 with the flaps on both rear and fore wings extended 30° and without the canards deployed. Assuming standard sea level conditions the stall velocity is calculated to be V_{Stall} = 188.5 knots. (Note that while the stall speed calculated here is considerably higher than V_{Stall} calculated in section 3•3, the aircraft is over 300,000 pounds heavier). The take-off velocity may then be calculated to be W_{TO} =1.2 (188.5) = 226.2 knots.

The ground roll distance of the aircraft is a function of the forces acting on the aircraft while it's accelerating from rest to it's take-off velocity. The acceleration of the aircraft at any point during ground roll may be found using the summation of the forces in the X-direction (along the thrust vector). This produces the following equation:

$$a_X = \frac{g}{W}[T - D - F_f] = \frac{g}{W}[T - D - \rho(W_{TO} - L)]$$

The average ground resistance friction coefficient for rubber tires on an concrete or asphalt runway is equal to μ = 0.025. T, D, and L are all functions of V, and therefore the acceleration of the airplane is not constant.

The average acceleration was assumed to be equal to 70% of the take-off velocity (Reference 11), and the ground roll was found to be equal to 6500 feet. This distance was also calculated using the abe equation to solve for the acceleration using the sum from rest to the take-off velocity using increments of 10 fps. This method calculated the ground roll to be 6832 feet. The average of the two methods was the final value used in the analysis. The Flying Diamond is estimated to have a ground roll of 6666 feet.

The distance covered while the aircraft is still on the airfield and has rotated to an angle of attack is assumed to be the distance covered during 3.0 seconds (Reference 11). This is 652 feet for the joined wing aircraft. While the aircraft is in the transition phase (the portion of climb out at a constant radius) it climbs above the FAR checkpoint of 50 feet. This distance was calculated to be 250 feet. The following figures show the effect of these distances with various ambient atmospheric conditions. Figure 6-1 illustrates the effect of both temperature and elevation on the aircraft take-off distances. Note that under all circumstances examined the take-off distance is well under the RFP requirement of 11,500 foot take-off distance. Figure 6-2 is the effect of headwind and tailwind on the take-off distance. The Flying Diamond meets the RFP criterion with both headwinds and tailwinds of magnitudes up to 50 feet per second.

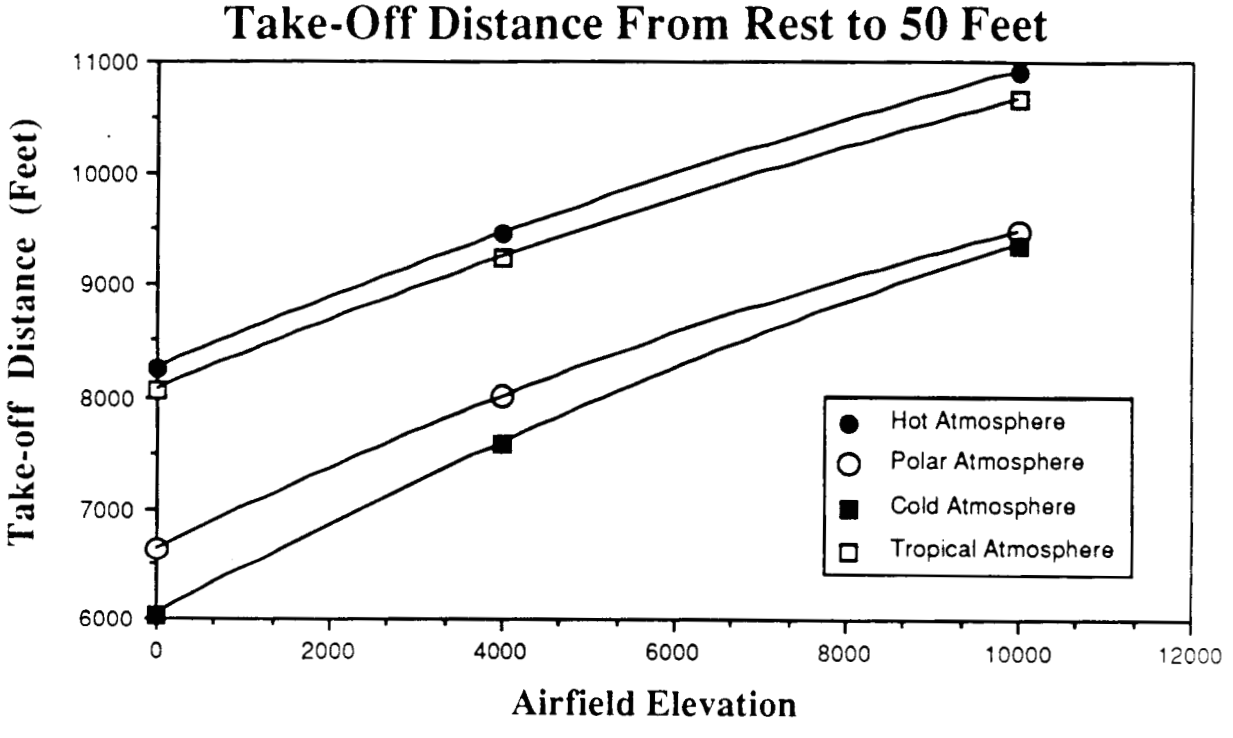

FIGURE 6-1

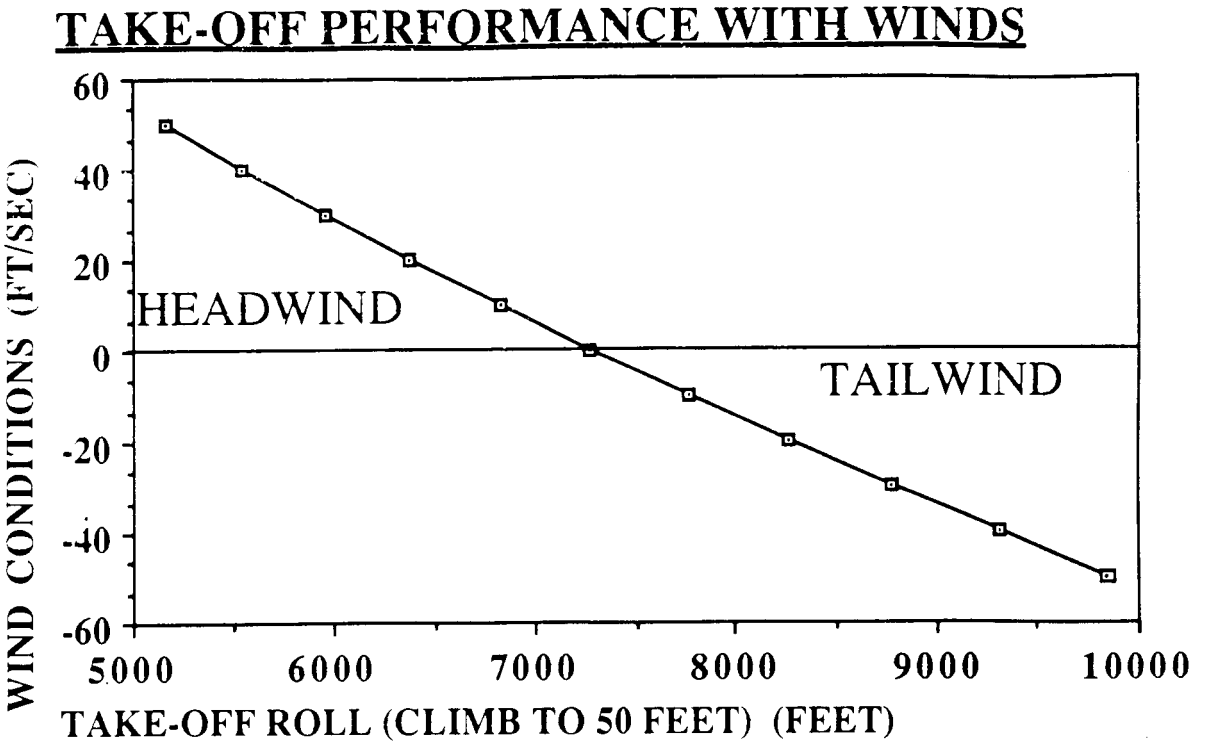

FIGURE 6-2

6.2 Cruise Performance

To properly analyze the cruise performance of the aircraft, it was first assumed that at cruise the plane was in unaccelerated level flight. Doing this, then the thrust required for the airplane would by equal to the plane's drag and the airplane's lift would be equal to the weight:

$$W = L = C_L\, q\, S$$

$$T_r = D = (C_{D_o} + K\, C_L{}^{\wedge}2)\, q\, S$$

When weight equation was rearranged and substituted into thrust required equation, then the final equation for the thrust required, using $q = \frac{g}{2} P\, M^{\wedge}2$, came out to be:

$$T_r = \frac{g}{2} P\, M^{\wedge}2\, S\, C_{D_o} + \frac{2KW^{\wedge}2}{gPM^{\wedge}2S}$$

The values for the zero lift drag coefficients and the supersonic drag-due-to-lift (K) factors that were used in determining the cruise thrust required were calculated previously. Thus, the parameters that needed to be optimized were pressure (which is a function of altitude

for parametric studies), Mach number, and weight. Hence, the thrust required for cruise was calculated for a range of altitudes and crossed with a range of Mach numbers. The weight that was chosen was the weight at the beginning of cruise (W = 720,000 lbs.) because that was the worst cruise case or where the thrust required was the highest during the cruise phase. The results of this are contained in Figure 6-3.

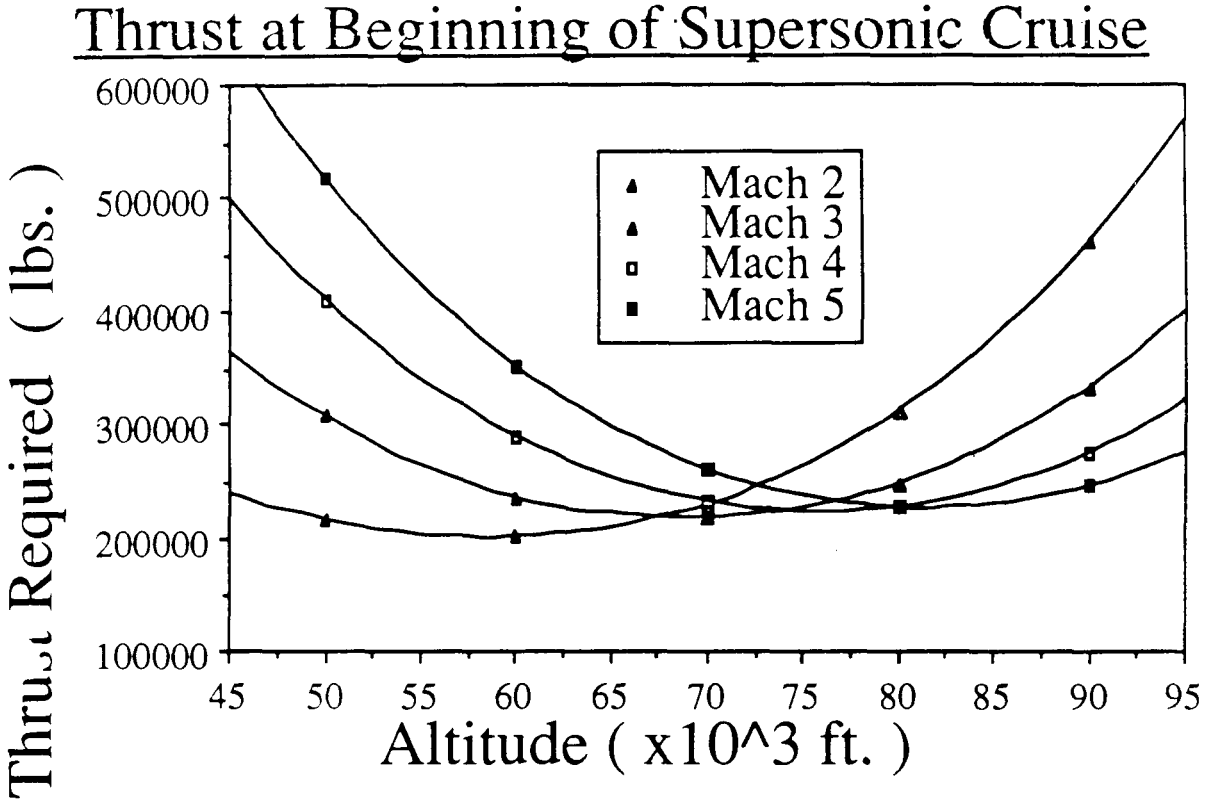

FIGURE 6-3

The trends of the later portion of Figure 6-3 might seem contrary to intuition and thus needs some explanation. The Mach curves do have a definite minimum. This is reasonable because of the second order nature of the final thrust required equation. However, after the minimums, the graph seems to imply that to increase in speed at a high altitude, the throttle must be pulled back. This is not the case. In order to stay at a constant speed, the trottle must be increased as altitude is gained.

After Figure 6-3 was thoroughly studied, the final thrust required equation was employed

again and more graphs were generated using weights corresponding to the weights during the cruise phase. It was found that in order to cruise at the optimum altitude, or where the thrust required was at the minimum, the plane must be in a shallow climb throughout the cruise (See Figure 6-4).

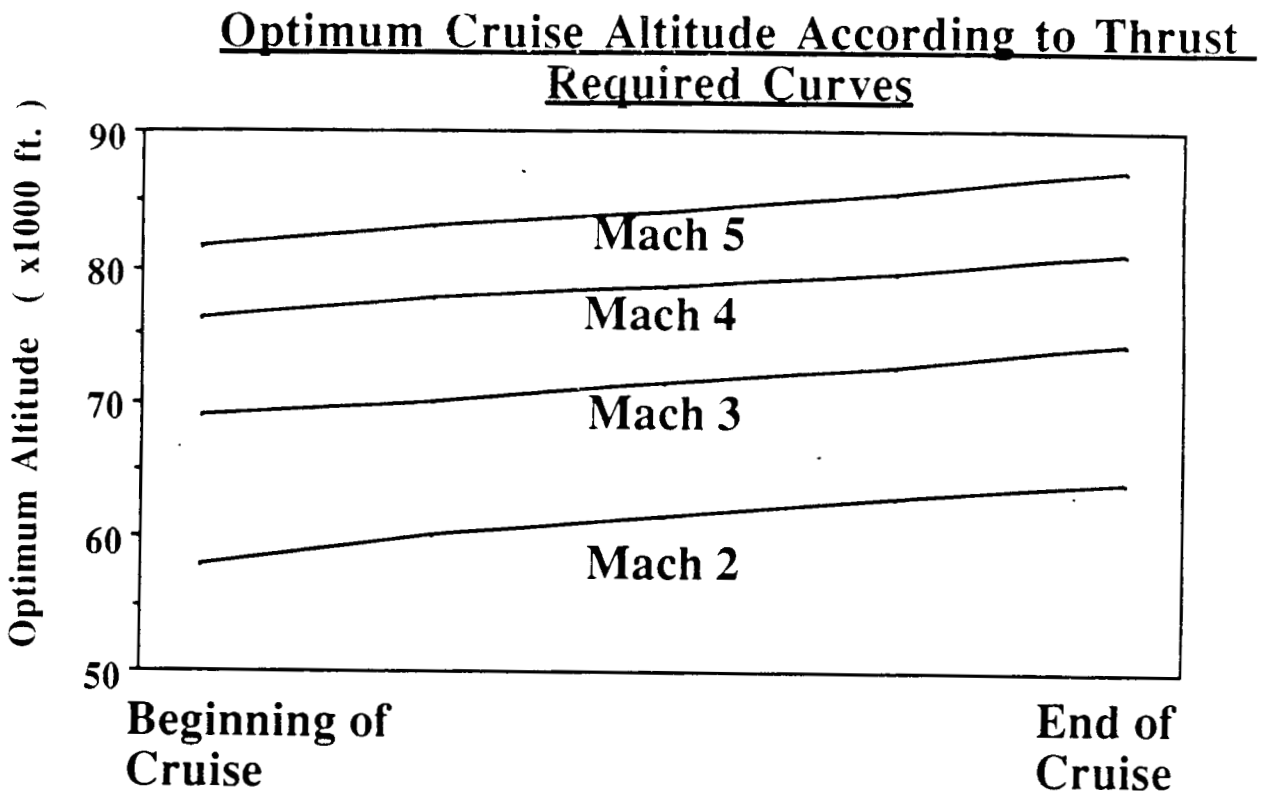

FIGURE 6-4

Using this type of plot, the cruise altitudes were set during the cruise portion assuming that the plane would always fly at the altitude of minimum thrust required.

In order to make certain that the plane will be able to fly at these specified speeds and altitudes, the thrust provided by the engines was studied. The thrust output from the engines was calculated, as will be discussed later, for different Mach numbers at different altitudes. Subtracting the thrust required from the net thrust available from the engines, the excess thrust was obtained for all possible cruise conditions. These curves in Figure 6-5 determined at what altitudes and at what Mach numbers the aircraft was able to operate. These possible flight envelopes are summarized as follows:

Speed of aircraft Mach	Range of operating altitudes min.	max.
2	⇒	78,500 ft.
3	53,000 ft.	80,500 ft.
4	58,500 ft.	92,000 ft.
5	68,000 ft.	⇒

By comparing these cruise envelopes to Figure 6-4, it was apparent that the engines provided enough thrust to enable the Flying Diamond to cruise at any Mach number during the entire cruise phase while staying at the optimum altitude.

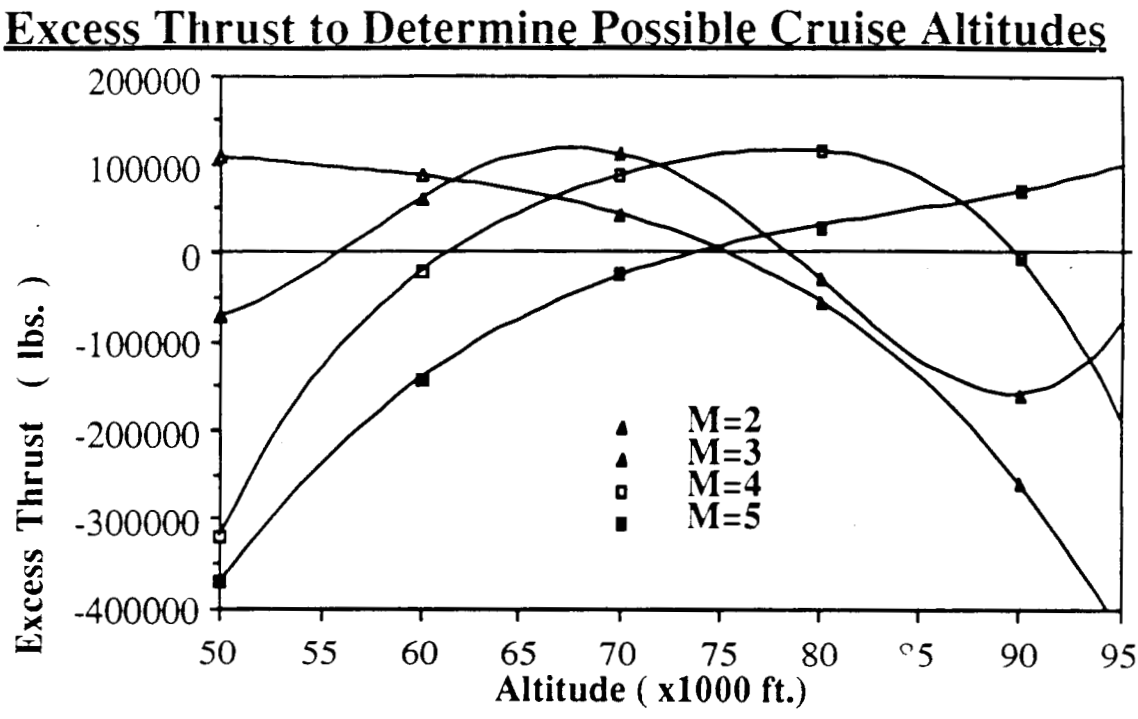

FIGURE 6-5

7.0 Stability and Control

A brief analysis of subsonic stability and control was performed for the Flying Diamond. Below are the fruits of that task.

7.1 Methods / Assumptions

The methods of Jan Roskam cited in References 20 and 21 were used to estimate the stability characteristics of the Joined wing. Some assumptions were made to use his work. One assumption was that the Joined wing will employ thin swept wings. By examination of the elevation views of the aircraft one can see that the wings are swept and furthermore, supersonic flight imposes a thin wing constraint on choice of thickness. The front and rear wings and the vertical tail were assumed to be composed of 4% chord thick double wedge airfoil sections having 90% of the theoretical lift curve slope of 2p. The rear wing and vertical tail were assumed to be operating in 90% of the dynamic pressure field experienced by the front wing. Ninety percent was chosen as a conservative estimate in contrast to ninety-five percent suggested by Roskam. The change of average drag at zero lift with Mach number was assumed to be zero as well as the change of drag coefficient with Mach number. Roskam and the authors of this report defend these assumptions as being acceptable for preliminary design purposes. A functional dependence for the change of airplane moment with angle of attack on the distance from the wing root quarterchord, body length and maximum body width, given by Reference 43, was assumed. The location of vertical tail aerodynamic center was also assumed to be at its average quarterchord for the subsonic speed range. The most important assumption made in this analysis was that the rear wing was treated as a horizontal tail and will be referred to as such for the remainder of the chapter. Julian Wolkovitch Reference 44, the pioneer of the Joined wing, said this would be an acceptable approximation if a more laborious, time-consuming effort could not be made.

7.2 Static Stability Results

Tables 7-1 and 7-2 show the longitudinal and lateral subsonic, power-off non-dimensional stability derivatives. The angle of attack and speed derivatives except C_{D_u} were all within generally accepted ranges and were additive to static stability (SS). The pitch rate derivatives C_{L_q} and C_{m_q} (the pitch damping derivative) were in range and of proper sign. C_D-alpha dot was assumed to be zero, C_L-alpha dot was computed with a triangular wing assumption and C_m-alpha dot, while being of proper sign and of usual magnitude neglected contributions from the fuselage or front wing. Variation of sideforce with

sideslip (C_{y_B}) added stability but the calculated dihedral effect (C_{l_B}) was destabilizing having a value of .015. This seems to make sense as the large anhedralled planform of the rear wing offset and dominated the dihedral of the front wing in providing rolling moment in sideslip. Static directional stability (C_{n_B}) was calculated to be favorable even as the front wing was neglected. C_{y_p}, C_{l_p} and C_{n_p} were in their generally accepted ranges and negative but C_{l_p}, the roll damping derivative, was justifiably computed without body contribution since the Flying Diamond has an elliptically shaped, non-cylinder-like body. C_{n_p} lacked rear wing contribution. From the yaw-rate derivatives the yaw-damper C_{n_r} was destabilizing which means a larger vertical tail may be necessary but the calculation wrongly assumed a negligible contribution from the rear wing. Change of airplane drag with flap deflection, C_D delta-E and C_y delta-A, were assumed zero and C_L delta-F assumed sealed-gap type flaps.

TABLE 7-1

Longitudinal Stability Derivatives

C-D-Alpha	0.1053	C-D-Delta-F	0
C-L-Alpha	3.5308	C-L-Delta-F	0.6276
C-M-Alpha	-0.0680	C-M-Delta-F	--------
C-L-u	0	C-L-i-H	--------
C-D-u	0.1989	C-D-i-H	1.7422
C-M-u	-0.0519	C-M-i-H	-2.7377
C-D-Alpha-dot	0	C-D-Delta-E	0
C-L-Alpha-dot	-7.0794	C-L-Delta-E	0.2210
C-D-Alpha-dot	-2.2159	C-D-Delta-E	0
C-L-q	0		
C-L-q	4.7289		
C-M-q	-15.0531		

TABLE 7-2
Lateral-Directional Stability Derivatives

C-y-Beta	-0.8659	C-y-Delta-A	0
C-l-Beta	0.0148	C-l-Delta-A	--------
C-n-Beta	0.2337	C-n-Delta-A	0
C-y-p	-0.1586	C-y-Delta-R	-0.1306
C-l-p	-0.3275	C-l-Delta-R	-0.0174
C-n-p	-0.0041	C-n-Delta-R	-0.0581
C-y-r	0.5303		
C-l-r	0.6627		
C-n-r	0.2005		

At low subsonic speeds (M=.25) the Flying Diamond was longitudinally unstable (C_m-alpha >0) but an analysis of the canard aerodynamics proved it could reverse the sign of C_m alpha from approximately +.34 to -.53 if placed at a flow incidence of -5 degrees.

7.3 Expected Trends for Subsonic Joined wing

Wolkovitch (Reference 47) wind-tunnel tested several joined wing configurations. He found some configurations (high aspect-ratio, low sweep angle) exhibited a "mildly non-linear pitch-down characteristic" at moderate (4 degree) and high (10 degree) angles of attack below stall (16 degrees). With another model, his JW-1, he found a linear variation in moment. (Reference 38) He also stated by adding a 60 degree sweep canard to a joined wing subsonic airliner planform caused the pitch-down tendency to reverse to a pitch-up tendency. Rear wing elevators, like those on the Flying Diamond, were adequate to control the pitch-up. Wolkovitch found with a transonic joined wing model C_{nB} was linear with changes in angle of attack. The rear wing was thought to provide measures of directional stability equal that of the vertical tail, however, the vertical tail effectively reduces the sideslip angle seen by the rear wing by 50%. Also, "The greatest roll control power is obtained by mounting the front wing ailerons slightly inboard so that their upwash/downwash increases the rolling moment on the outboard sections of the rear wing." (Reference 47) This fact is crucial to the Flying Diamond since adequate roll

control will be necessary. Wolkovitch observed low rudder effectiveness in the high aspect ratio, low sweep model mentioned above yet flight tests on several of his radio-controlled models had adequate rudder effectiveness.

7.4 Expected Trends for Supersonic Joined wing

Spearman (Reference 49) noted some supersonic stability characteristics which are probable for the Joined wing. C_L- alpha and C_{D_0} should decrease with supersonic Mach number while static margin should increase due to an increase in upwash at speeds above Mach 2 and an increasing fuselage contribution. Static margin may decrease and be non-linear with a low wing and high tail. The non-linear function in static margin may lead to multiple trim points. Directional stability decreases (C_{n_B}) with Mach number which justifies a perhaps oversized vertical tail for the subsonic regime.

7.5 Stability Augmentation System

The Flying Diamond fully expects to employ a Stability Augmentation System (SAS). The SAS will, as its name implies, correct the instabilities of the airplane. Airplanes of today and of the future, like the Grumman X-29, are prioritizing performance and mission capability as of being higher significance than static or dynamic stability or control because of the available technology to assist the handling characteristics. The Flying Diamond will require an SAS to correct its subsonic instabilities and most likely its supersonic characteristics as well.

8.0 Propulsion

The propulsion system design for the Flying Diamond was a major undertaking due to the wide range of altitudes and flight speeds the aircraft would encounter. The original concept for the plane was for a Mach 3-6 transport cruising at 100,000 feet with a range of 6500 nautical miles. These parameters were modified in order to provide a more feasible propulsion unit. The major challenge was to provide a propulsion system that could go from zero to a Mach number between 3 and 6, and to do it efficiently in order to accommodate the range with a reasonably sized aircraft. The following describes the process and development of the propulsion system.

8.1 Engine Considerations

One of the first considerations to be undertaken was that of choosing the engine type. The main problem encountered was accommodating the cruise Mach number range. Figure 8-1 shows some of the propulsion alternatives as functions of Mach number and specific impulse. As can be seen, no one basic engine type goes from zero to Mach 6 efficiently. Rocket propulsion would cover the speed range but its specific impulse is low and rocket propulsion requires that both fuel and oxidizer be carried. This would make the weight of the propulsion system, not to mention the aircraft, too high to be feasible.

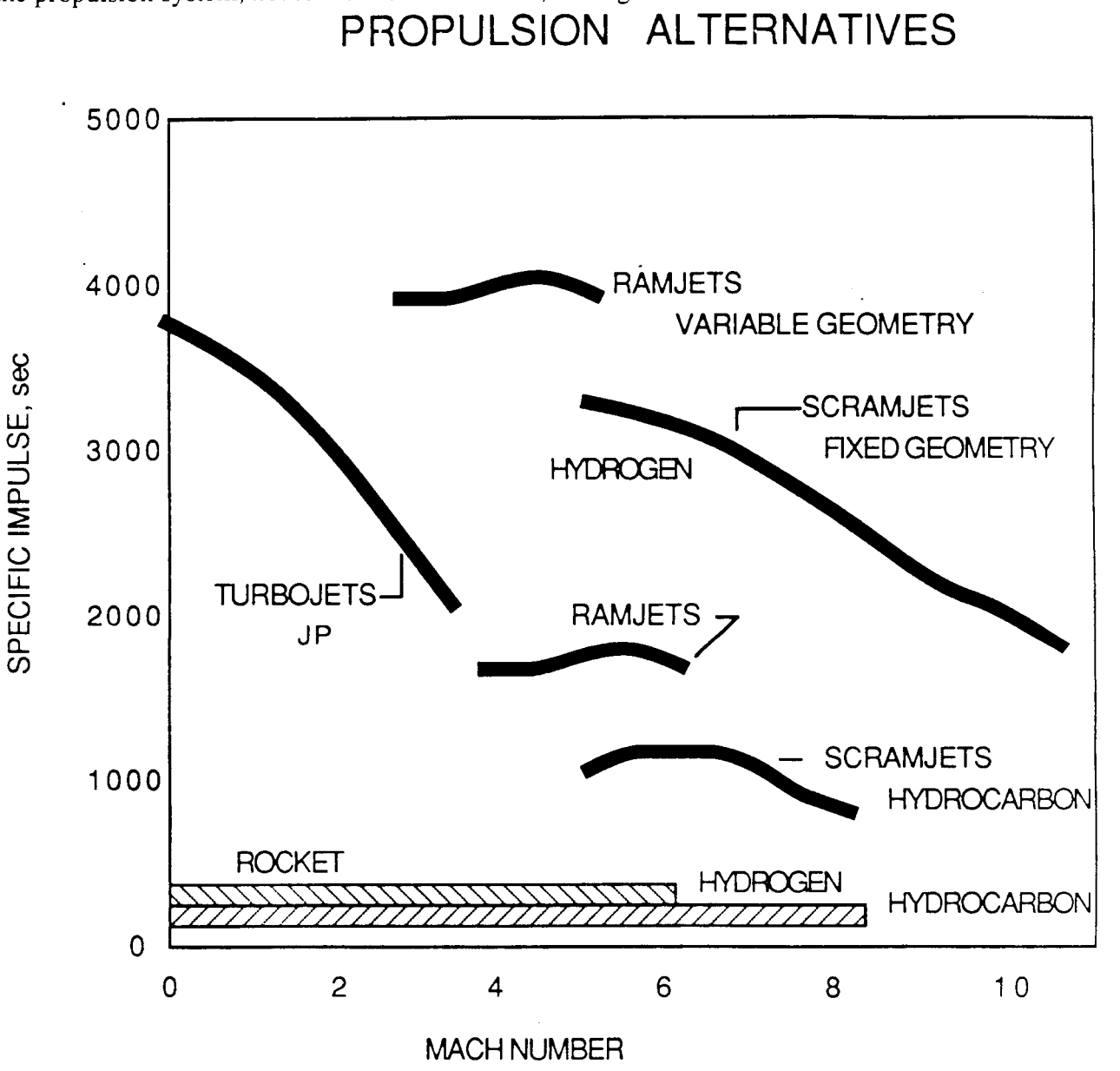

FIGURE 8-1

The scramjet was another propulsion alternative that was ruled out. The scramjet is tailored for flying at speed ranges in excess of Mach 6. Because this is out of the design cruise Mach number range for the Flying Diamond, the scramjet would not be used efficiently. For Mach numbers less than 6, other propulsion alternatives have better performance.

From examination of Figure 8-1, it can be seen that turbojets perform well up to approximately Mach 3, but their efficiency falls off at higher Mach numbers. Also, it can be seen that ramjets perform well in the Mach 3 to 6 speed range but fall off at speeds slower than that. From this, the preliminary conclusion was that the way to obtain the best performance from the propulsion system was to have it operate like a turbojet in the Mach 0 to Mach 3 speed range and like a ramjet in the Mach 3 to Mach 6 speed range. Therefore, some type of hybrid turbojet/ramjet engine seemed to be in order.

8.2 Turboramjet Engines

Because of the conclusion that a hybrid turbojet/ramjet type of engine would be the best candidate for the Flying Diamond, it was decided that the turboramjet would be used. Two different configurations of the turboramjet were investigated: the wraparound turboramjet and the air turboramjet.

.8.2.1 Wraparound Turboramjet

The wraparound turboramjet is set up much like a conventional afterburning turbojet. The difference is that there is a bypass which contains a burner. Some information was obtained from General Electric about the wraparound turboramjet. This information included some baseline thrust and fuel consumption data for a 6.92 feet diameter engine as well as weights and scaling laws. Unfortunately, this information was not complete enough to do as detailed an analysis as was necessary, thus the basic wraparound turboramjet engine was modelled and a computer program was written so more parameters could be varied.

The wraparound turboramjet was modelled as an ideal afterburning turbojet with a bypass burn added. The specific thrust for the afterburning turbojet was found to be

$$\frac{F}{ma} = M_c \sqrt{\frac{\theta_a}{\theta_o - 1}\left[1 - \frac{\frac{\theta_t}{\theta_o \tau_c}}{\theta_t - \theta_o(\tau_c - 1)}\right]} - M_o$$

The specific impulse for the afterburning turbojet was:

$$I = \frac{a_o h}{g C_p T_o} M_o \frac{\sqrt{\frac{\theta_a}{\theta_o - 1}\left[1 - \frac{\frac{\theta_t}{\theta_o \tau_c}}{\theta_t - \theta_o(\tau_c - 1)}\right]} - 1}{\theta_a - \theta_o}$$

These were the main equations that were used for the wraparound turbojet program. The idealized inlet was also programmed into the computer code. The results obtained for the wraparound turboramjet were as follows. The engine was sized to 6.5 feet in diameter because it was the minimum size that could provide adequate thrust. The Mach number at the compressor face was set to 0.4. This is the present state of the art. The burner temperature was set to 6500 degrees Rankine. This number takes in to consideration advances in material technology. Figure 8-2 shows the gross thrust versus altitude for different Mach numbers. This gross thrust takes into account 17% losses due to skin friction and wave drag as well as losses due to inlet and nozzle inefficiencies.

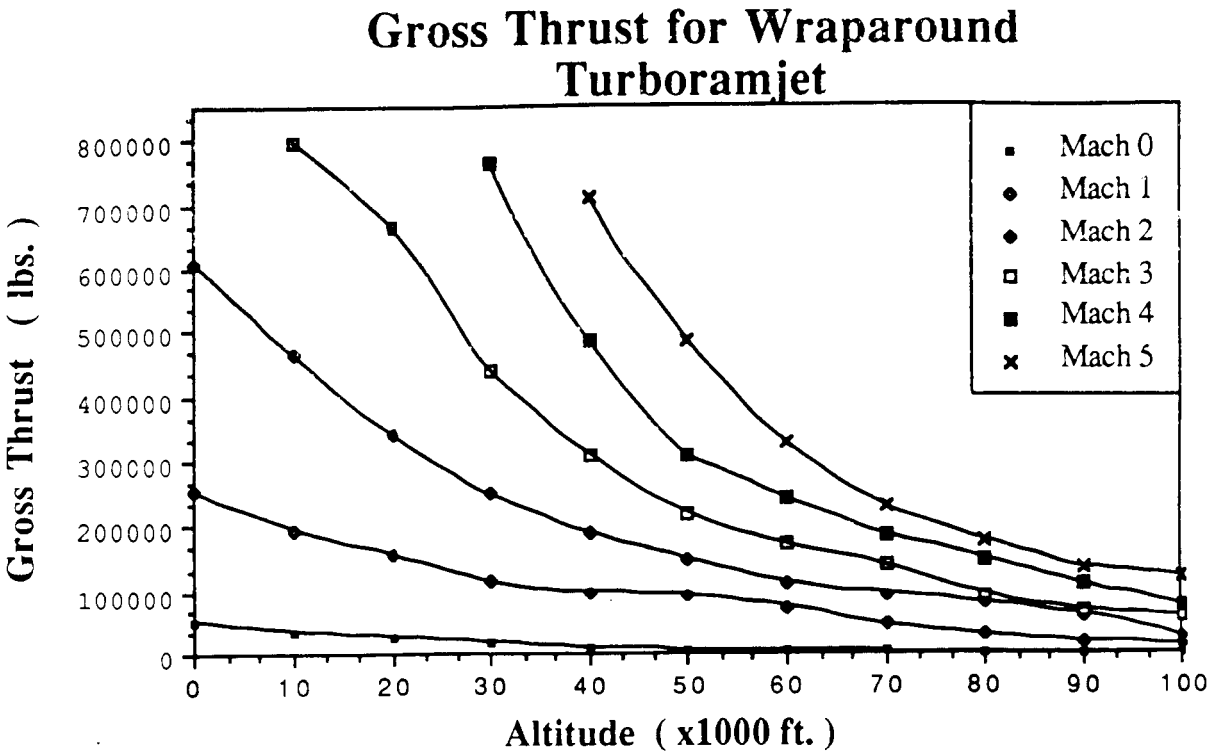

FIGURE 8-2

The next consideration was drag, specifically the ram drag which is the most significant contributor to the reduction in available thrust. Ram drag is the drag incurred due to the compression of the air being processed through the inlet. It is dependent on the amount of air being processed and the speed at which that air is going.

$$\text{Ram Drag} = A_o \, p_o \, \gamma \, M_o^2$$

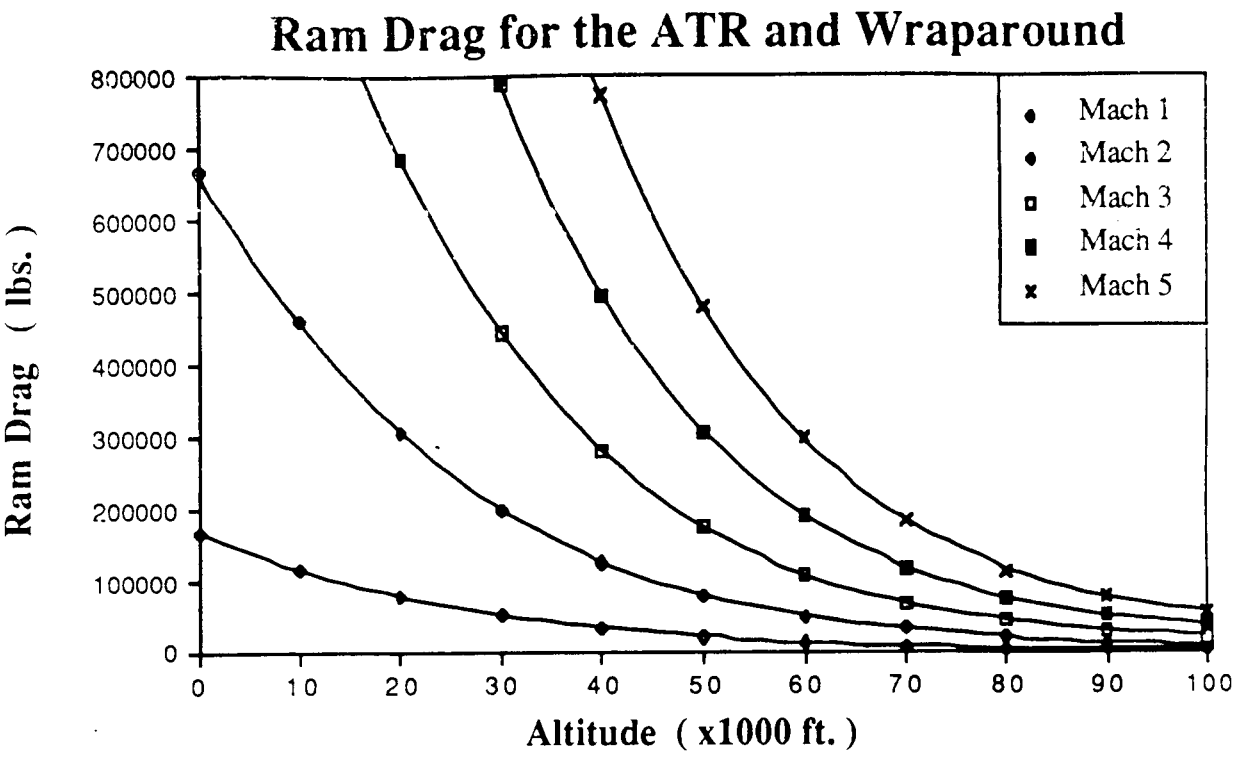

FIGURE 8-3

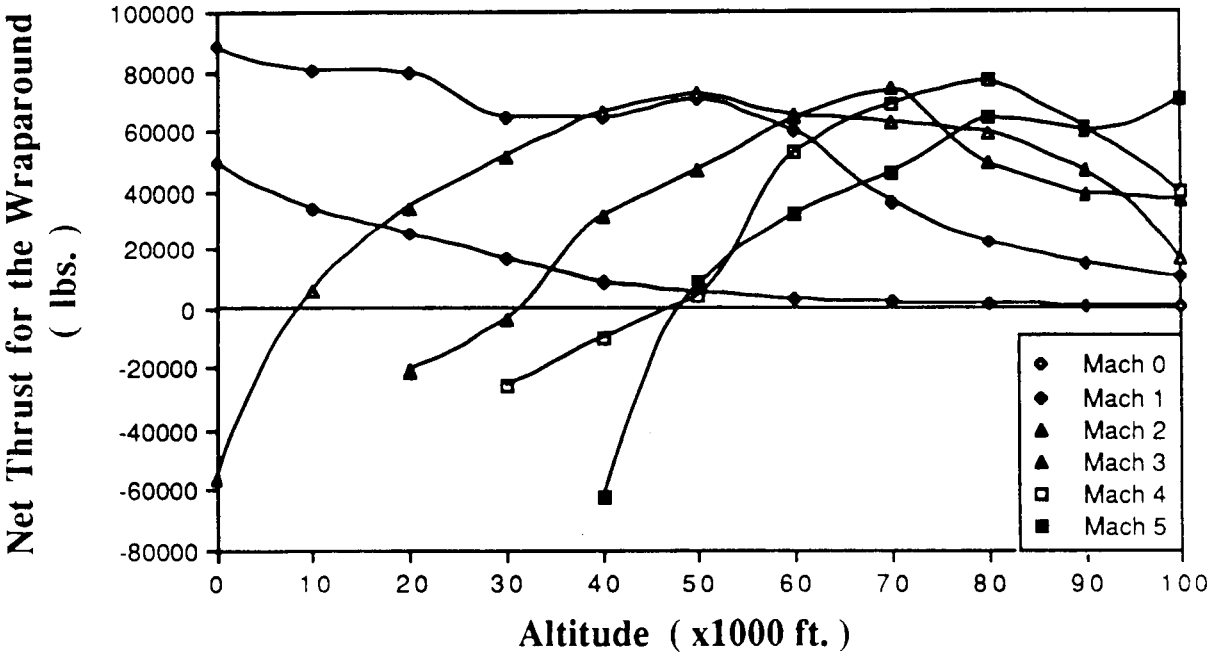

FIGURE 8-4

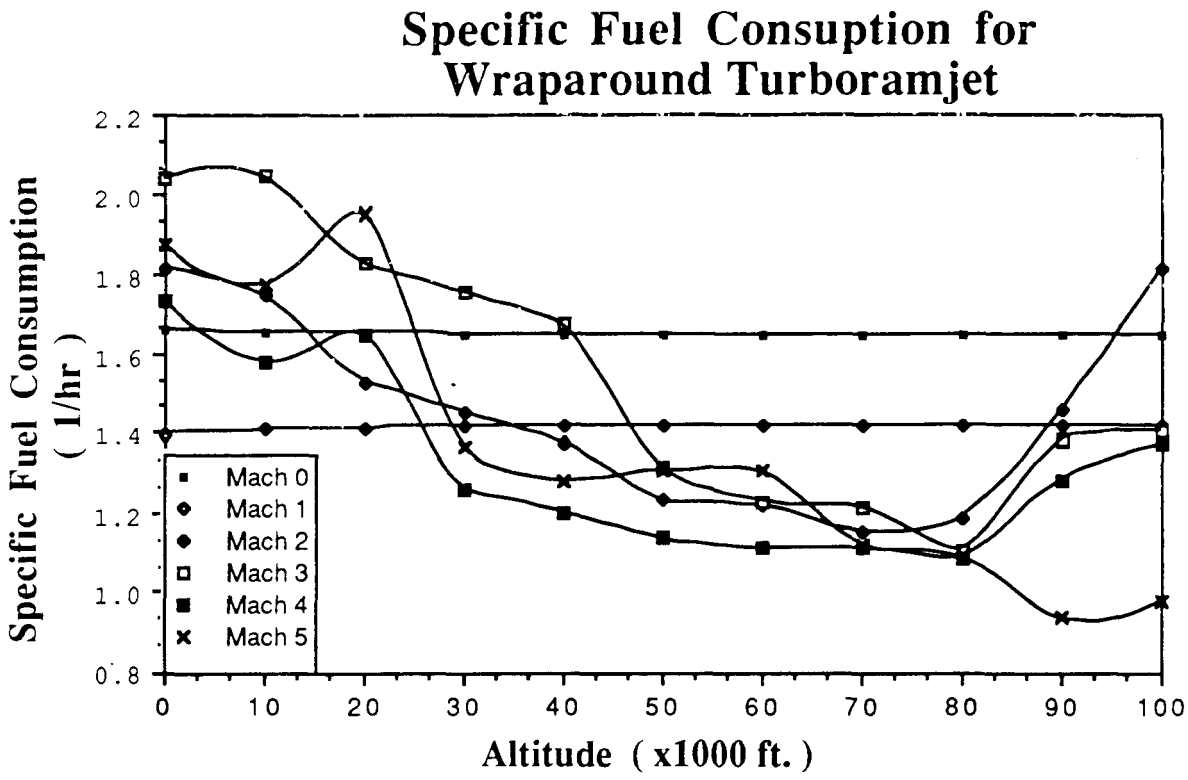

FIGURE 8-5

Figure 8-3 shows the ram drag versus altitude for different Mach numbers. As can be seen , ram drag is a major factor. The ram drag was subtracted from the gross thrust to produce the net thrust. This thrust was the net output of one engine. Figure 8-4 show the net thrust versus altitude for different Mach numbers.

Figure 8-5 shows the specific fuel consumption for the wraparound turboramjet versus altitude for different Mach numbers. Although they appear slightly high, this can be taken care of by advancements in technology. Finally, the weight and the length of the wraparound turboramjet was obtained from the scaling laws and the baseline engine provided by General Electric. The scaling laws used were:

$$W \alpha d^2 \qquad l \alpha d$$

From this, the length of the engine was found to be 13.6 feet and the weight was found to be 8647 lbs. A quick summary of the wraparound turboramjet follows:

$d = 6.5$ feet $\quad l = 13.6$ feet $\quad T_b = 6500$ deg. R.

$M_{c_{face}} = 0.4$ $\quad W = 8647$ lbs.

8.2.2 Air Turboramjet (ATR)

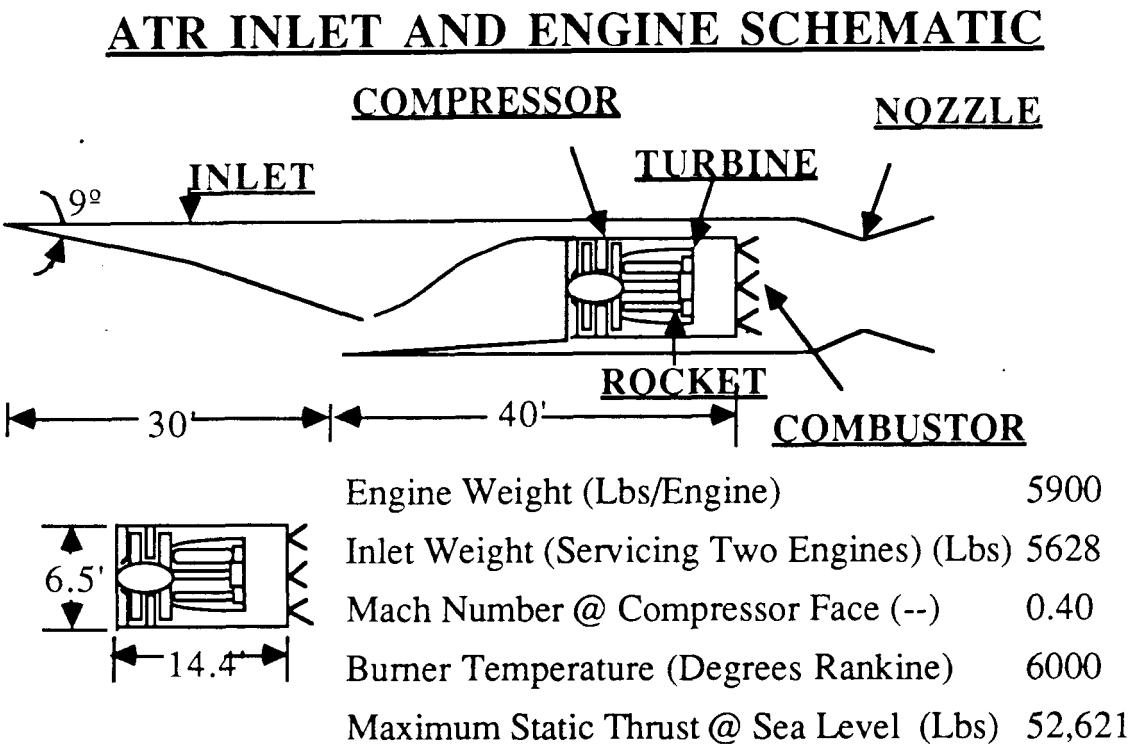

FIGURE 8-6

The other engine considered was the Air Turboramjet or ATR. Figure 8-6 shows a schematic of the ATR. As can be seen , the core contains a compressor driven by a turbine. What is unique is that the turbine is not driven by the airflow through the engine, but rather by rocket engines. Consequently, the compressor performance is not dependent on the engine airflow, and energy is not extracted from the airflow to drive the turbine. The net result is increased thrust performance. The ATR is like a ramjet with the core turbomachinery placed in front of the burner. The core would be run up to Mach numbers around 3. For higher Mach numbers the compressor would simply be feathered and the

ATR would run like a ramjet. Information on the ATR was obtained from Aerojet TechSystems. According to their data, the ATR out performs the turbojet. It also out performs ramjets up to about Mach 5, however above Mach 5 their performance becomes comparable. Because of the very optimistic information presented by Aerojet, further study was conducted. Since more detailed data was not available, a computer program was written to model the ATR.

The ATR was modeled in two parts, the core, and the bypass. For the core the specific thrust equation was

$$\frac{F}{m_4 a_4} = M_4 \left\{ \sqrt{\frac{\theta_{a\rho}}{\theta_4 - 1}\left[1 - \frac{\left[\frac{p_7}{p_4}\right]^{(\gamma-1)/\gamma}}{\theta_4 - \frac{\alpha m_c C_{pc}}{m_t C_{pt}}\left[\frac{T_o \theta_o}{T_4}\left(\tau_c - 1\right)\right]}\right]} - 1 \right\}$$

For the bypass, the specific thrust equation was:

$$\frac{F}{\alpha m_o a_o} = M_o \left[\sqrt{\theta_{aB}\left[\frac{\theta_o \tau_c - 1}{\theta_o - 1}\right]} - 1 \right]$$

The specific impulse was calculated from:

$$I = \frac{F}{g\left(m_{fa}\right)} = \frac{Fh}{\alpha m_o C_{p_{air}} T_o \left(\theta_{aB} - \theta_o\right)}$$

These were the main equations used for the ATR modeling code. The engine was sized to 6.5 feet in diameter to provide adequate thrust. The Mach number at the compressor face was 0.4 which is the present state of the art according to meetings with Lou Young. Taking into account advances in burner and material technology, the burner temperature was set to 6000 degrees Rankine. The results obtained were as follows and include the use of the inlet. The results presented also include losses

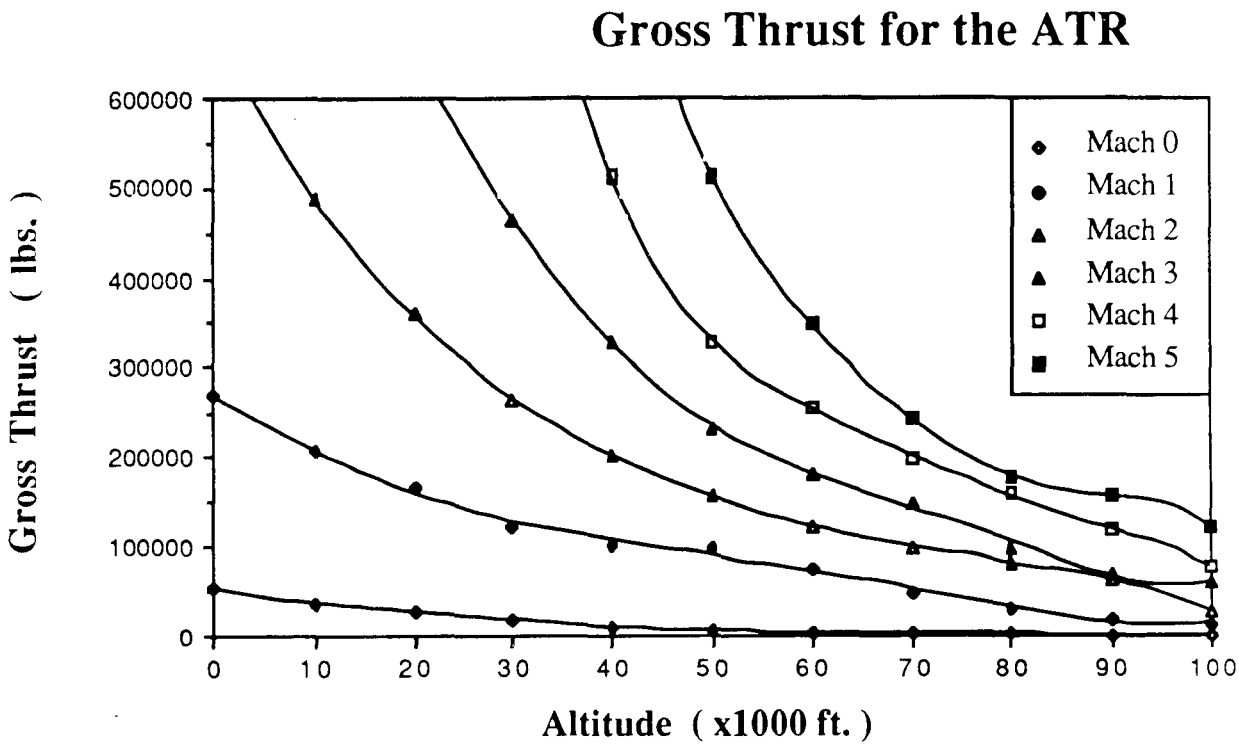

FIGURE 8-7

due to the nozzle (5%) and the inlet (7%) which are from industry standards and analysis. Also, losses due to skin friction and wave drag (5%) were incorporated. Figure 8-7 show the gross thrust versus altitude for different Mach numbers. These may seem quite large, but they are gross thrust values. A significant portion of the gross thrust is lost due to ram drag as explained in section 10.2.1. Because the mass flow ratio for both the ATR and the wraparound turboramjet were the same, the same ram drag was incurred and is shown in Figure 8-3. The ram drag was subtracted from the gross thrust to provide net thrust values shown in Figure 8-8 versus altitude for different Mach numbers. The trends appear accurate and the numbers reasonable for the assumptions made.

Net Thrust Per ATR Engine

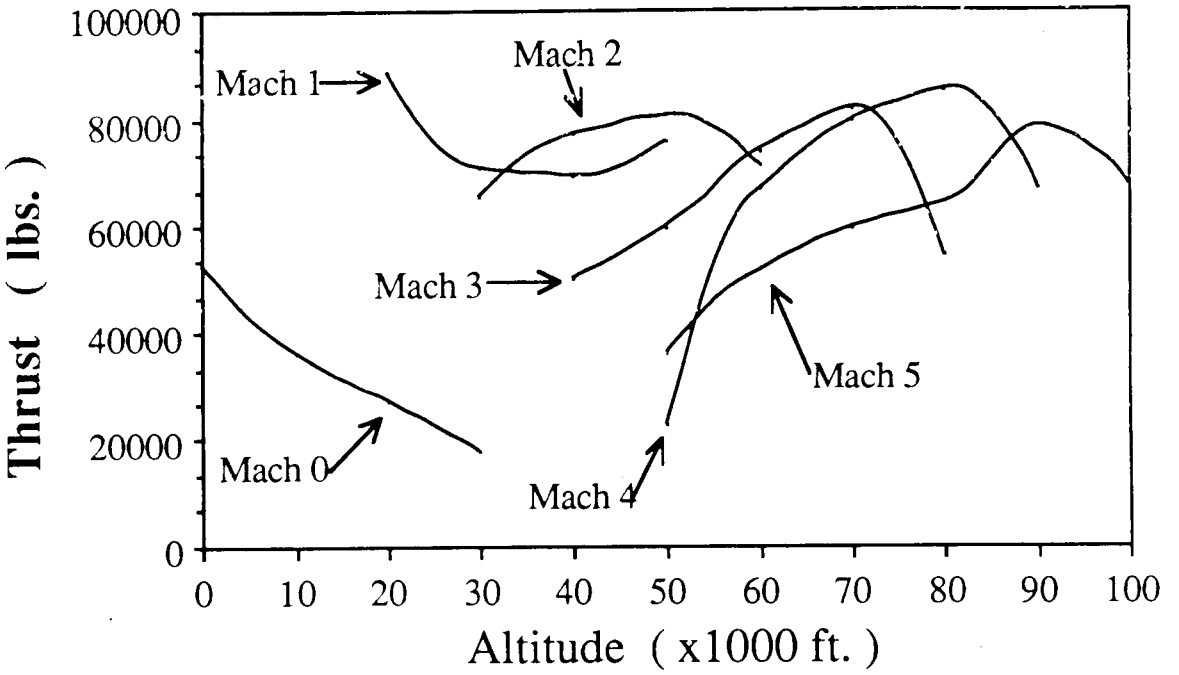

FIGURE 8-8

Specific Fuel Consumption for ATR Engines

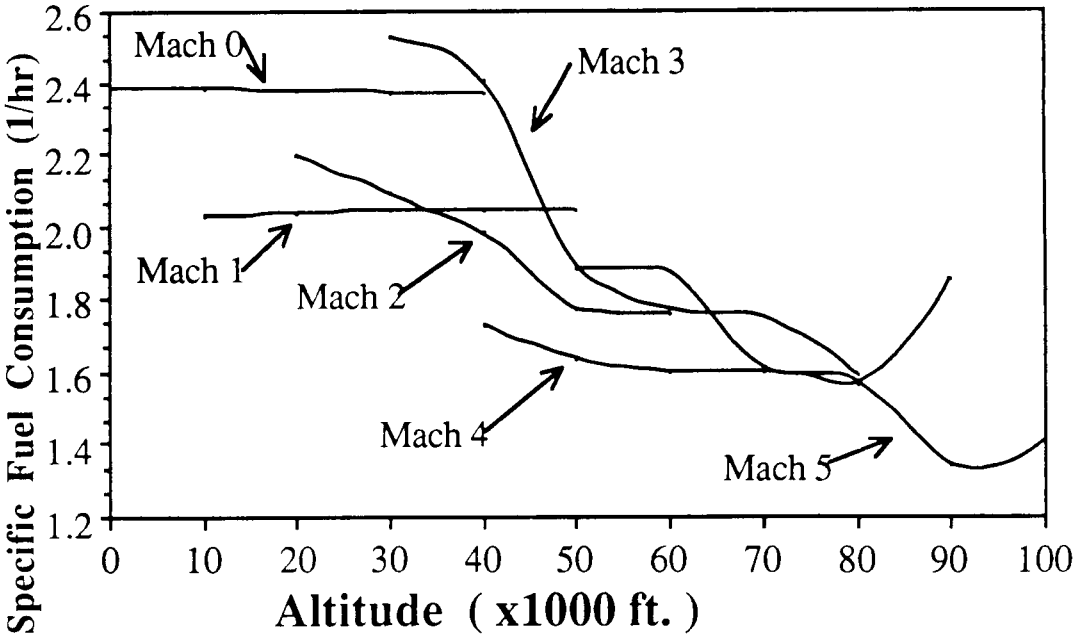

FIGURE 8-9

Next the specific fuel consumption of the ATR was obtained. These are shown in Figure 8-9 versus altitude for different Mach numbers. These were rather high but not too far off from values obtained from Aerojet TechSystems.

The length and weight of the ATR was obtained from scaling laws for turbine engines and information from Aerojet. The scaling laws used were as follows:

$$\text{Thrust} \propto W \quad \text{and} \quad \text{Thrust} \propto l^2$$

The baseline engine used was the GE4/J5. the sea level thrust of the ATR was ratioed with that of the GE4/J5 to obtain the weight and length of a comparable turbojet. Then using the information from Aerojet, the length and weight of the ATR was obtained. The Aerojet information was that an ATR would be one-half the weight and two-thirds the length of a conventional turbojet of the same thrust. This led to a length of 14.4 feet and a weight of 5050 lbs. The weight was increased to 5900 lbs. to account for noise suppression and other auxiliaries. A quick summary of the ATR follows.

$$d = 6.5 \text{ feet} \qquad l = 14.4 \text{ feet} \qquad T_{b} = 6000 \text{ deg. R.}$$
$$M_{c_{face}} = 0.4 \qquad W = 5900 \text{ lbs.}$$

8.3 Engine Selection and Performance

The engine that was selected for the Flying Diamond was the ATR. This engine was selected for two main reasons. First, the ATR has a higher thrust output, and second, the ATR weighs less than the wraparound turbojet. But this selection was not made without a cost. The ATR has a higher specific fuel consumption than the wraparound. If the fuel consumption values generated from the ATR program were used, the Flying Diamond could not meet the range requirements. This is just a reflection of technology. Therefore the specific fuel consumptions were decreased by 20% to account for advances in technology and to more closely match current trends. Another factor that was easy to overlook was that the specific fuel consumptions obtained from the ATR code were for the ATR running at full throttle. As will be shown below , the Flying Diamond does not

require the engines to be run at 100% power the entire flight time. This will further drop the fuel consumption and bring it into a feasible range as shown in Figure 8-10. With these fuel consumptions the Flying Diamond can reach the specified range.

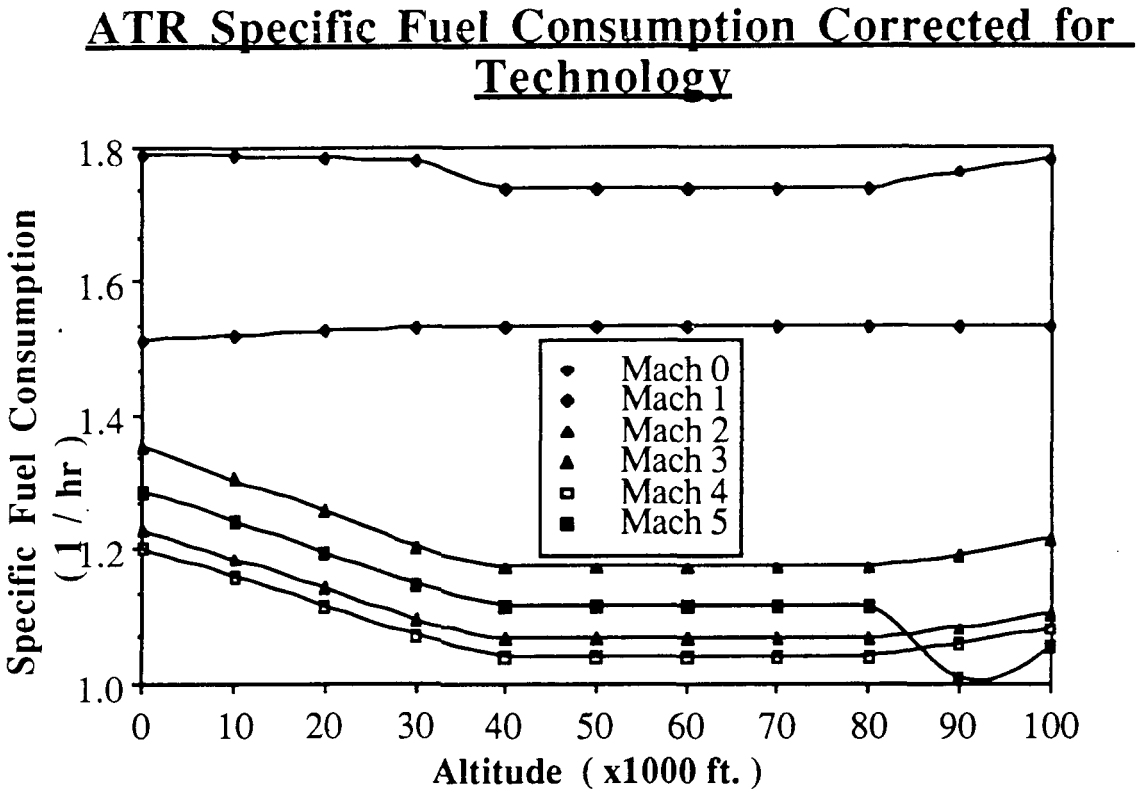

FIGURE 8-10

The Flying Diamond was equipped with four ATR engines. These engines were mounted underneath the fuselage at the tail end. The thrust performance of the engines including inlet, nozzle, and all associated losses is shown in Figure 8-11. This figure shows a typical thrust available and thrust required plot for Mach 4. As can be seen, there is ample excess thrust for the acceleration and climb phases of the aircraft. Thus the ATR does meet all the necessary needs of the Flying Diamond. It can provide the thrust for all phases of flight and the fuel economy needed to satisfy the range.

8.4 Fuel Considerations

Another important consideration involved with the propulsion system was the choice of the fuel. This was important because a large amount of energy would need to be extracted from the fuel in order to obtain the thrust necessary to drive the aircraft. Also, the high speeds of the aircraft and the temperatures incurred in the engines would make active cooling necessary. It would be very beneficial to use the fuel as a heat sink for cooling. Following is a description of the fuels considered.

8.4.1 Methylcyclohexane (MCH)

MCH is an endothermic hydrocarbon fuel. If used, it would undergo a chemical change that would absorb a significant amount of energy. This reaction produces toluene and hydrogen but also

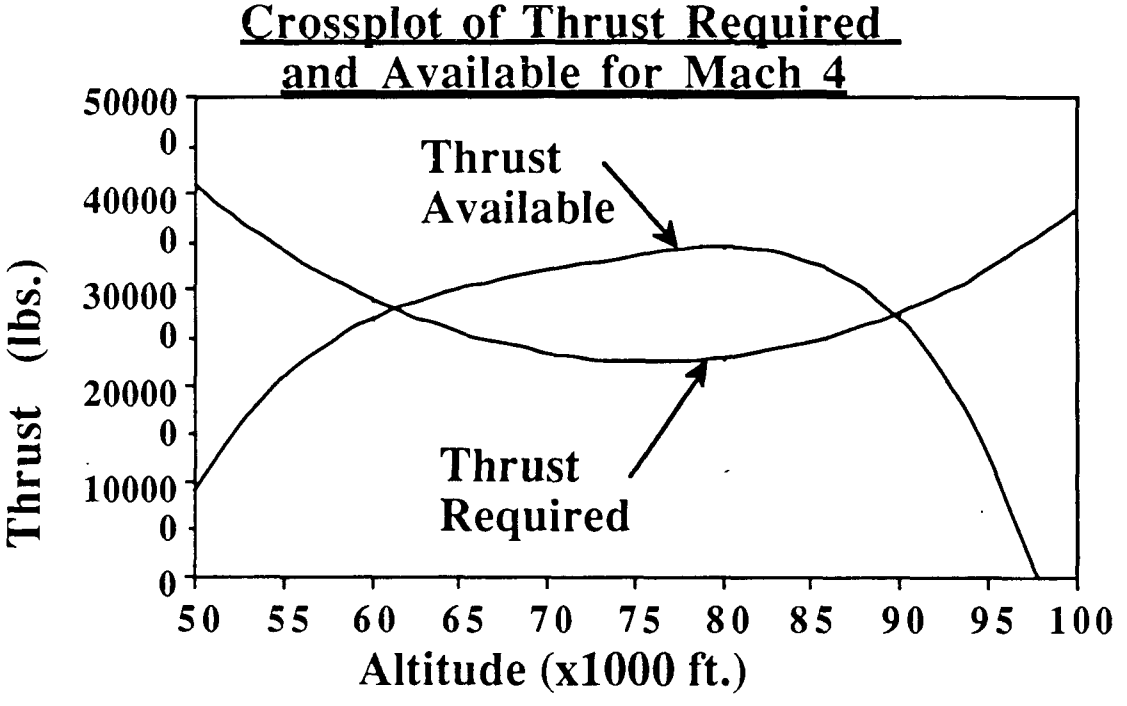

FIGURE 8-11

requires the assistance of a catalyst. MCH was considered because of its high potential operating temperature due to its heat sink potential and thermal stability. However, in order to use the full potential of MCH, it would be necessary to use a complicated, operational, and unproven thermal management system. Also, MCH and its residues are toxic.

8.4.2 JP-7

JP-7 is a high temperature fuel based on the conventional JP fuels. It was considered because it is similar to the JP fuels now in use. Therefore, its use would require little if any changes in existing fueling facilities and fuel systems. However, even though JP-7 was developed to be used at higher temperatures than conventional JP fuels, its heat sinking capacity is still far below that of other fuels as will be shown.

8.4.3 Hydrogen

Liquid hydrogen, as a fuel, provides a substantially better heat of combustion and heat sinking capability. It could easily deliver the necessary thrust and cooling for the Flying Diamond. Unfortunately, liquid hydrogen has a very low density and thus the required volume of fuel would be extremely large. Another complication was that liquid hydrogen is a cryogenic and would require insulation. Finally, liquid hydrogen is not a readily available fuel. Production would have to be started.

8.4.4 Methane (LNG)

Methane or Liquified Natural Gas was another fuel considered. It displayed good heat of combustion and heat sink properties although not nearly as good as hydrogen. Its density is much better than hydrogen's and it is readily available. But, like hydrogen, it is a cryogenic and will pose problems in the fuel tanks due to the low temperatures required and the insulation necessary.

8.5 Fuel Comparison

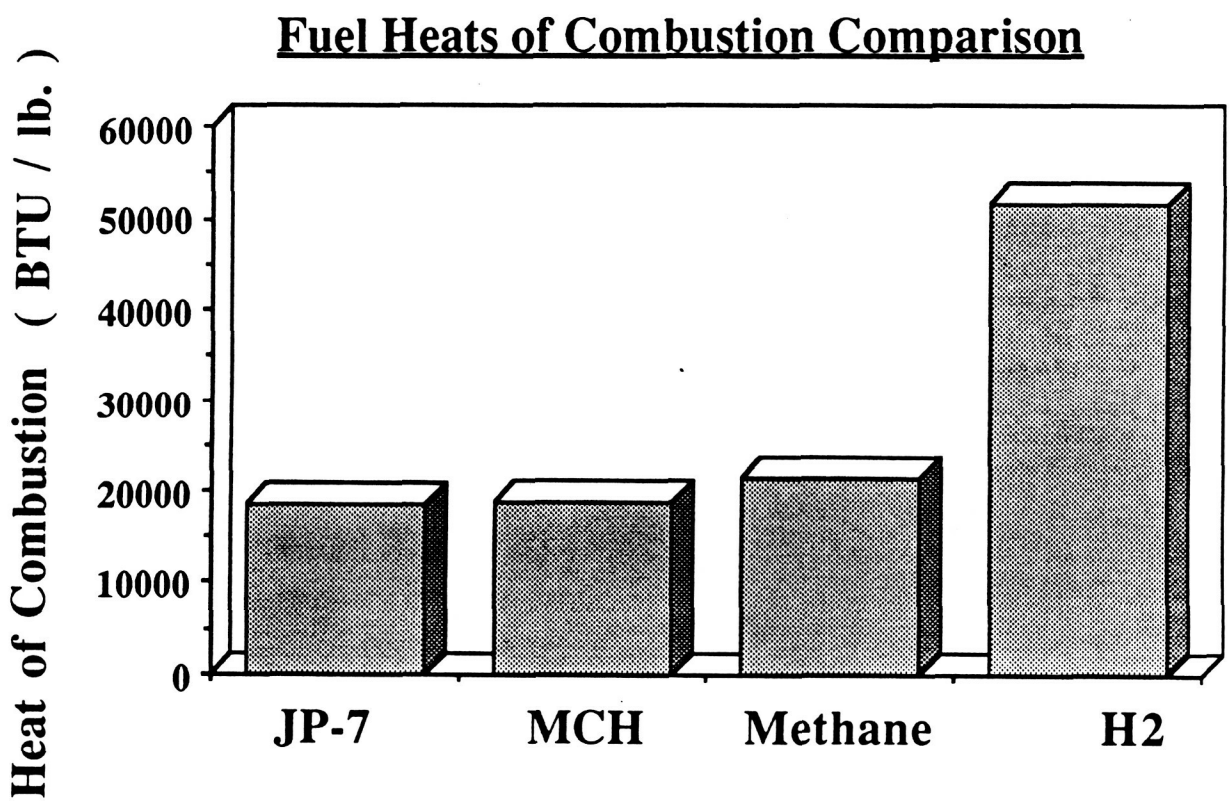

FIGURE 8-12

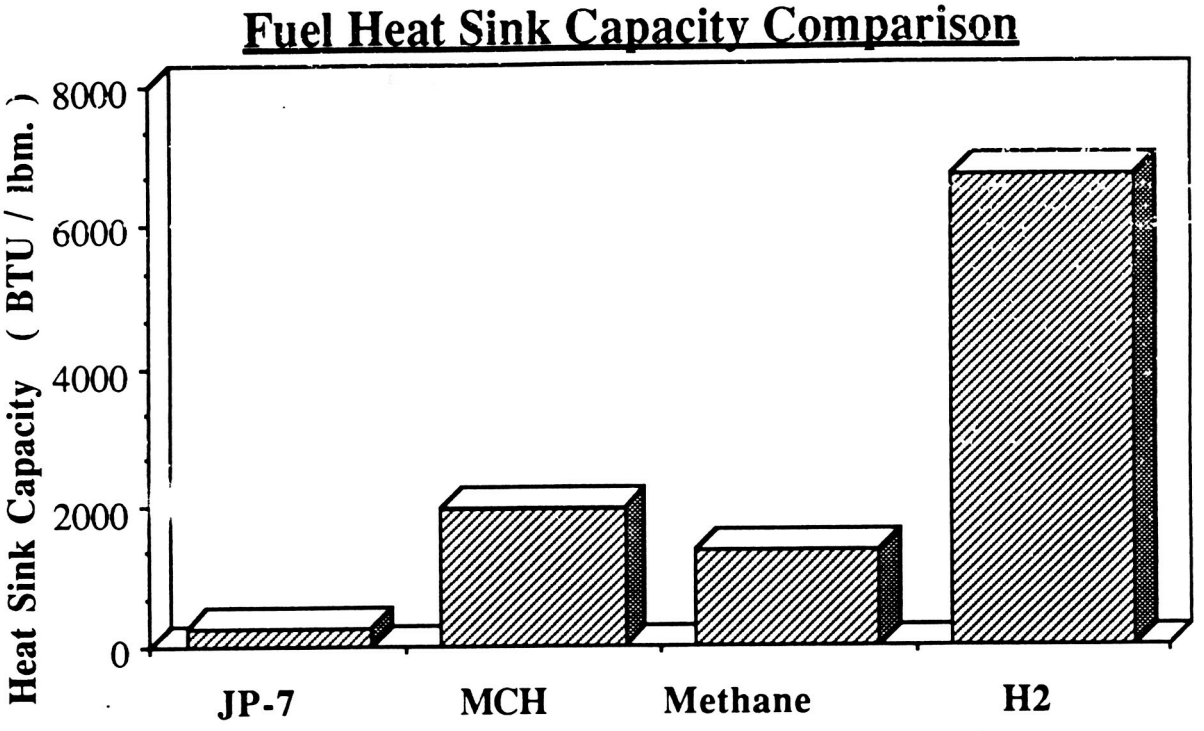

FIGURE 8-13

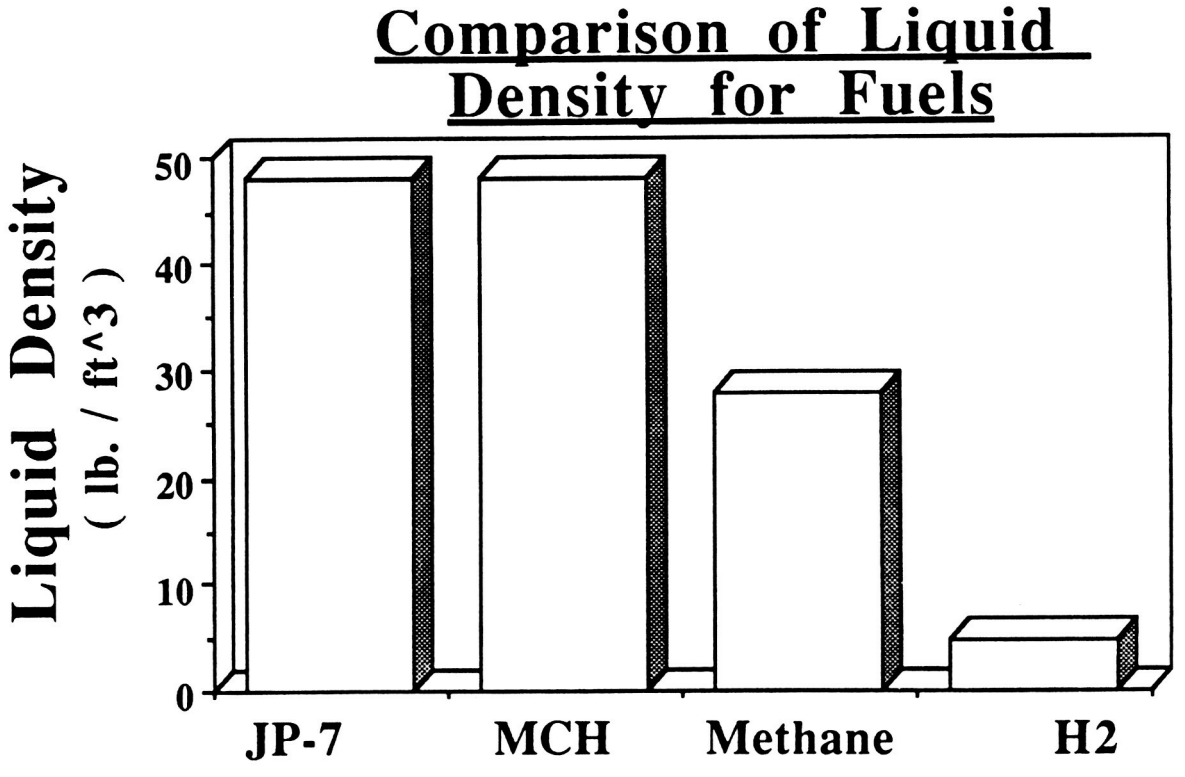

FIGURE 8-14

Several properties of the different fuel considerations were compared: the heat of combustion, the heat sink capacity, and the density. These are shown in Figures 8-12 through 8-14. As can be seen, MCH and JP-7 have comparable heats of combustion with Methane a bit higher and hydrogen well above the rest. The heat sink capacity was clearly dominated by hydrogen. MCH was slightly better than Methane. JP-7 in comparison was very poor. Figure 8-15 shows a comparison of fuel cooling capabilities and aircraft heat sink requirements versus flight Mach number. This shows the Mach number limitations of each fuel with regard to its heat sinking capability. Above the limitation Mach number the fuel could not be used as a heat sink.

HEAT SINK REQUIREMENTS AND FUEL CAPABILITIES

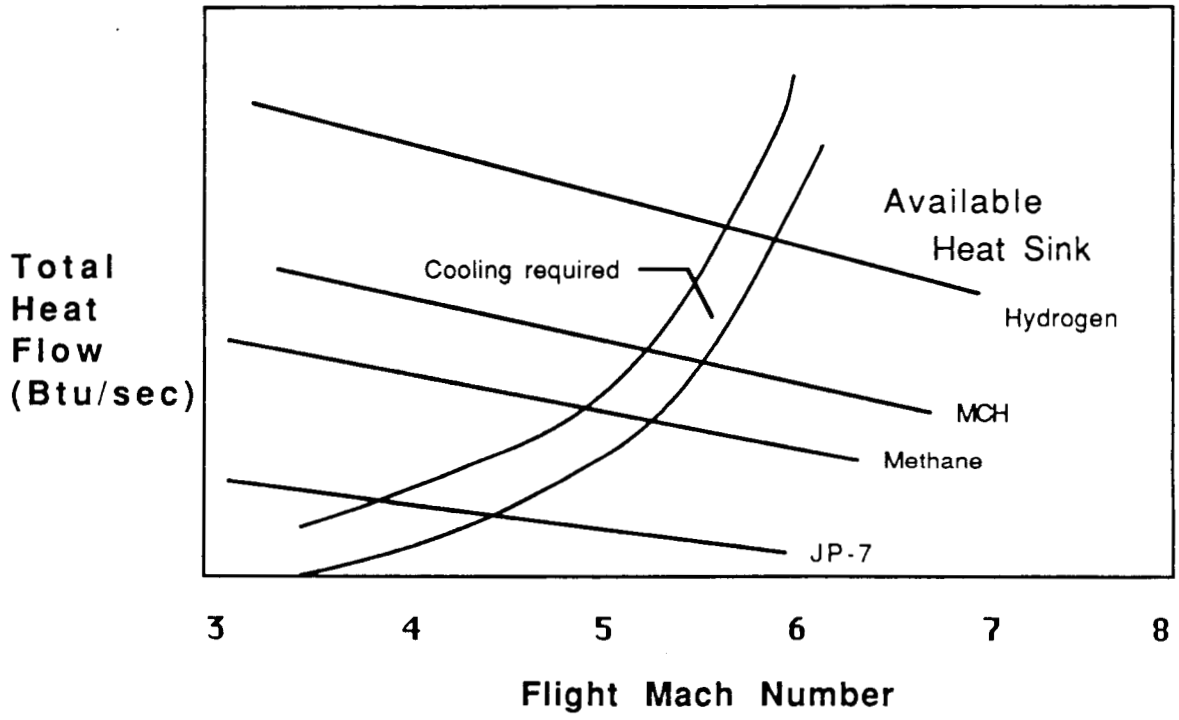

FIGURE 8-15

The next property compared was the density. As shown in Figure 8-14, MCH and JP-7 have comparable densities of 48 lb/ft^3. Methane is a little more than half that at 28 lb/ft^3. Hydrogen is very poor at 4.7 lb/ft^3.

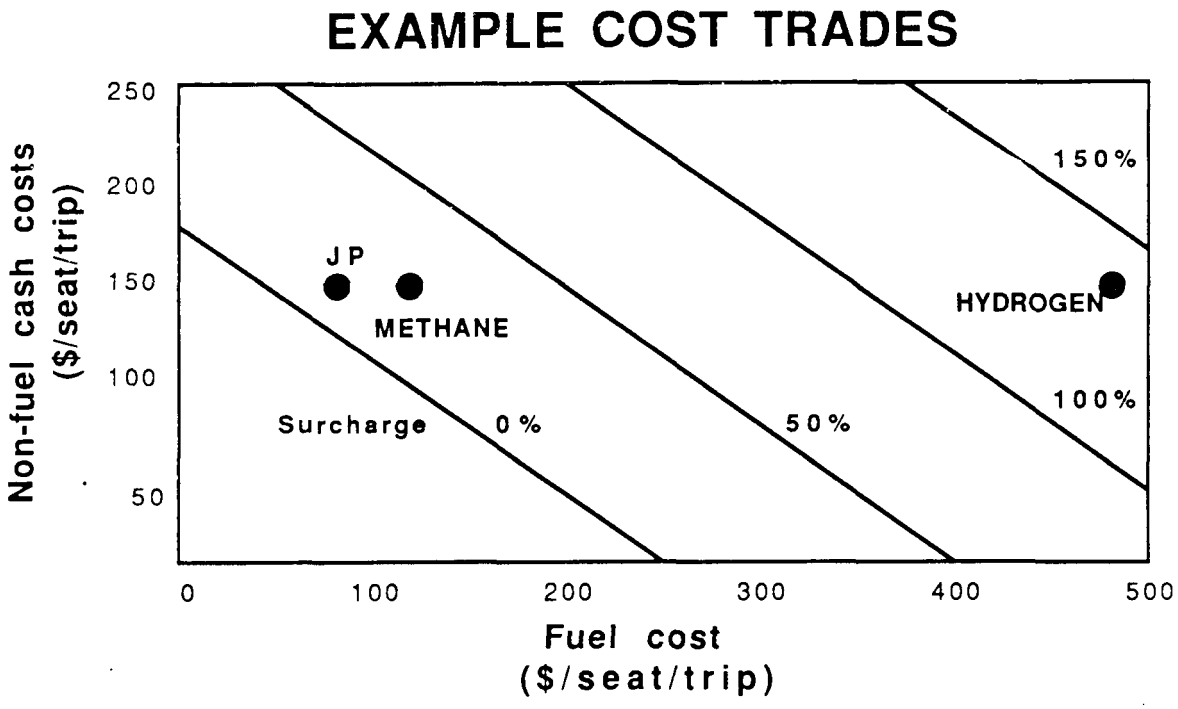

FIGURE 8-16

Finally, an example cost trade study was consulted. Figure 8-16 shows an estimated cost trade for a fixed return on investment for typical HSCT configurations using different fuels. The chart is sectioned with estimated surcharges. JP fuel and Methane would incur surcharges in the neighborhood of 15 to 20 percent while hydrogen would incur a surcharge of better than 120 percent.

MCH was eliminated as a fuel choice because of the complexity and unproven thermal management system that would be necessary and because the fuel and its residue are toxic. JP-7 was eliminated because its heat sink capacity would make it necessary to devise a completely independent cooling system for the aircraft and for the fuel itself. Liquid Hydrogen was eliminated because its density was so low that it would require a prohibitively large fuel volume. Also the use of hydrogen would incur a very large surcharge making the aircraft financially unfeasible.

It was decided to use Methane as the vehicle fuel. Methane has a better heat of combustion than either MCH or JP-7. Its heat sink capacity is much better than JP-7, and although it is not quite as good as MCH and much worse than Hydrogen, it is adequate for the expected

speed range. Methane is non-toxic unlike MCH. Methane has a density that is a little better than half that of MCH and JP-7, and it is more than five times as dense as hydrogen. Finally, the surcharge incurred would be in the same neighborhood as that of JP-7 and much less than hydrogen. Even though Methane is a cryogenic, it was determined that tanks and insulation could be designed to handle the low temperatures. Therefore, Methane was chosen as the fuel for the Flying Diamond because it presented the best compromise between properties, storage, and cost.

8.6 Nose Shock

In determining the airflow into the inlet, the shock wave from the nose of the aircraft must be considered. The Flying Diamond, the lower portion of the nose has an angle of 13.5 degrees as shown in Figure 4-6. For this analysis the nose was treated as a wedge in order to simplify calculations. The error is expected to be slight because idealized conditions were assumed for the wedge.

Using oblique shock theory, the Mach number behind the nose shock was found from the nose angle d, the shock wave angle q, and the freestream Mach number M_o. First the normal Mach number was found from
$M_{n_o}=M_o \sin \theta$ in which q was obtained from NACA 1135. Using M_{n_o}, values for $\frac{P_1}{P_o}$ and $\frac{\rho_1}{\rho_o}$ were obtained from NACA 1135. Then the Mach number behind the nose shock was obtained from

$$M_1 = \frac{M_{n_o}}{\sin(\theta-\delta)}.$$

With this information, the total pressure loss was calculated.

$$\frac{P_{t_1}}{P_{t_o}} = \left(\frac{P_{t_1}}{P_1}\right)_{M=M_1}\left(\frac{P_1}{P_o}\right)_{M=M_{n_o}}\left(\frac{P_o}{P_{t_o}}\right)_{M=M_o}$$

At the place where the nose curves into the fuselage, a Prandtl-Meyer expansion was assumed. From M_1 and NACA 1135, ν_1 was found. Then ν_2 was calculated from

$$\nu_2 = \nu_1 + \delta$$

Using ν_2 and NACA 1135, the value for M_2 was found. This would be approximately the Mach number that the inlet would see. Since a Prandtl-Meyer expansion was assumed, $P_{t_2} = P_{t_1}$. The density ratio across the expansion was found from

$$\frac{\rho_1}{\rho_2} = \left(\frac{1 + \frac{\gamma - 1}{2} M_2^2}{1 + \frac{\gamma - 1}{2} M_1^2} \right)^{1/\gamma - 1}$$

Then the density ratio for the inlet entrance to the freestream was obtained from

$$\frac{\rho_2}{\rho_o} = \frac{\rho_2}{\rho_1} \frac{\rho_1}{\rho_o}$$

Figure 8-17 shows the Mach number seen by the inlet versus the freestream Mach number. Figure 8-18 shows the total pressure recovery versus the freestream Mach number. Finally, Figure 8-19 shows the density ratio at the inlet versus the freestream Mach number. These properties would be used for the inlet calculations.

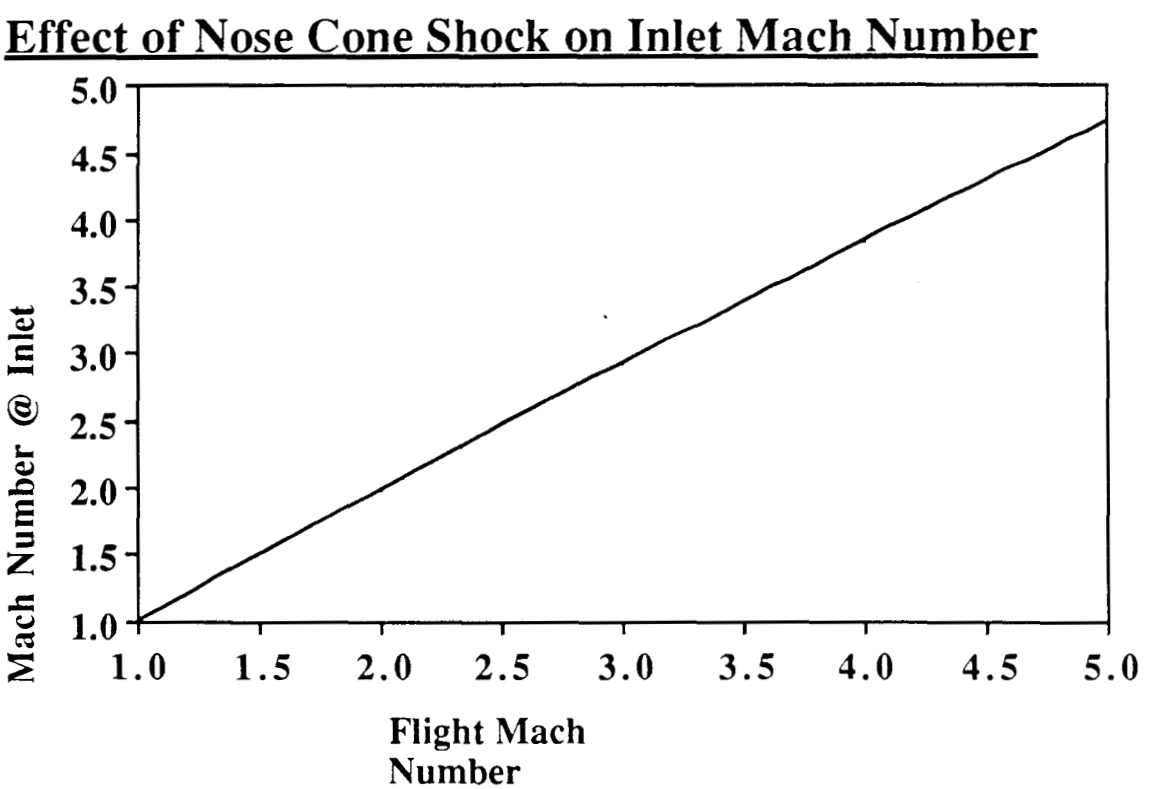

FIGURE 8-17

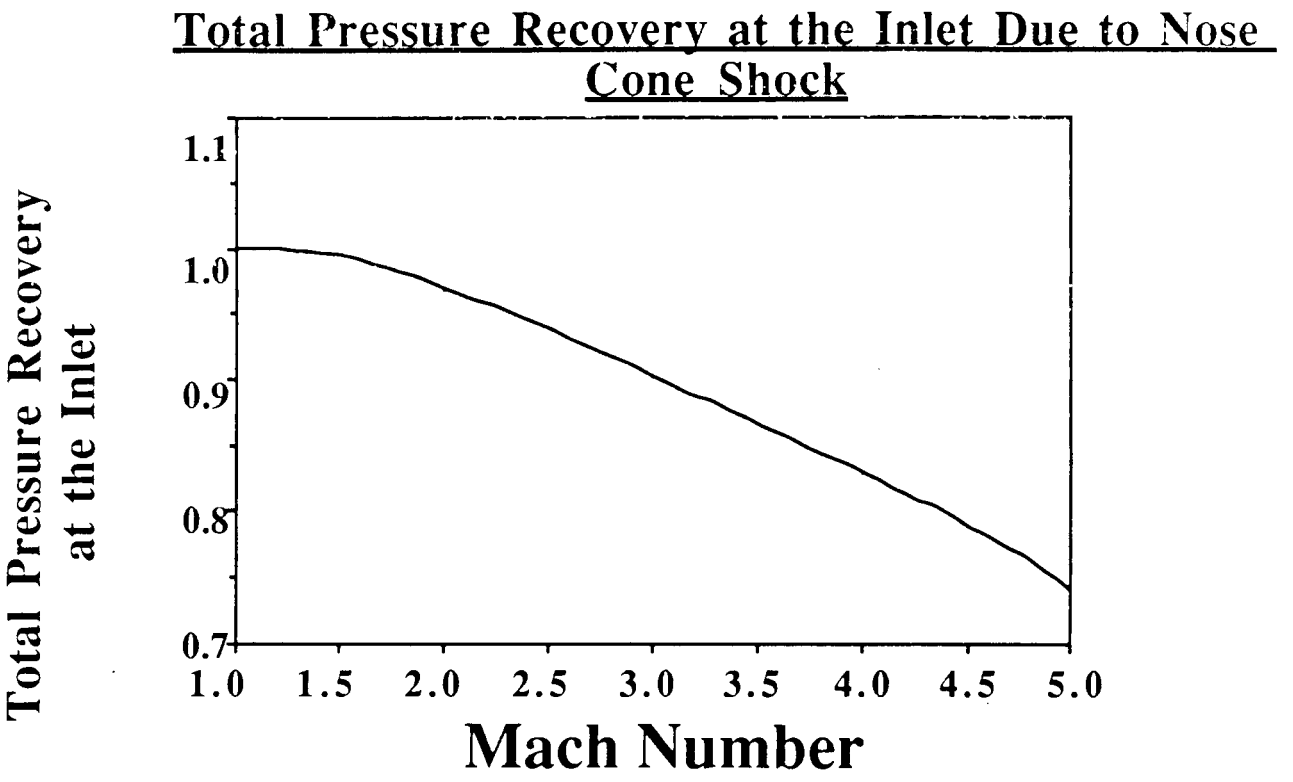
Total Pressure Recovery at the Inlet Due to Nose Cone Shock
Total Pressure Recovery at the Inlet
1.1
1.0
0.9
0.8
0.7
1.0
1.5
2.0
2.5
3.0
3.5
4.0
4.5
5.0
Mach Number

FIGURE 8-18

Convergent/Divergent Fixed Geometry Nozzle:	Poor off-design performance, unstable in highly under-expanded conditions.
Convergent/Divergent Variable Geometry Nozzle:	Good off-design performance, but heavy and complex.
Plug Nozzle with very cooling difficulties.	High cruise and off-design efficiency, but Variable Geometry: heavy and there are plug
Ejector Nozzle:	Good cruise and off-design efficiency, light, simple thrust reverse capability. The Concorde uses this type of nozzle.

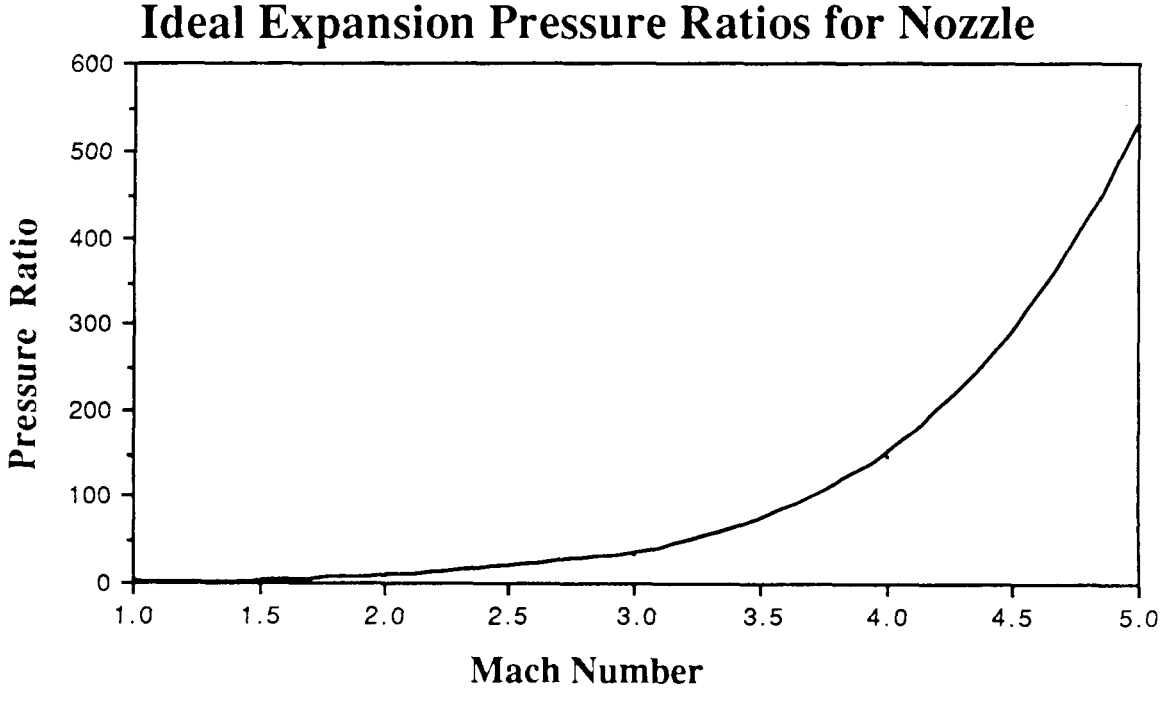

FIGURE 8-20

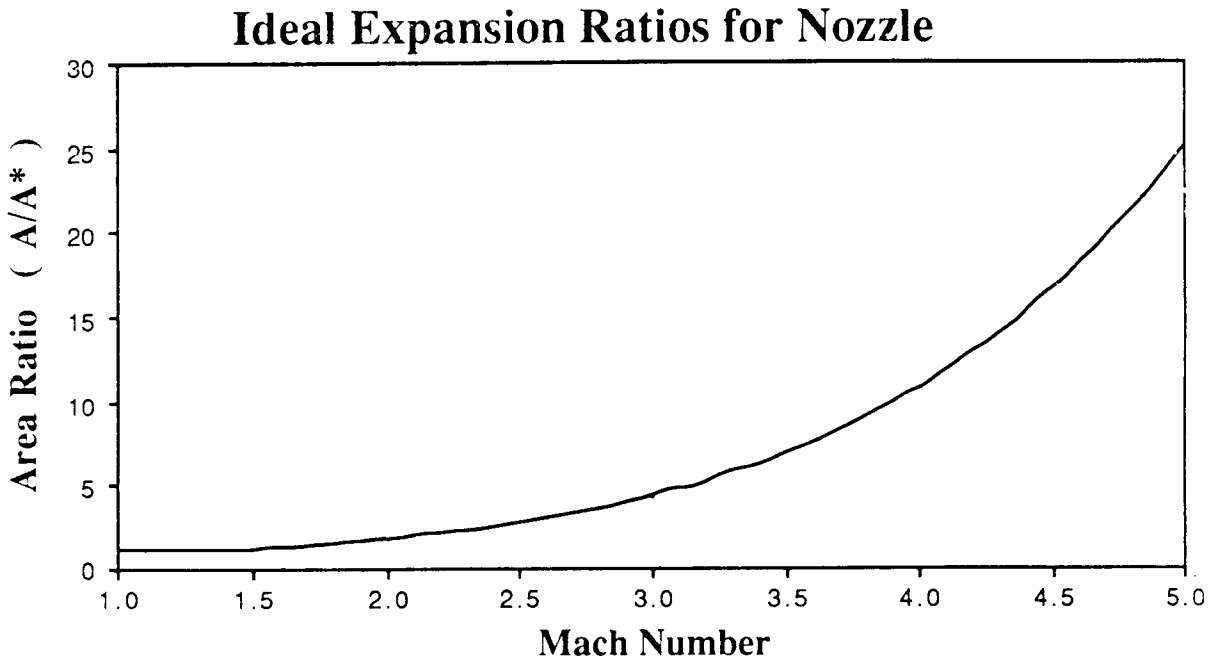

FIGURE 8-21

Since a large range of area ratios will be required for efficient on and off design performance, a variable geometry, 2-dimensional convergent/divergent (2D-CD) nozzle was selected. The 2D-CD configuration will minimize the complexities and corresponding heavy weights associated with an axisymmetric CD nozzle since it only has 4 major moving parts- two convergent flaps and two divergent flaps. The 2D-CD nozzle will also minimize the interference penalties and allow better integration with the aft fuselage when compared to other nozzle types. This is because the two dimensional exit will conform to the flat portion of the aft fuselage. Although this nozzle is not used on any aircraft today, a large amount of research has been performed and even a full scale working model (ADEN) has been developed with favorable results .

The nozzle geometry was determined from parametric analyses involving nozzle thrust performance and weight. According to Mr. Lou Young, a small increase in nozzle thrust coefficient will result in a much higher engine thrust. Obtaining a high nozzle thrust coefficient was found to be difficult.

Although a large area ratio is desired for high thrust coefficients, the weight penalties for the nozzle lengths needed prohibits any value greater than 4. An optimum area ratio of 3 was selected because of its good performance and weight properties.

From this analysis, the thrust coefficient is seen to be relatively constant and the primary nozzle lenght decreases as the primary nozzle half angle increases. By reviewing other aircraft nozzle geometries and considering the application to the Diamond, a value of 30^{o} was selected as optimum.

From this analysis, the nozzle thrust coefficient can be seen to increase with decreasing secondary nozzle half angles. This is because there are less losses associated with angularity. This increase in performance is offset by the requirements of longer nozzles which result in a high nozzle weight. From this analysis, a value of 15^{o} was selected as the optimum. The final nozzle configuration is shown in Figure 8-22.

8.7.3 Nozzle Operation

The 2D-CD nozzle will provide efficient operation from the low subsonic speeds up to the high Mach number cruise speeds. The flexibility of variable geometry combined with a large throat-to-exit area ratio capability allows the nozzle to expand the exhaust efficiently. The 2D-CD nozzle will be configured as a convergent nozzle for subsonic operation, will open wide at Mach 1, and become a convergent/divergent nozzle at speeds greater than Mach 1 as shown in Figure 8-23.

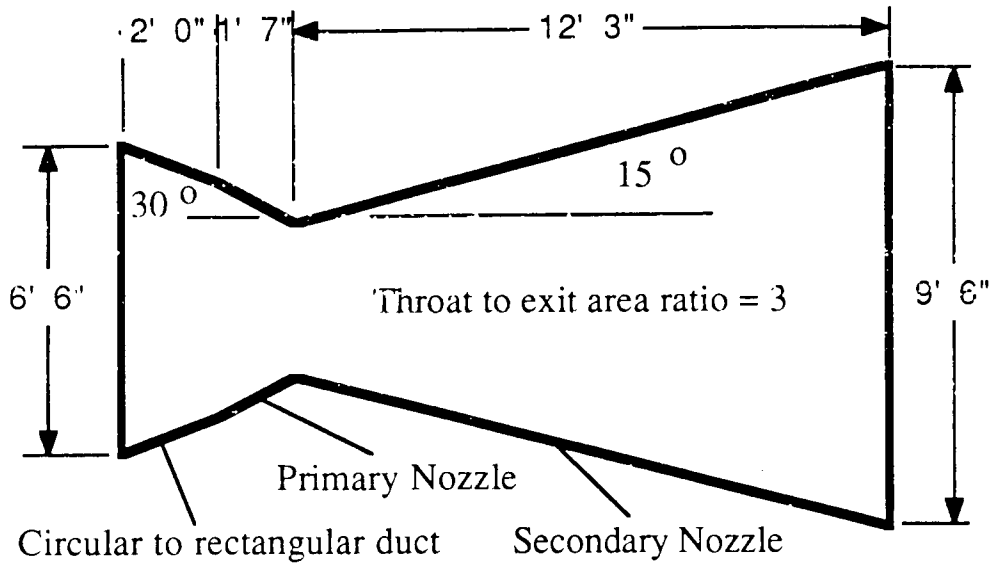

FIGURE 8-22

Nozzle Configurations for Various Conditions

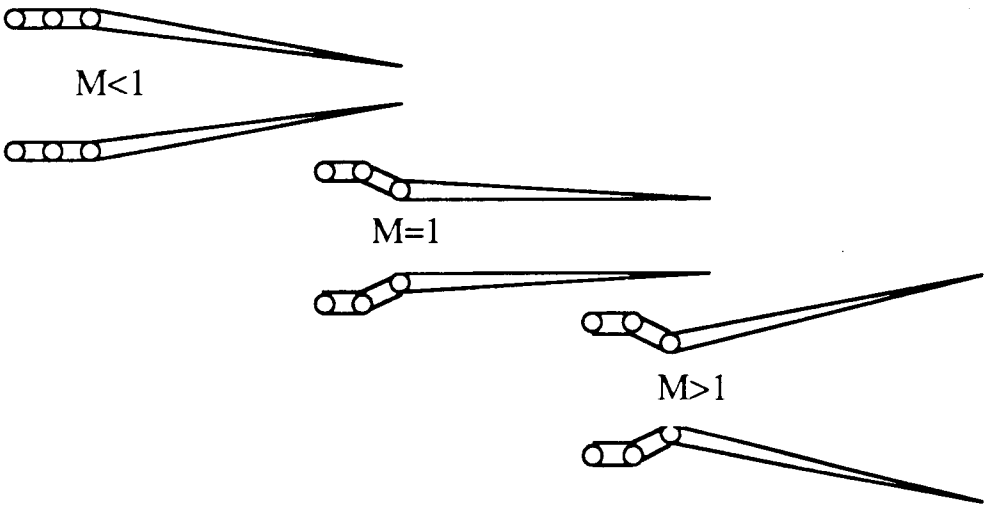

FIGURE 8-23

8.7.4 Nozzle Performance

The performance of the nozzle was determined with considerations for losses due to friction, flow angularity, expansion, leakage, cooling air throttling, and off-design performance. A method to determine the losses due to friction, angularity and expansion given in Reference 11 was used.

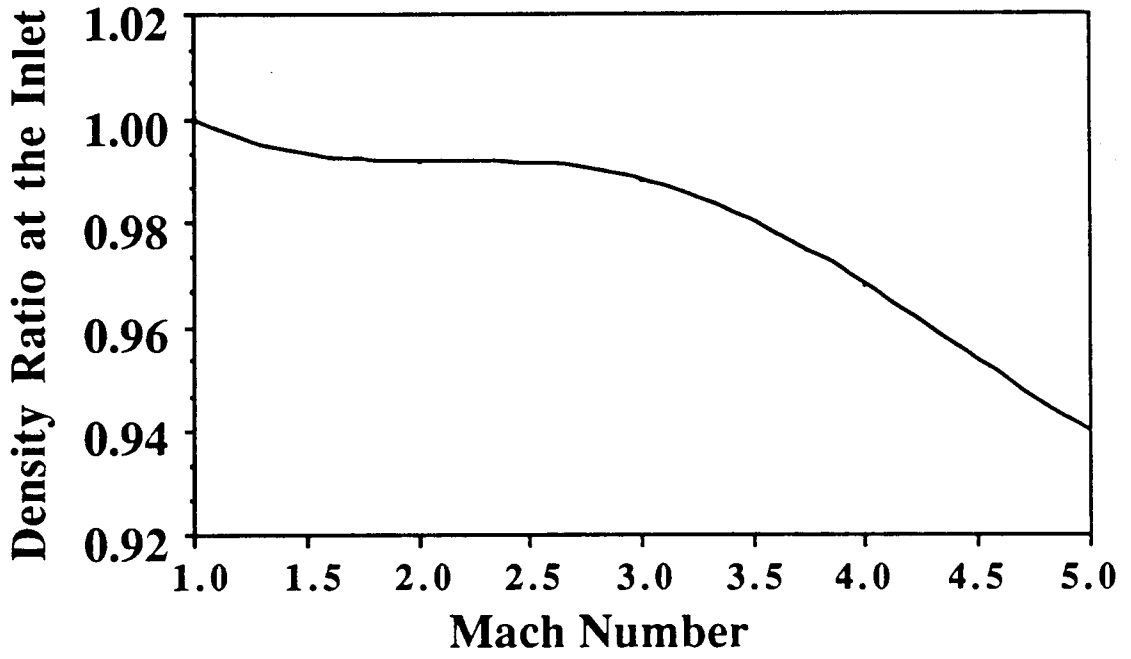

FIGURE 8-19

8.7 Nozzle Integration

8.7.1 Introduction

The function of the nozzle is to expand the exhaust gases to a pressure equal to the atmospheric value. This can not be done for the HSCT because of the high Mach number regime in which it operates. The pressure ratios and the required area ratios are too large (Figures 8-20 and 8-21) for efficient expansion. A nozzle that did this would be tremendously heavy and would have very high drag penalties. On the other hand, a short, lightweight nozzle would be too inefficient. For these reasons, nozzle integration with the aft airframe was determined to be critical for the HSCT.

8.7.2 Nozzle Configuration

There are a number or different nozzle types, each with their own good and bad qualities. These are summarized below:

Simple Convergent Nozzle: Good for subsonic cruise and short dashes at high speeds. Extended supersonic cruise is too inefficient.

The leakage and cooling air throttling losses were estimated to be 1%, which is a valid according to Reference 19. Off-design performance (incomplete expansion) will occur throughout the cruise portion of flight. This is due to the high speeds and altitudes at which the Flying Diamond will be operating. This is why afterbody expansion is needed. For the 2D-CD nozzle, the side which will have increased expansion provided by the afterbody will incur only small losses. However, the other side, which is not allowed to fully expand, will experience large losses. This off-design performance was determined using the Prandtl-Meyer expansion wave function.

The thrust coefficients for various flight conditions are shown in Figure 8-24. From this figure it is found that the highest losses arise from off design performance. The thrust coefficient at cruise was determined to be 0.951, which allows the Flying Diamond to operate at a cruise speed of Mach 4.5.

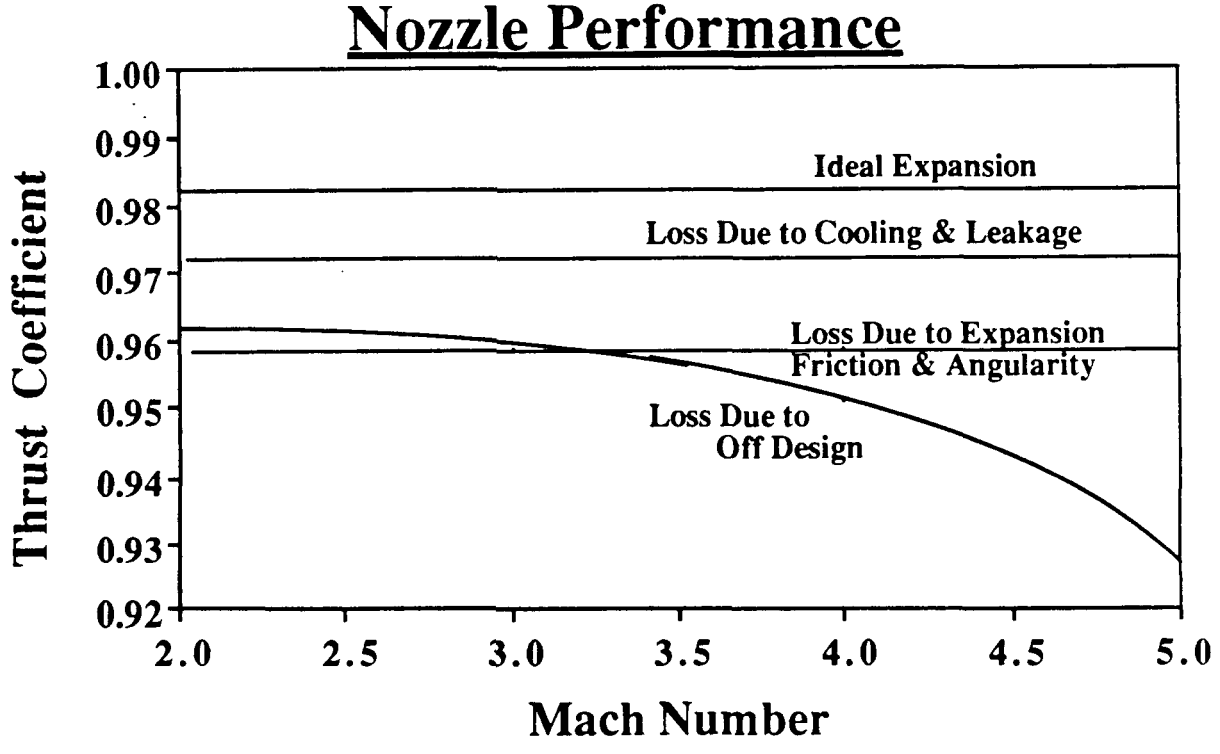

FIGURE 8-24

8.7.5 Nozzle / Aft Fuselage Cooling

The temperatures within the nozzle are expected to be considerably high since the burner is operating at a temperature of 7000°R. Because of this, no exhaust gases may be allowed to come into contact with the nozzle walls or fuselage afterbody. With this consideration, the nozzle will be cooled by a film of cool air injected into the flow at various locations. This will be accomplished by a number of panels with cooling holes on the surface (Figure 8-25).

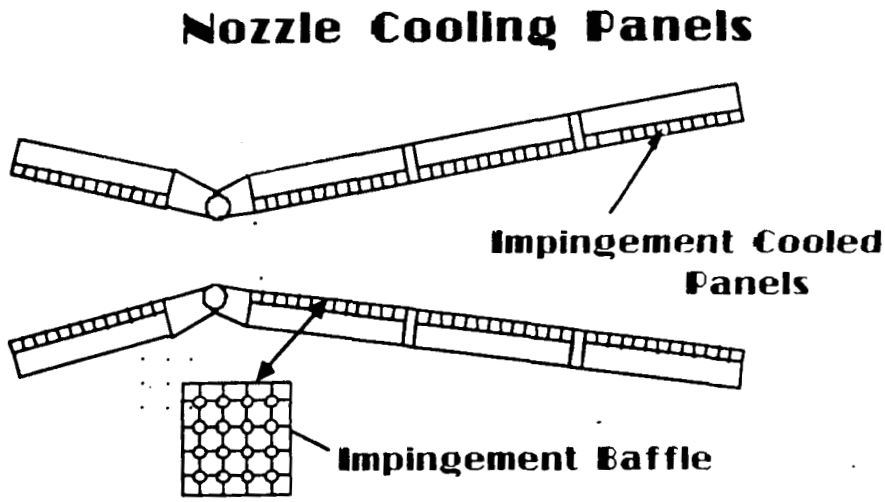

FIGURE 8-25

The cooling air will come from bleed air, which will be first cooled by the fuel. A rough estimate of the bleed air required is 10% of the total flow. This amount can be supplied by the inlets. The aft fuselage section will employ active cooling along all panels subjected to the nozzle exhaust (Figure 8-26).

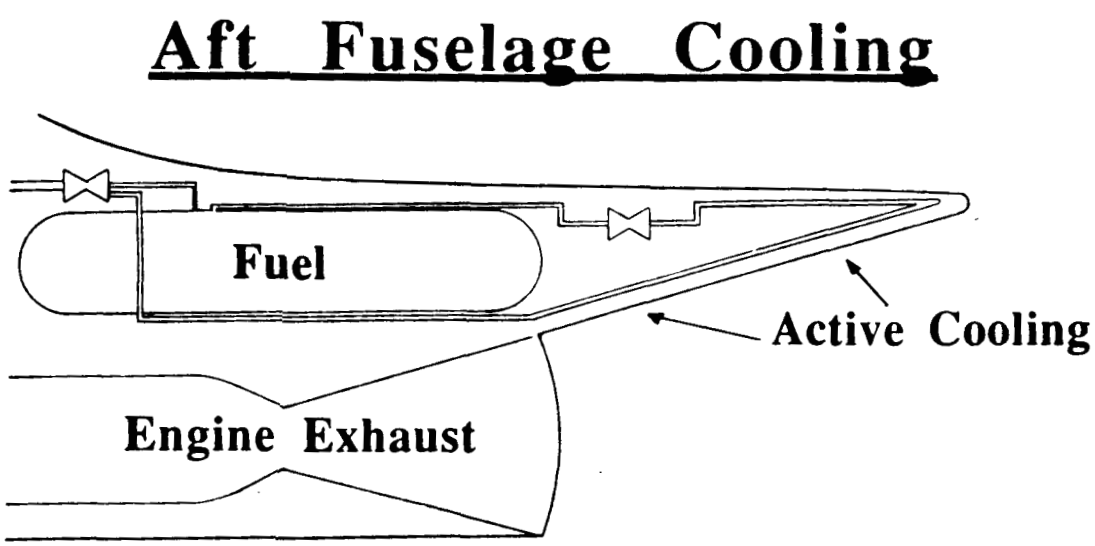

FIGURE 8-26

8.8 Inlet

The inlet for the Flying Diamond was a major undertaking. Several ideas were proposed at the start of the design. These included 2-dimensional and axi-symmetric inlets with internal, external, or mixed compression. Much time was spent discussing the relative benefits and drawbacks to the different types of inlets. The most simplistic inlets, that is fixed geometry with either internal or external compression, were quickly eliminated due to the wide speed range of the aircraft. At off design flight conditions the penalties in performance would easily outweigh any benefits obtained form the structural and mechanical simplicity. In order for the engines to perform well, specifically, to provide the necessary thrust for aircraft performance, throughout the entire flight regime, a certain amount of air must be delivered to the engines. Because of the wide speed range, a variable geometry inlet with mixed compression became a necessity.

The next decision was to choose between an axi-symmetric or a two-dimensional inlet. The axi-symmetric inlet would be more efficient and could be varied in geometry by a translating spike. but the problem encountered with this type of inlet was integrating it into the fuselage. The axi-symmetric inlet, because of its shape, would add to the drag of the aircraft due to poor integration and that would more than account for any increase in efficiency. Thus, it was decided to use a two-dimensional inlet because it could be effectively integrated into the fuselage and still provide adequate performance. The added total pressure loss through the two-dimensional inlet does not translate directly into thrust loss because of the high energy of the air flow. Consequently, a higher efficiency penalty could be paid without a proportional penalty in thrust performance.

The inlet used on the Flying Diamond was developed as follows. The mass flow rates of the engines were obtained from the ATR program described earlier. These were then transformed into capture areas by:

$$A_C = A_O = \frac{m}{\rho_O V_O} = \frac{m}{\rho_O M_O a_O}$$

Figure 8-27 shows the capture area versus Mach number for different altitudes. From this chart the inlet capture area was sized to 70 square feet to allow for bleed air. In order to best meet the width of the Flying Diamond, the inlet opening was sized to 7 feet wide by 10 feet high. The basic configuration and length of the inlet was a trade-off between simplicity, efficiency, and weight.

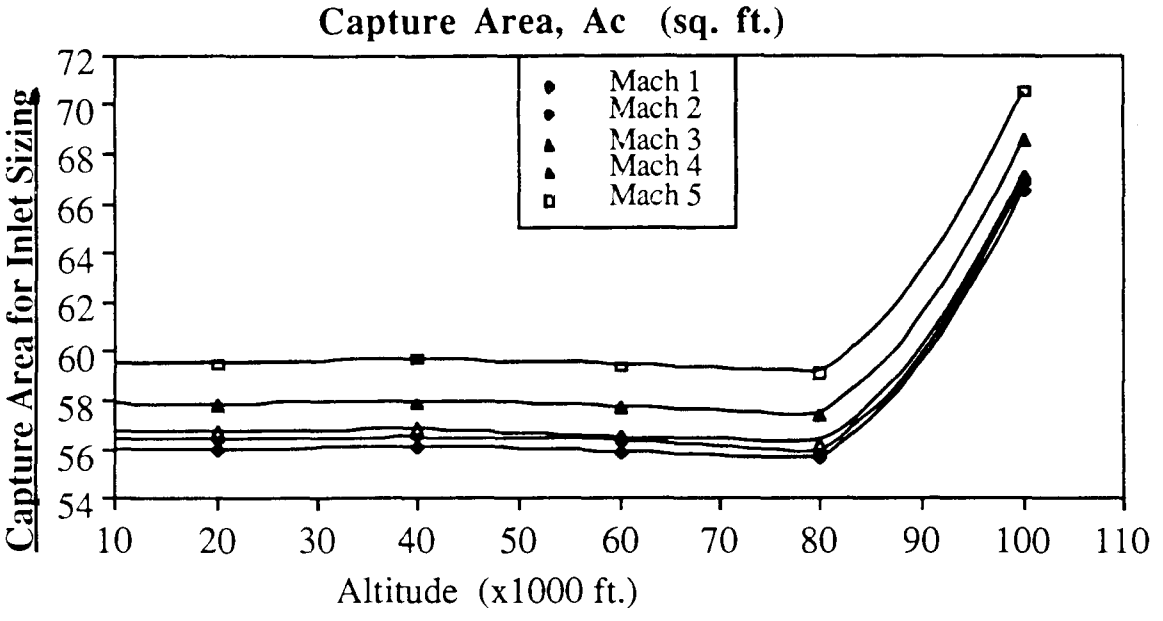

FIGURE 8-27

It was decided that three oblique shocks plus a normal shock would provide the best compromise between the inlet length and weight with respect to the inlet efficiency. This was determined by comparing with five and six shock inlets. These inlets were long and complex which required a weight and drag penalty that well out balanced the benefit of a more efficient inlet.

The inlet configuration was designed as shown in Figure 8-6. The first ramp was fixed at 9 degrees and comes down from the bottom of the fuselage. The second ramp was designed to swing from a line parallel to the first ramp and down to the angle necessary to provide the most efficient turn of the air. This angle would be determined by matching the normal Mach numbers of the first and second shock waves which provides the best total pressure recovery. The third oblique shock comes off the bottom lip of the inlet. This ramp was at a fixed angle of 3 degrees to turn the flow slightly up and in toward the engines. This air then enters the throat and encounters the normal shock wave followed by the subsonic diffuser which would bring the flow to Mach 0.4 at the compressor face.

The inlet total pressure ratio was found using oblique shock wave theory. The normal Mach numbers were found from

$$M_{n_x} = M_x \sin\theta_{x+1}$$

where x is the inlet section number and θ_{x+1} is obtained from M_x and δ_{x+1} using NACA 1135. δ is the ramp angle.

From NACA 1135 the value for $\frac{p_{x+1}}{p_x}$ and $M_{n_{x+1}}$ was found. Then M_{x+1} was found from

$$M_{x+1} = \frac{M_{n_{x+1}}}{\sin(\theta_{x+1} - \delta_{x+1})}$$

Then the total pressure ratio was found by using NACA 1135 and

$$\frac{pt_{x+1}}{pt_x} = \left[\frac{pt_{x+1}}{p_{x+1}}\right]_{M_{x+1}} \left[\frac{p_{x+1}}{p_x}\right]_{M_{n_x}} \left[\frac{p_x}{pt_x}\right]_{M_x}$$

This process was repeated for each shock wave. The inlet design is shown in Figure 8-6. The total pressure recovery is shown in Figure 8-28 for different Mach numbers.

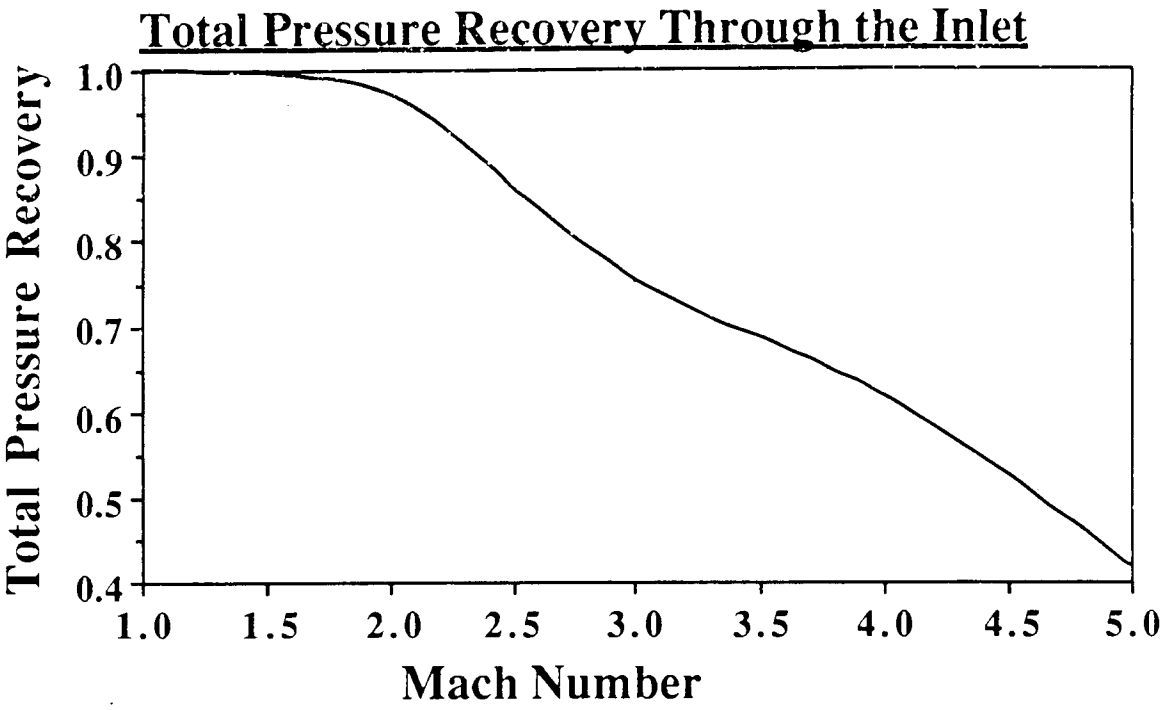

FIGURE 8-28

The weight of the inlet system was then calculated using the method of Reference 9. The inlets for the four engines were divided into two groups with a separator between the two groups only. Thus one inlet services two engines. The parameters used were:

A_i = Capture area per inlet ($ft.^2$)
N_i = Number of inlets
L_d = Subsonic duct length (ft.)
L_r = Ramp length forward of throat, per inlet (ft.)
K_{GEO} = Duct shape factor
p2 = Maximum static pressure at engine compressor face (psia)
K_{TE} = Temperature correction factor
K_M = Duct Material Factor

The weight of the duct provisions was found to be 2347 lbs. from

$$Wt_{DP} = .32(N_i)(L_d)(A_i)^{.65}(p2)^{.6}$$

The weight of the internal duct was found to be 2250 lbs. from

$$Wt_{ID} = 1.735\left[(L_T)(N_i)(A_i)^{.5}(K_{TE})\right]^{.7331}$$

The weight of the variable geometry ramps, actuators, and controls was found to be 6659 lbs. from

$$Wt_{VG} = 4.079\left[(L_T)(N_i)(A_i)^{.5}(K_{TE})\right]^{1.201}$$

This led to a total inlet system weight of 11,256 lbs.

9.0 Structures

9.1. Landing Gear Design

The function of landing gear is to absorb landing and taxiing shocks, provide adequate ground maneuvering, provide sufficient braking, allow for towing, and protect the ground surface. Of these five requirements, protecting the ground surface from damage proved to be the most critical for the Flying Diamond because of the high gross weights involved.

9.1.1 Configuration

There are three basic types of landing gear, but one, the tailwheel type, is not a valid alternative. Of the two remaining possible types of landing gear layouts, tricycle and bicycle, the bicycle type was ruled out because of its poor take-off rotation qualities and high cruise drag associated with high wing incidence angles needed to achieve take-off rotation. Retractable gear, as opposed to fixed gear, was necessary to reduce drag since high speed flight is involved. Another factor which was researched involved determining the types of landing gear existing aircraft employ. Comparable aircraft, such as the Boeing 747, DC-10, Concorde, and the Rockwell B-1, all use retractable, tricycle type gear. With these considerations, the tricycle landing gear configuration was selected. Figure 9-1 is a three view of the tricycle gear.

LANDING GEAR CONFIGURATION

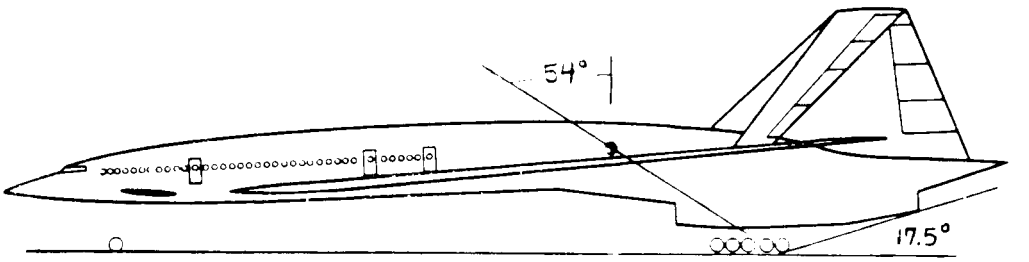

FIGURE 9-1

The landing gear configuration was chosen to be a retractable, tricycle type gear which consists of a single nose gear and four main gears. The nose gear has three tires. Two of the main gear struts have six tires each and two have four tires each. The multiple tires per strut were designed according to limitations on the maximum runway loads. The nose gear retracts forward into an area under the fuselage and the main gear retracts into an area above the engine compartment. This was designed to reduce the retraction complexity. A schematic of the landing gear retraction design is shown in Figure 9-2.

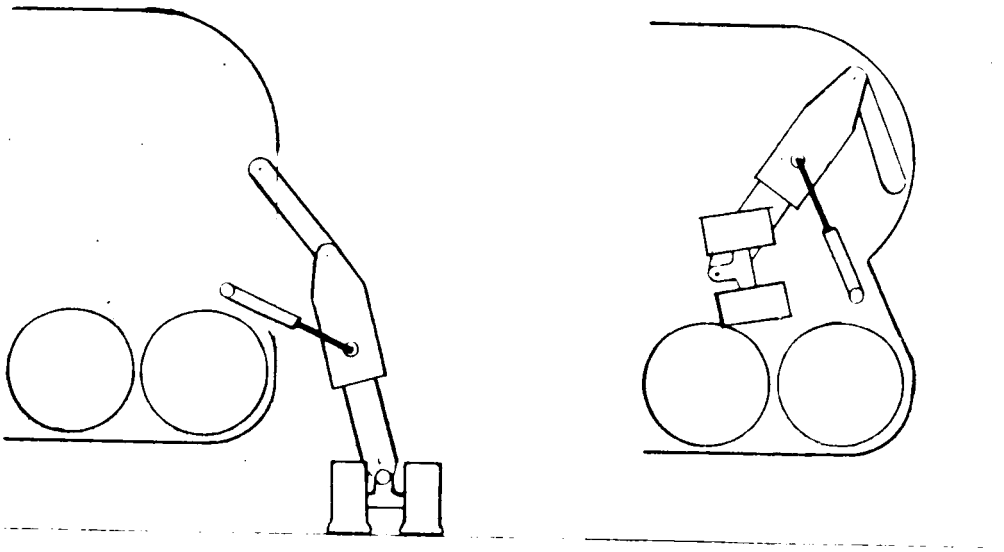

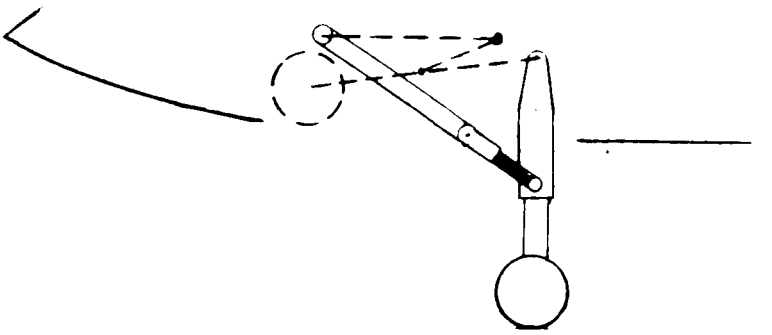

GEAR RETRACTION DESIGN

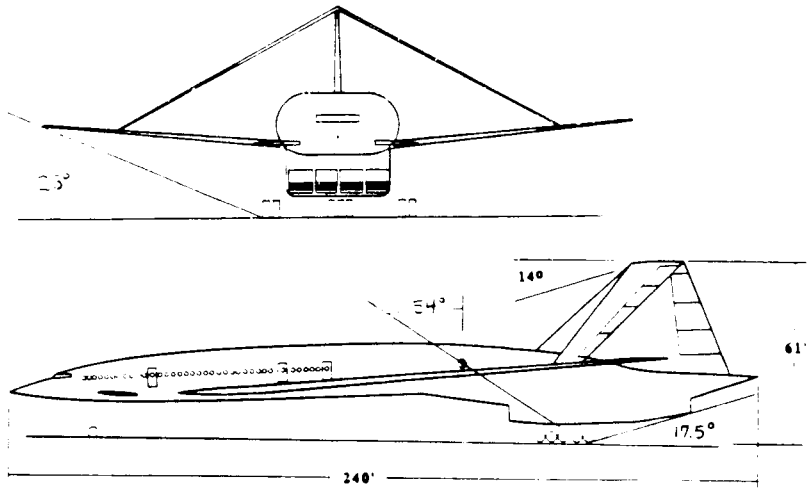

FIGURE 9-2

The landing gear configuration meets all of the important requirements for a preliminary design (References 12 & 17). The placement of the landing gear was chosen with respect to the aircraft's farthest aft center of gravity. The four main gears were placed such that the longitudinal and lateral tip-over requirements stated in Reference 8 were met. Figure 9-1 exemplifies these compliances. This allows a 54 degree angle between the gear and the center of gravity and provides good ground handling with a minimum of 12.7% of the aircraft's weight on the nose gear. A 45 degree lateral tip-over criterion angle is lower than the minimum requirement of 55 degrees. The longitudinal and lateral ground clearance requirements are also met with this configuration. There is a 17.5 degree rotation angle and a 23 degree lateral angle, which exceed the minimums of 15 and 5 degrees respectively. When some or all of the tires are deflated and the shocks are fully compressed, no part of the fuselage, engines, or wing will touch the ground.

9.1.2 Landing Gear Loads

The landing gear loads were determined with the methods in Reference 17. The maximum ramp weight was used for the landing gear load analysis. This was multiplied by 1.07, which is required for FAR 25 certification. With a design weight of 900,432 lbs, the landing gear loads were determined as shown in Table 1.

Table 1

Strut Loads

	Pn (lbs)	Pm1(lbs)	Pm2(lbs)
Static	119051	250292	158413
Dynamic	53632	N/A	N/A
Design	178576	375438	237619

Load Definitions

Gross Weight = 900432 lbs.

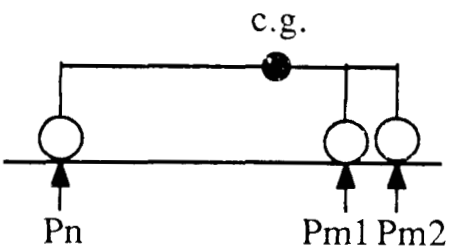

The static load of the nose gear was determined to be greater than the dynamic load and therefore was used for the critical loading. The equivalent single wheel loads (ESWL) and the corresponding load classification numbers (LCN) were determined. The joined wing design was found to be comparable to existing aircraft (Table 2).

Table 2
Tire Pressure and LCN for Various Aircraft

Airplane	Weight, TO	Tire Pressure	LCN
Boeing 707	300,000 lbs	180 psi	80
McDD DC-10	410,000 lbs	175 psi	88
HSCT	900,432 lbs	150 psi	98
Max LCN / Max Tire Pressure		200 psi	100

9.1.3 Tire Selection

The aircraft was assumed to operate only on large, well maintained, concrete runways. With this as a restriction, Reference 17 states that the tire pressure must range from 120-200 psi. With the LCN's shown above, this required a tire pressure of 150 psi and multiple tires per strut. There are various types of tires available, but the one most widely used today is designated Type VII: Extra high pressure and high load capacity. This kind of tire, specifically B. F. Goodrich 50.0-20.0 Type VII, was selected for both the nose and main gear (Table 3).

Table 3
Tire Data

Application: Nose Gear and Main Ge ar			
B. F. Goodrich 50 X 20 Type VII (T SO rated)			
Diameter (max)	50.00 in	Load (max)	41800 lbs
Diameter (min)	49.00 in	Tire Pressure (psi)	150 psi
Width (max)	20.00 in	Speed (max)	200 mph
Width (min)	19.10 in	Aspect Ratio	0.75

9.1.4 Strut Design

The landing gear struts were designed to withstand the maximum loads to which they would be subjected. The maximum stroke was found by comparing the kinetic energy at touchdown of the joined wing with other aircraft and determining an adequate stroke distance. This was designed for a maximum touchdown speed of 12 fps, which is required by FAR 25.473. The strut diameter was estimated with an equation given in Reference 22. For the structural analysis a landing gear load factor of 1.5 was used, which is required by FAR 25. Adequate strength is provided with wrought aluminum 2024-T4 for the struts and linkage and SAE 4340 heat treated steel for the nose gear U-shaped connector. The tire, struts, and dimensions are shown in Figure 9-3.

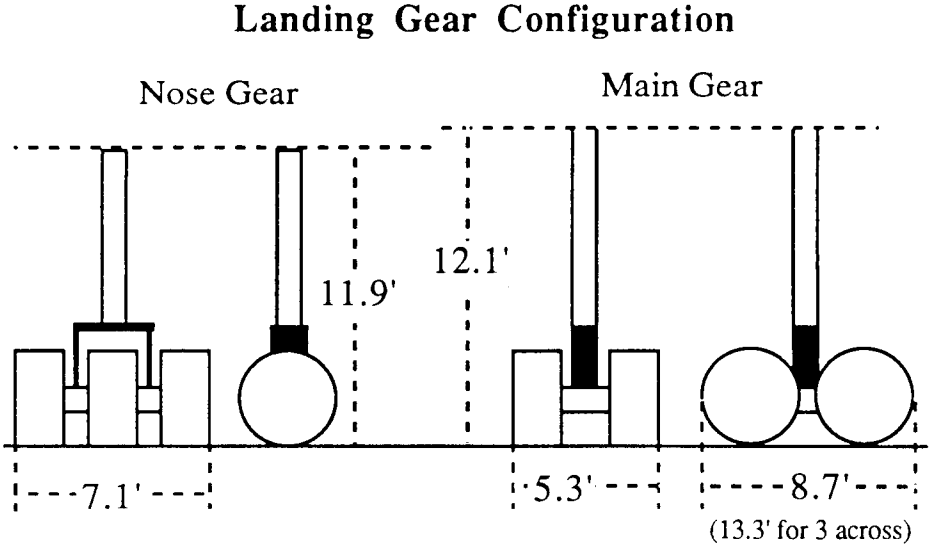

FIGURE 9-3

9.2 Moments of Inertia

The moment of inertias for the Flying Diamond were calculated by dividing each structural element of the airplane into sixty sections. The center of mass for each element was located relative to the center of gravity and the moment of inertias about pitch, yaw and roll axes, and combinations thereof, were calculated. Figure 9-4 shows the variation of moments of inertia for different fuel conditions. Since the fuel is located in the fuselage, pitch and yaw moments of inertias change considerably with time.

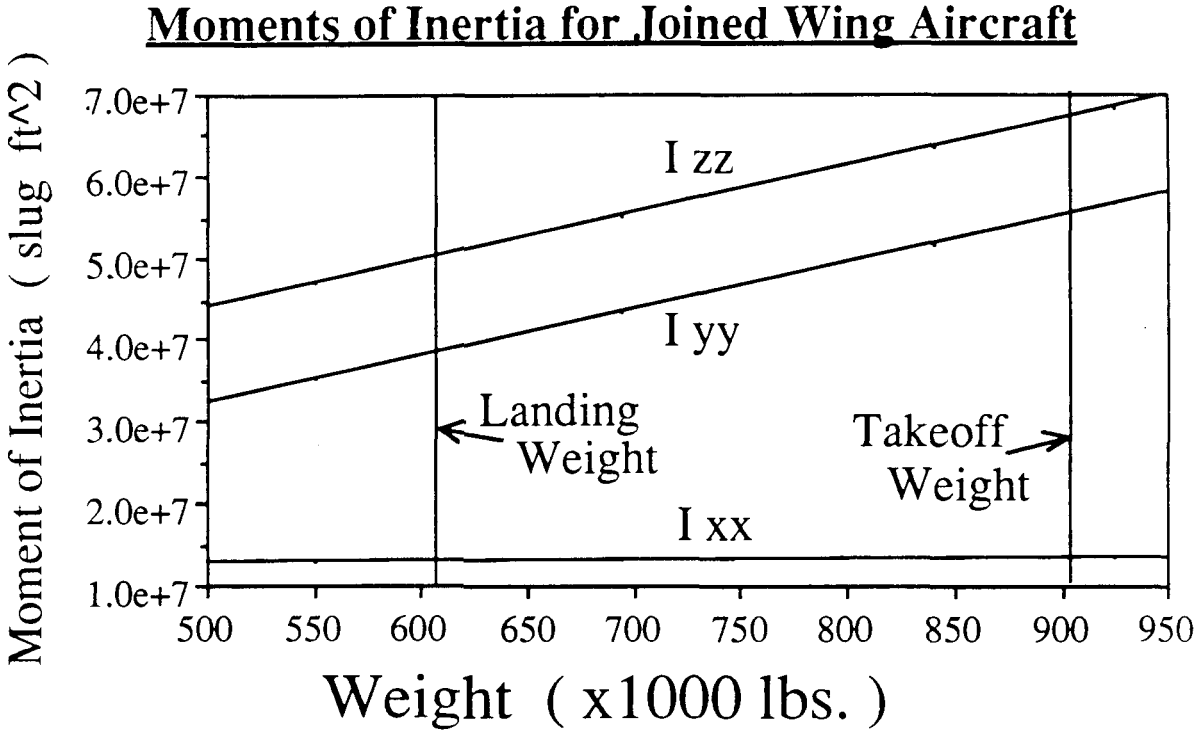

FIGURE 9-4

The Flying Diamond has a special "cantilever" structure that makes the lifting surfaces stronger than conventional airplanes. As a result thinner wings were used and weight savings were obtained. The front wing moment diagram is shown in Figure 9-5.

The discontinuity in the figure above is due to the joint between the front and rear wings and is unique to the Joined-Wing configuration.

In the analysis the internal structure was modeled as a boxed beam (Reference 48) with specially designed internal corners. Since the joined wing has a tilted moment axes the upper left and lower right corners were filled in to have higher resisting strength. The fuselage structure will be a ring type structure.

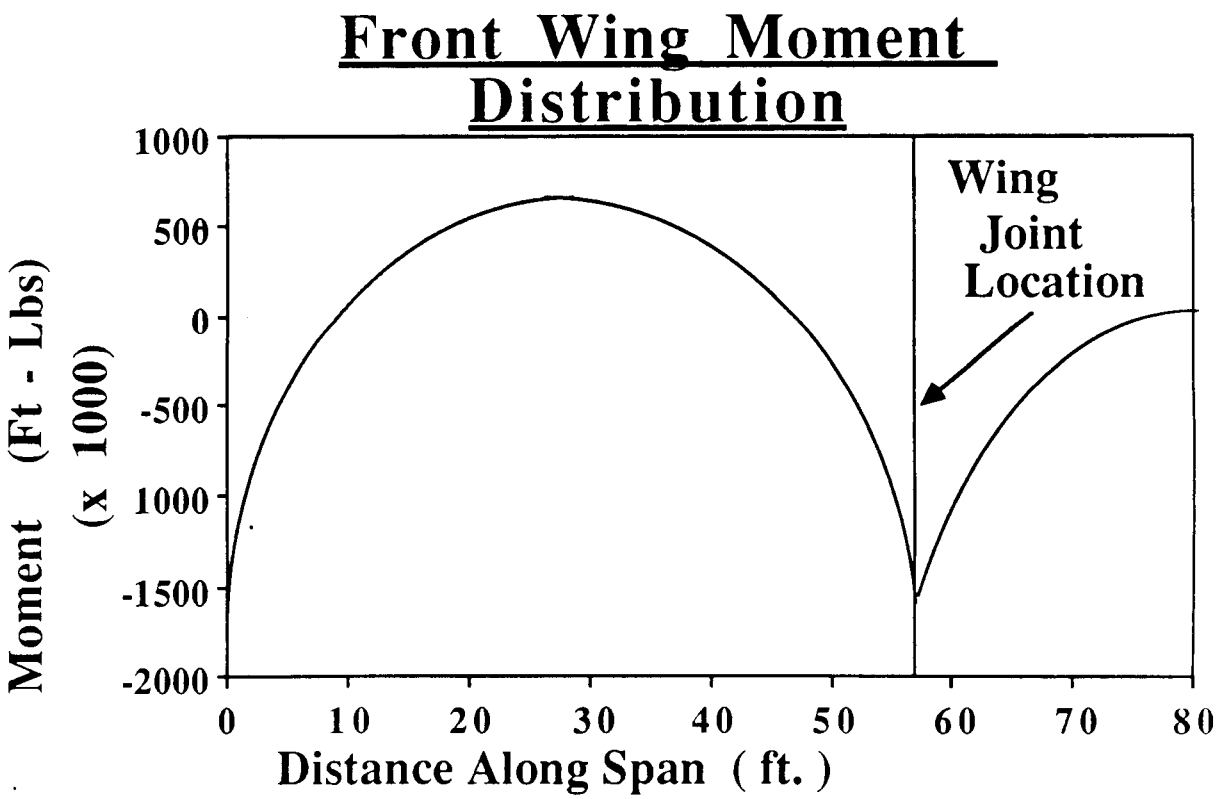

FIGURE 9-5

The V-n diagram in Figure 9-6 was constructed to determine the maximum loading and thus the ultimate loading of the airplane. Since the airplane is heavy the calculated maximum loading was less than the FAR 25 requirement of 2.5. Thus, 2.5 was used as the maximum load factor.

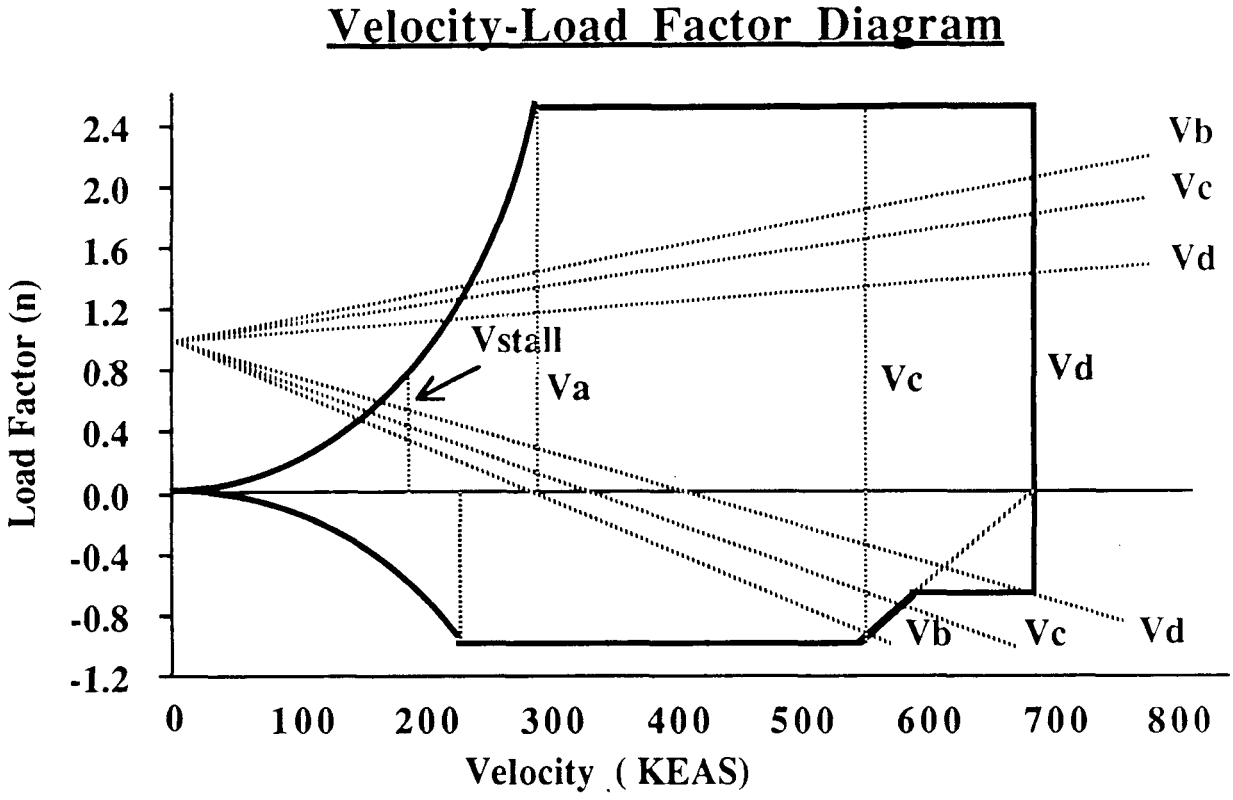

FIGURE 9-6

10.0 Heat Transfer

Due to the Mach range operation of the Flying Diamond the stagnation point heating is a major problem. At cruise Mach number of 4.5, temperatures close to 1800 degrees Rankine were calculated. High temperatures will require active cooling. Thus the fuel itself will be used as an active coolant. Since the fuel is a cryogenic and will be stored at approximately 400 degrees below 0 Fahrenheit, it will serve as an excellent heat sink.

The exhaust gases from the engines will extensively heat the rear part of the airplane. This was one of the major reasons for locating the fuel at the rear of the airplane. As shown on Figure 8-24, the fuel will be used to cool the area.

Another major area that needed cooling was the connection point of the vertical tail and rear wing. The narrow corners at this point will encounter high temperatures. To solve this problem the Flying Diamond will pump methane to this region to extract the heat.

11.0 Noise

11.1 Sonic Boom

Inherent in the mission profile of the High Speed Civil Transport is supersonic flight which requires an appraisal of its sonic boom. Any object passing through the air at a velocity greater than the atmosphere's speed of sound will create a sonic boom. Sonic boom is the name given to the sudden rise and fall of sound pressure resulting from the quick passage of shock waves. Mach cones from the bow and tail of the airplane coalesce to form bow and tail shock waves at supersonic speeds. At the proper atmospheric conditions, the shock waves will extend to the ground. As the airplane passes an observer, the observer will experience the change in pressure across the shock waves in the form of sound. Figure 11-1 shows the bow and tail shock waves, the typical pressure wave generated near the ground and a possible ear response to the pressure signal. Most of the sonic boom's energy is concentrated in the infrasonic (below 16Hz) range. 1 The maximum increase in atmospheric pressure due to sonic boom is termed the overpressure and is measured in units of pounds-force per square foot or in the typical sound unit, the logarithmic decibel. Another quantity used to describe sonic booms is its duration measured in seconds or fractions thereof.

11.1.1 Law

FAR 91.55 states that no civil aircraft which is capable of supersonic flight may operate from a United States airport nor may it operate supersonically in U.S. airspace. Landing waivers have been granted to the Concorde aircraft to operate from a few U.S. airports but it is prohibited supersonic flight over land. Current HSCT studies being performed by Mc Donnell Douglas and Boeing aircraft companies assume subsonic flight overland and little overland travel (Reference 2). The only stipulation to allow supersonic flight in FAR 91.55 is if the pilot is able to determine that the sonic boom generated by his aircraft will not reach the ground. It makes no mention of tolerable overpressure levels. The

Environmental Protection Agency (Reference 3) says there is no public annoyance from 1 daytime (7am to 10pm) ground measured boom below 0.75 psf based on a day-night average of 55 dB. For more than 1 boom per day, the peak level of each boom, recommended by the EPA, should be less than $\frac{0.75}{\sqrt{N}}$ psf or (125 - log(N)) dB where N is the number of booms. It is expected the attractions and wide ranging benefits of the HSCT will persuade the public to change these laws and to instead invoke laws which seek compromise between feasible operation of an HSCT fleet and sonic boom tolerances.

NATURE OF THE PROBLEM

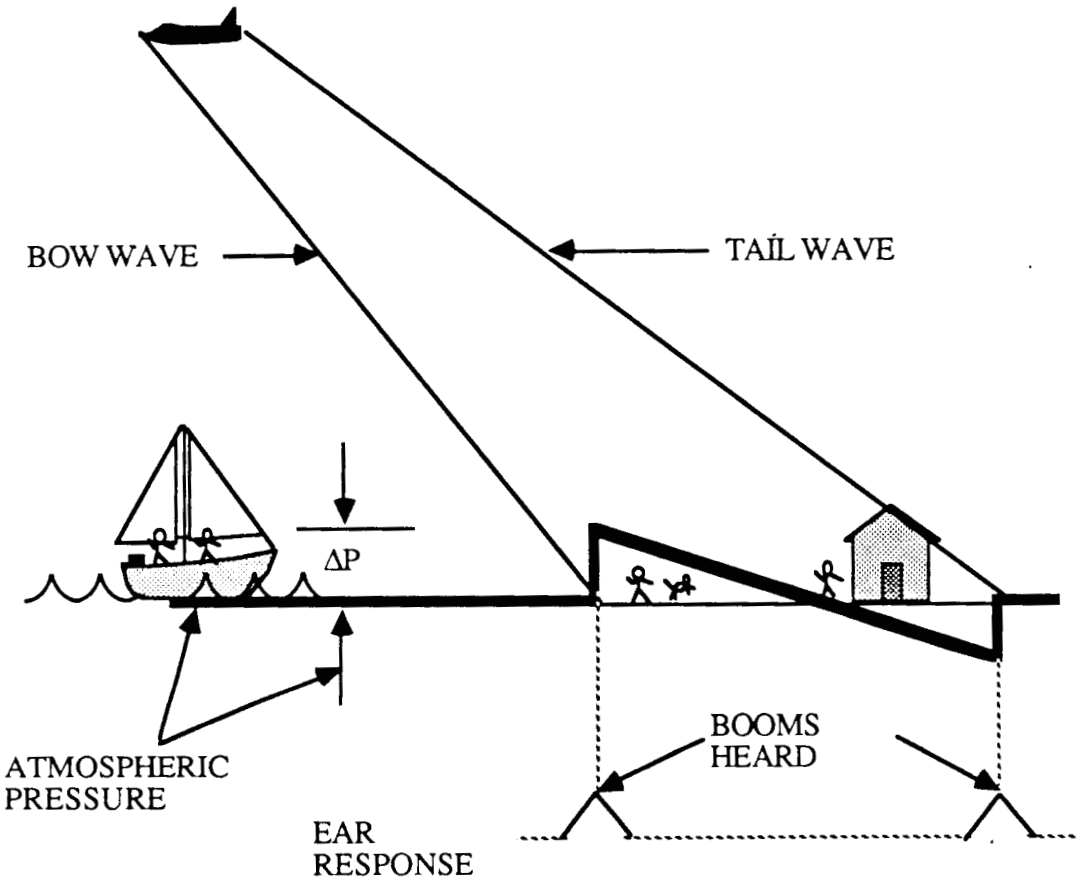

FIGURE 11-1

11.1.2 Prediction Methods

The prediction methods of Carlson (Reference 4), Seabass (Reference 5) and Morris (Reference 6) were used in comparison to estimate the sonic boom signatures produced by

the Flying Diamond. Common to all the methods was input information regarding aircraft shape, speed and altitude.

11.1.2.1 Morris

Morris (Reference 6) 1960 paper gave the overpressure (dp) as either due to volume effects or lifting effects, whichever is greater. The rise in pressure due to volume was

$$dP_V = 0.429\, K_R \sqrt{\frac{P_a}{P_g}}\, K_V\, (M^2-1)^{0.125}\, \sqrt{S_{AM}}\, l_A^{-0.25} h^{-0.75}\, P_g$$

and the rise in pressure due to lift was

$$dP_L = 0.363\, K_R \sqrt{\frac{P_a}{P_g}}\, K_L\, \frac{(M^2-1)^{0.375}}{M}\, \sqrt{W}\, l_W^{-0.25} P_a^{-0.5} h^{-0.75}\, P_g \quad .$$

The use of this method requires and relies heavily upon an estimate of the volume shape factor K_V and the lift shape factor K_L which the author states are generally between 1.5 to 2.0 and 1.4 to 1.63, respectively, for "practical supersonic aircraft shapes" (Reference 6). K_V would be close to 1.5 for bodies whose maximum thickness occur towards the rear and K_L would tend towards 1.63 for shapes similar to delta wings. Morris states that lifting effects will dominate over most of the altitude range of a large bomber or supersonic transport aircraft.

11.1.2.2 Seabass

Seabass (Reference 5) (1972) gave the following equation for the overpressure as

$$P_{so} = \exp\left(\frac{-h}{2H}\right) \frac{P_g\, 4\, l}{3ak\sqrt{2\beta\, h}} \left[\sqrt{1+\frac{9}{8}W'} - 1\right]$$

where

$$W' = ak\beta \exp\left(\frac{h}{H}\right) \sqrt{\frac{h}{l}} \frac{W}{(P_g l^2)} \quad ,$$

$$a = \sqrt{\frac{\pi H}{2h}}\, \mathrm{erf}\left(\sqrt{\frac{h}{2H}}\right) \quad ,$$

and

$$k = \frac{2\Gamma M^2}{\gamma\beta\sqrt{2\beta}} \quad .$$

This equation utilizes altitude, length, and speed as the primary parameters but also the atmospheric scale height which was not well defined. Seabass states

> ....the signature shape that is approached asymptotically below the aircraft in an isothermal atmosphere of scale height H is the signature that occurs at a distance $\pi H/2$ below the aircraft in a homogeneous atmosphere. (Reference 5)

and

> ....the ultimate (pressure signal) advance below the aircraft in a stratified atmosphere is the same as that in a homogeneous atmosphere when z (the distance below the aircraft) = $\pi H/2$. (Reference 5) He also states his methods are usable for "exotic configurations" provided effective lengths and base areas are used.

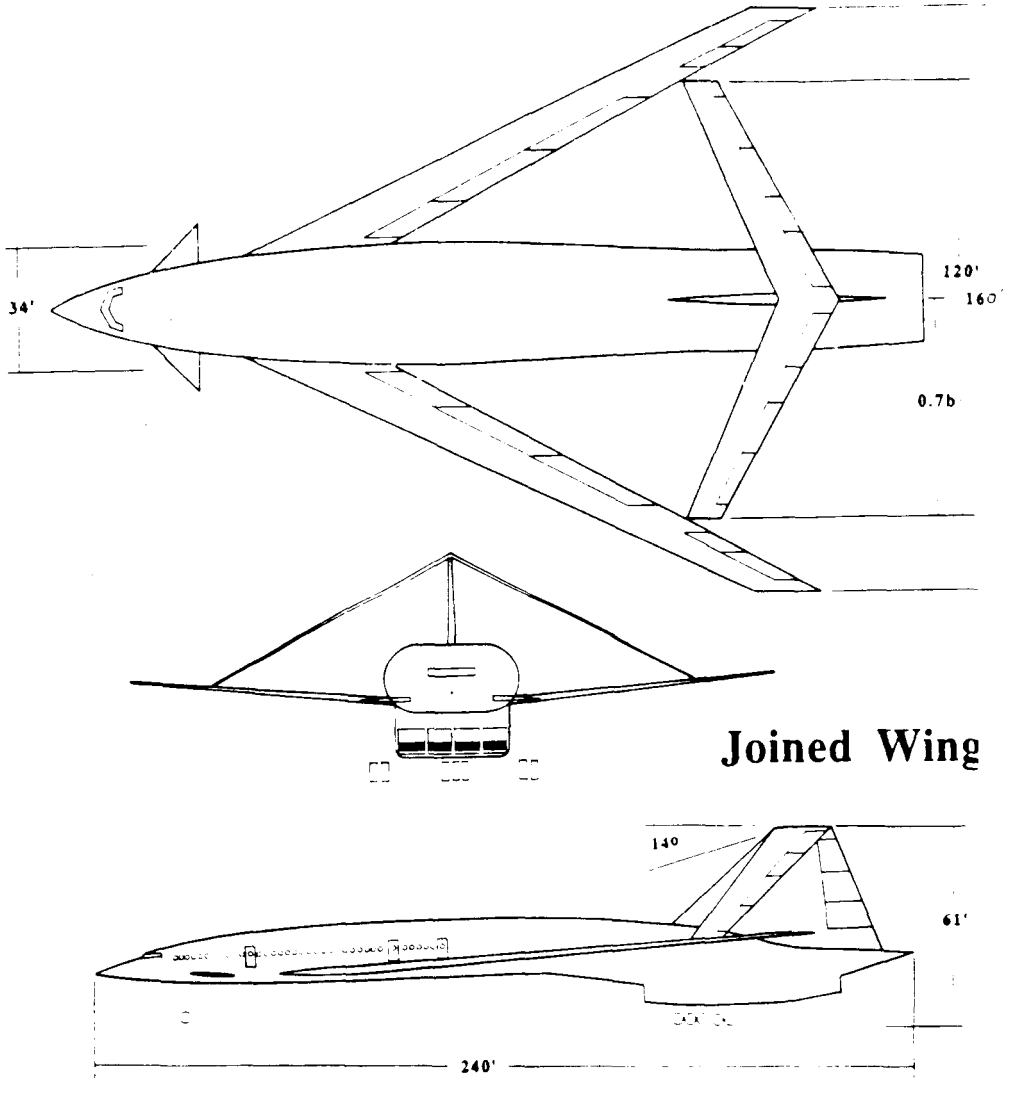

Joined Wing

11.1.2.3 Carlson

Carlson (Reference 4) (1978) published a simplified sonic boom prediction procedure which seems the most thorough of the three methods. Carlson employed the combined effects of lift and volume in his effective area equation:

$$A_e(x) = A(x) + B(x)$$

where B(x) was the equivalent area due to lift and was defined as

$$B(x) = \frac{\sqrt{M^2-1}\, W \cos(\theta) \cos(\gamma)}{1.4\, p_v\, M^2\, S} \qquad b(x)\, dx$$

A(x) was the cross-sectional area distribution normal to the flight path. Since the aircraft was not assumed to be operating at very large angles of attack and rightly so since high angles of attack would create passenger discomfort, areas normal to the aircraft longitudinal axis were acceptable. One then calculates a shape factor assuming a parabolic effective area distribution. The validity of this assumption to calculate the shape factor in this manner was given by Carlson and is accurate to within 5% to 10% of the values for current supersonic aircraft using more rigorous computer methods.

Having found the effective area distribution, one then calculates appropriate altitude factors and finally computes the overpressure and time duration as

$$dp = K_P\, K_R \sqrt{p_v p_g}\, (M^2-1)^{0.125}\, h_e^{-.75}\, l^{.75}\, K_S$$

and

$$dt = K_t \frac{3.42}{a_v} \frac{M}{(M^2-1)^{0.375}}\, h_e^{0.25}\, l^{.75}\, K_S \quad ,$$

respectively. Like Morris, Carlson employed a reflectivity factor, K_R, which one must estimate in order to use the procedure. Morris and Carlson agreed that reflectivity factors between 1.8 for marshy terrain to 2.0 for hard flat surfaces are acceptable. Carlson's model may be used for aircraft altitudes as great as 250,000 ft (76km), ground level altitudes as great as 5200 ft (1600m), aircraft in level flight or in moderate climb or descent flight profiles in the standard atmosphere. The procedure also assumed the generated pressure signal is of the far-field N-type wave like that shown in Figure 11-1. Acceleration or flight-path curvature effects could not be studied due to the limits of the method.

11.1.3 Method Evaluation

Seabass' method gave the lowest overpressures but also required the least information for input. Seabass' equations were only sensitive to length and weight (keeping altitude and Mach constant) and since the four HSCT planforms (Caret, Oblique, Joined and Blended wings) were within 4% of each other's length and at most 16% different in weight, one could expect similar results. The method did not account for aircraft shape or planform which distinguishes the various HSCT configurations to a greater degree than length and weight. Morris' method required more information about the shape of the airplane as given by the boom due to volume factor, boom due to lift factor, wingspan and maximum cross-sectional area inputs. As mentioned above, the volume and lift factors are only estimates. The same bias possessed by the person doing the calculations exists in the results. Carlson's method seemed the most planform sensitive of the three procedures being that cross-sectional area and span distributions as well as length, weight, aircraft planform area, and flight track information were required for input. This last method also output the boom time duration, something of which the other methods made no mention. Input information for the Joined Wing for all three methods can be seen in Tables 11-1 through 11-3-1.

TABLE 11-1

Morris Inputs

K_R	K_V	P_G	K_L	b	L_A	S_{AM}	W
(--)	(--)	(psf)	(--)	(ft)	(ft)	(ft^2)	(lbf)
2	1.5	2116.2	1.4	160	240	530	675000

TABLE 11-2

Seabass Inputs

L	W	P_G
(ft)	(lbf)	(psf)
240	675,000	2116.2

TABLE 11-3

Carlson Inputs

L	S	W	g	q	H_G	K_R
(ft)	(ft^2)	(lbf)	(deg)	(deg)	(ft)	(--)
240	11,300	675,000	5	0	0	2

TABLE 11-3-1

x (% length)	A(x) (ft^2)	b(x) (ft)
0	0	0
5	52	12
10	185	20
15	380	37
20	460	24
25	530	36
30	530	50
35	530	61
40	530	62.5
45	530	67.5
50	530	65
55	500	62.5
60	490	60
65	490	58
70	490	80
75	490	84
80	480	62
85	450	36
90	275	28.5
95	110	26.5
100	0	24

11.1.4 Output

Each of the three different methods were examined. The first method implied overpressures due to lift effects dominate at altitudes above 75,000 ft for all Mach numbers for the Joined wing. Volume effects were prevalent only at higher Mach numbers and lower altitudes. The second method gave results which were desired but not necessarily probable. Sonic boom overpressures for this method were as low as .87 psf for Mach 1.5 at 35,000 ft altitude and only as high as 1.76 psf for Mach 6.5, 20,000 ft -- encouraging for HSCT designers! A goal of 1 psf for high-speed civil transports has been set in hope that U.S. law-making bodies will accept this ceiling for supersonic flight over land. The third prediction procedure yielded results in better agreement with the first's. This agreement gives support for the use of the more recent (third) procedure. Overpressures for the Joined wing were as great as 12.67 psf for Mach 6, 20,000 ft which seems reasonable from such a large heavy aircraft moving at great speeds at low altitude. Boom magnitude decreased as expected at higher altitudes to 1.71 psf, 80,000 ft , Mach 4.5 -- the design point for the Flying Diamond. Boom time durations increased with altitude for constant Mach and increased with Mach for constant altitude. Although one would expect that as he flies higher at the same Mach number the time duration should decrease due to atmospheric attenuation. The trend, however, was just the opposite. As one flies faster at

constant altitude the sonic boom grew stronger and lasted longer. Figure 11-2 shows lines of constant overpressure for varying altitude and Mach number using Carlson's equations. At the Flying Diamond's cruise speed of Mach 4 and altitude of 80,000 feet one may derive from this figure a sonic boom overpressure of 1.85 psf. The time duration of this boom was 0.52 seconds.

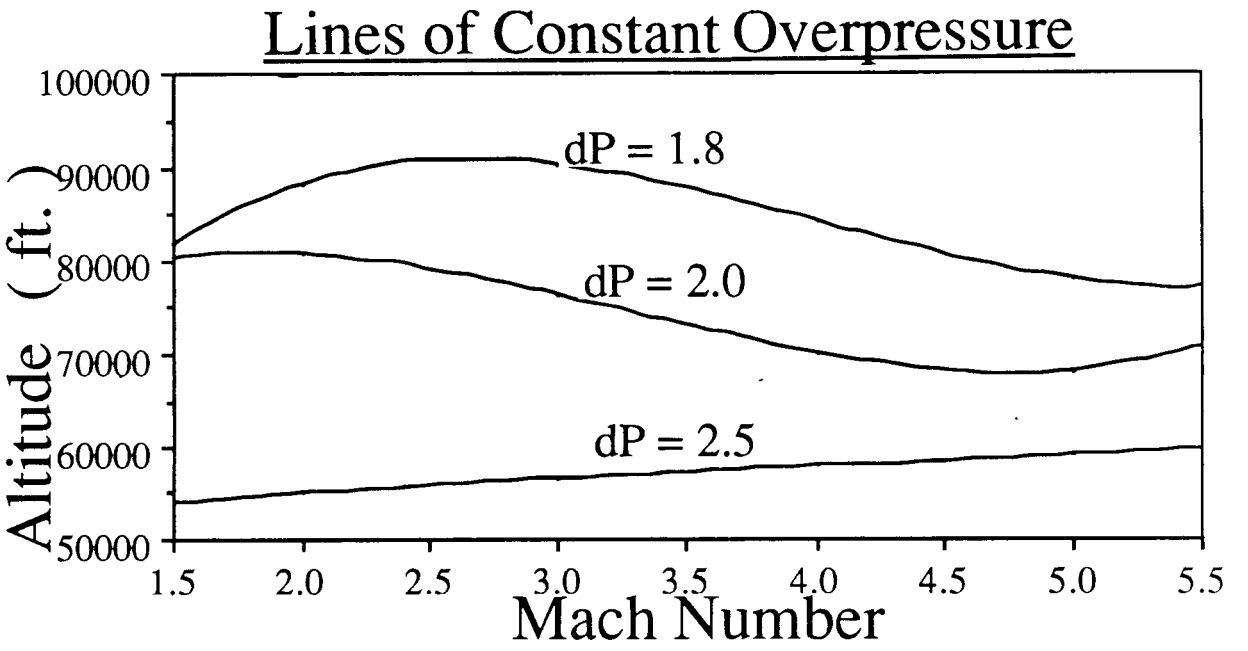

FIGURE 11-2

11.1.5 Trends

McDonnell Douglas HSCT reports a 600,000 lbf aircraft Mach 4 at 80,000 ft was estimated to produce a 1.0 psf overpressure and a Mach 6 design at 95,000 ft would produce 1.6 psf (approximately) (Reference 7). A sonic boom study performed by Driver (Reference 23) for a Mach 2.7, 250 passenger 5500 nm conventional delta-wing Concorde-like design (with fuel only for a 2500 nm range) produced 1.45 psf and a proposed low-boom design (arrow-head shaped) would produce 0.72 psf at cruise conditions. Driver's study indicated the use of planform and cross-sectional area distributions like that of Carlson.

Current supersonic aircraft have been measured to produce overpressures as much as 98 dB (3.1 psf) (Reference 4) whereas the point at which humans experience pain to their unaided ear is about 134 dB (210 psf) (Reference 7). One should keep in mind that sonic

booms are generally within 100 to 500 milliseconds in duration1 and its worse effect on humans is usually to startle them. However, sonic booms will not only touch humans but buildings, the earth and animals as well.

11.1.6 Seismic And Underwater Response

A paper written by Cook and Goforth (Reference 24) studied the seismic and underwater responses to sonic booms. They concluded that an underwater response to a sound wave in air would require the sound wave to fall incident upon the water's surface at an angle less than 14 degrees, the critical angle below which a sound wave is transmitted to the water. For speeds less than 1000 m/s (3281 fps) the assumed N wave propagating from a supersonic aircraft would have an angle of incidence greater than 19 degrees, thus would be totally reflected from the surface. As the HSCT study examines the Mach 3 to Mach 6 flight regime these incident angles could decrease below the critical angle but

> "...because of the large impedance mismatch between air and water, more than 99.8% of the impinging acoustic energy will still be reflected back into the air." (Reference 24)

Furthermore, Cook and Goforth stated that experiments in seawater with electric underwater seismic pulse sources and explosive charges have shown the most sensitive small fish (anchovies, menhaden) as well as oysters, blue crabs and shrimp were not stunned and that one can infer that typical sonic booms will not harm these organisms. The greatest boom they measured in their underground effects study was of 2.5 psf. The ground's attenuation of sound is an exponential decay function and this confined the signal to the top 10 feet of the ground. Since earthquake loci are on the order of 1 km (3281 ft) from the surface, it seems unlikely booms will possess the strength to penetrate such depths. To suppress any concern about the relationships between sonic booms, avalanches and/or landslides,

> "...sonic-boom vibrations may rank beside those of nearby railroads and earthquakes, as a possible triggering agency for avalanches." (Reference 24)

And it was said that sonic booms seldom contribute more than a few percent of the stress required to start a landslide or avalanche. Cook and Goforth (Reference 24) also propose that some sort of warning signal (such as a church bell) be sounded in a community about to experience a sonic boom since there is a noise occurring up to seven seconds before the actual boom. This would greatly reduce the annoyance of startle.

11.1.7 Animal Response

Wilson's article brought forth the effects of sonic boom to animal populations. In several tests conducted by the Air Force on domesticated farm animals ranging from large mammals (horses and cattle) to smaller types of livestock (chicken and turkey), the primary

effects were of momentary fright and temporary annoyance. At overpressures as high as 19 psf from 30 sonic booms daily, the reduction in the livestock production was not apparent, aside from some agitation and fleeing for cover by the animals. In one study, horses and grazing cattle were subjected to an overpressure of 144 psf. Their reaction was of scattering some 10 to 30 yards then returning to their grazing. One type of domesticated animal, the mink, was known to be sensitive to adverse noise yet 5 psf exposures only aroused curiosity in the mink. The effect of sonic booms on wild animals is expected to be similar to domesticated creatures (and humans) with the exception of wild avians. A study in 1969 of Dry Tortugas Sooty terns demonstrated a 99% failure rate in egg hatching, but the failure rate was said to be due to the frightening of the parent bird during the incubation period. This data was compiled for low-altitude supersonic flights while subsequent high-altitude tests were said to have no particular effect on the tern colony. The Flying Diamond does not expect to making 30 sonic booms per day for a given area nor can it or will it fly at speeds and altitudes as to produce overpressures on the order of 19 or 144 psf.

11.1.8 Building Response

In a St. Louis study of 2 psf boom overflights, most damage claims were of the glass category. Other studies of residential-type 1 square meter glass panels and of commercial-type panels 8 square meters by 6 mm thick subjected to 20 psf showed no observable damage. 8 psf overflight experiments in Sweden produced movement of an external wall away from an internal wall in a prefabricated house but 8 psf is also of the order of sound pressure level of a door being slammed shut.

11.2 Engine Noise

Sonic boom is only one area of concern for the Flying Diamond regarding noise. Its engine noise will, at or near the ground and airport, be a significant source of controversy if not first examined by its designers. The design of any airplane requires consideration of the production of noise from its engines. Noise, in any context, is characterized by its sound level, frequency spectrum and its variation over time. *Sound level* refers to the hearer's subjective conception of loudness and is a function of the magnitude of pressure fluctuations about the ambient barometric pressure.9.5 To gain insight on the decibel and frequency scales used in quantifying noise, refer to Figure 11-3 and 11-4. In Figure 11-3 one can compare the dB measurement of an automobile horn to a distant airplane to a soft whisper while Figure 11-4 relates familiar musical instruments to jet roar and fan whine. One can notice that jet roar has the frequency spectrum like that of a bass viol which may

not be aggravating while the fan whine is shrilly like a piccolo or the uppermost octaves of a piano and could be very annoying.

TYPICAL NOISE LEVEL

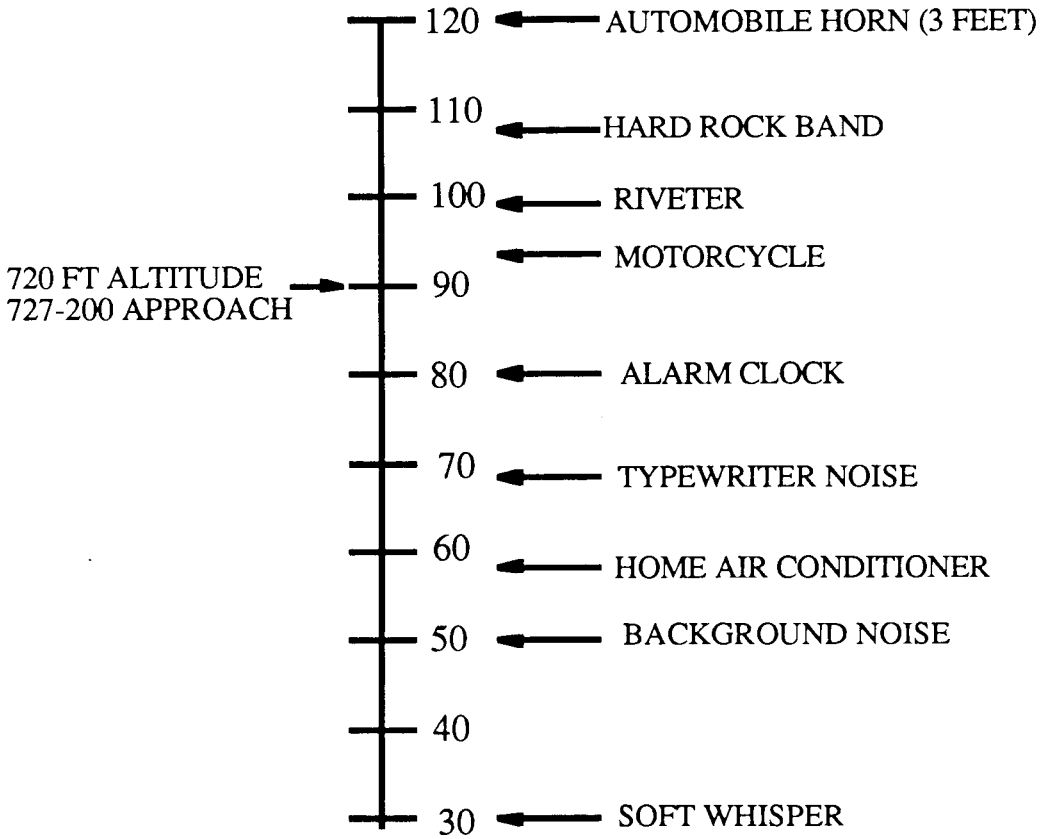

FIGURE 11-3

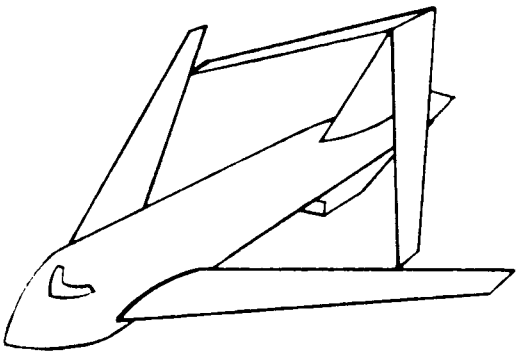

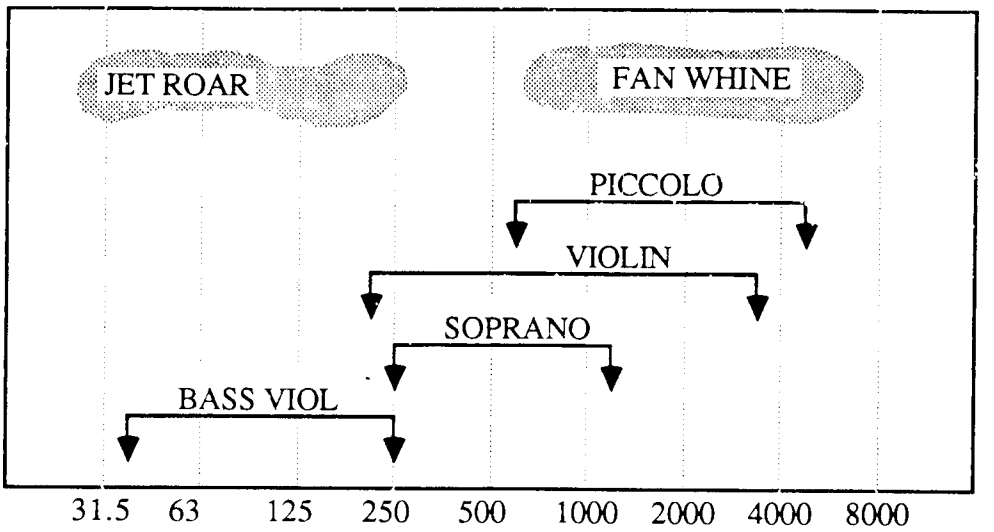

FIGURE 11-4

As the Flying Diamond is employing an air-turboramjet, an unconventional engine, noise generators and suppressor techniques were considered. Figure 11-5 shows in summary the various sources of engine noise. Acoustic liners to act as the inner skin of the engine fairing in parts throughout the entire engine are, in general, effective sound absorbers. In some cases they have reduced noise by 10dB10 but encountered operational problems like freeze-thaw transition and fuel/oil retention. For those and other reasons, alternative reduction methods for unique stages of the engine must be considered. Figure 11-6 shows the same engine schematic as before except this time with the reduction tecniques used by the Flying Diamond. Each section below describes the highlighted portions of Figure XXXXX and some other ideas not shown.

ATR INLET AND ENGINE NOISE SUPRESSORS

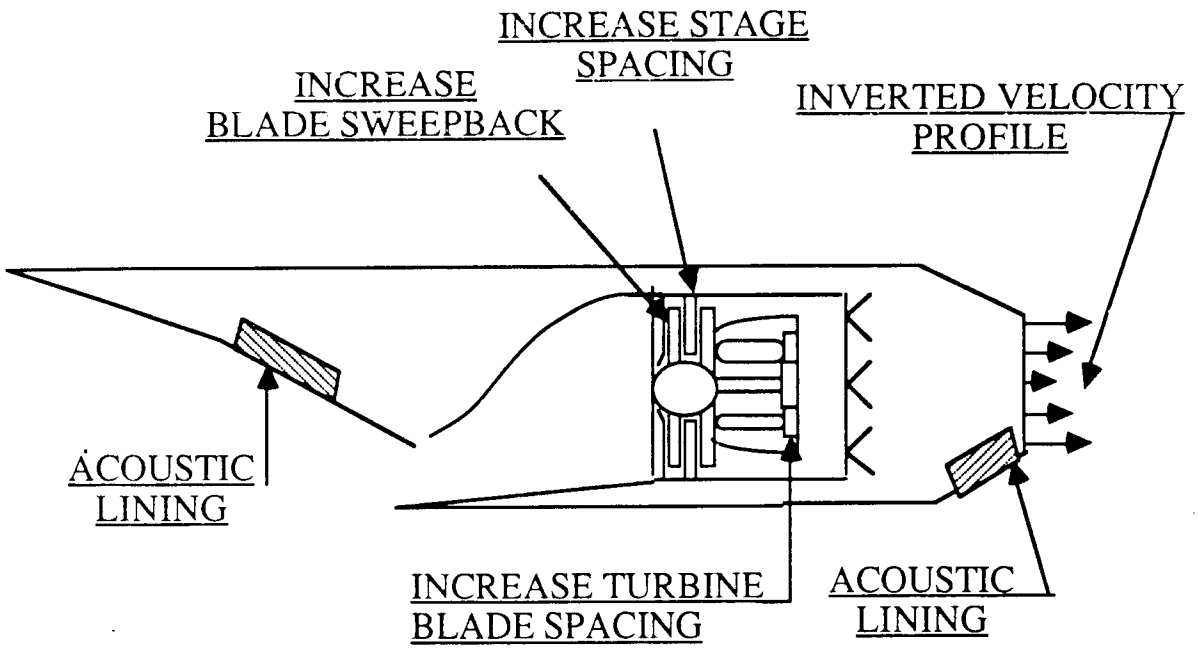

FIGURE 11-6

11.2.1 Inlet

Coming from the inlet system of the engine are internal noise sources of the compressor. Inlet sources are the most prominent during the approach phase. This noise is characterized by two types of noise -- broad-band and discrete tone noise. Broad-band noise is generated by the turbulence and flow velocity as it enters and is generated by the compressor blades. The acoustic energy from the turbulent flow is proportional to its velocity to the 5th power. The incidence angles of the compressor blades also play a key role in noise production. A one degree divergence of blade incidence angle from the optimum angle can increase noise by 3 dB. Discrete tones are associated with the fans of low- or high-bypass ratio turbofans but can also occur from compressor stages. When the supersonic tips of blades have shock waves that are not identical, the familiar buzzsaw noise is produced. Also the cyclic pressure field and wake interactions which exist between rotating and stationary stages are a cause of discrete tones. The correct spacing of the compressor stages and blade sweep-back to defeat the shock problem have been noted as possible solutions. Also proposed is the introduction of an hemispherical honey-comb skin inflow control device to mount in front of the inlet during the landing and approach phases. This device was tested on conventional turbofan engines (Reference 28). A couple of the

FAA NOISE - MEASURING POINTS

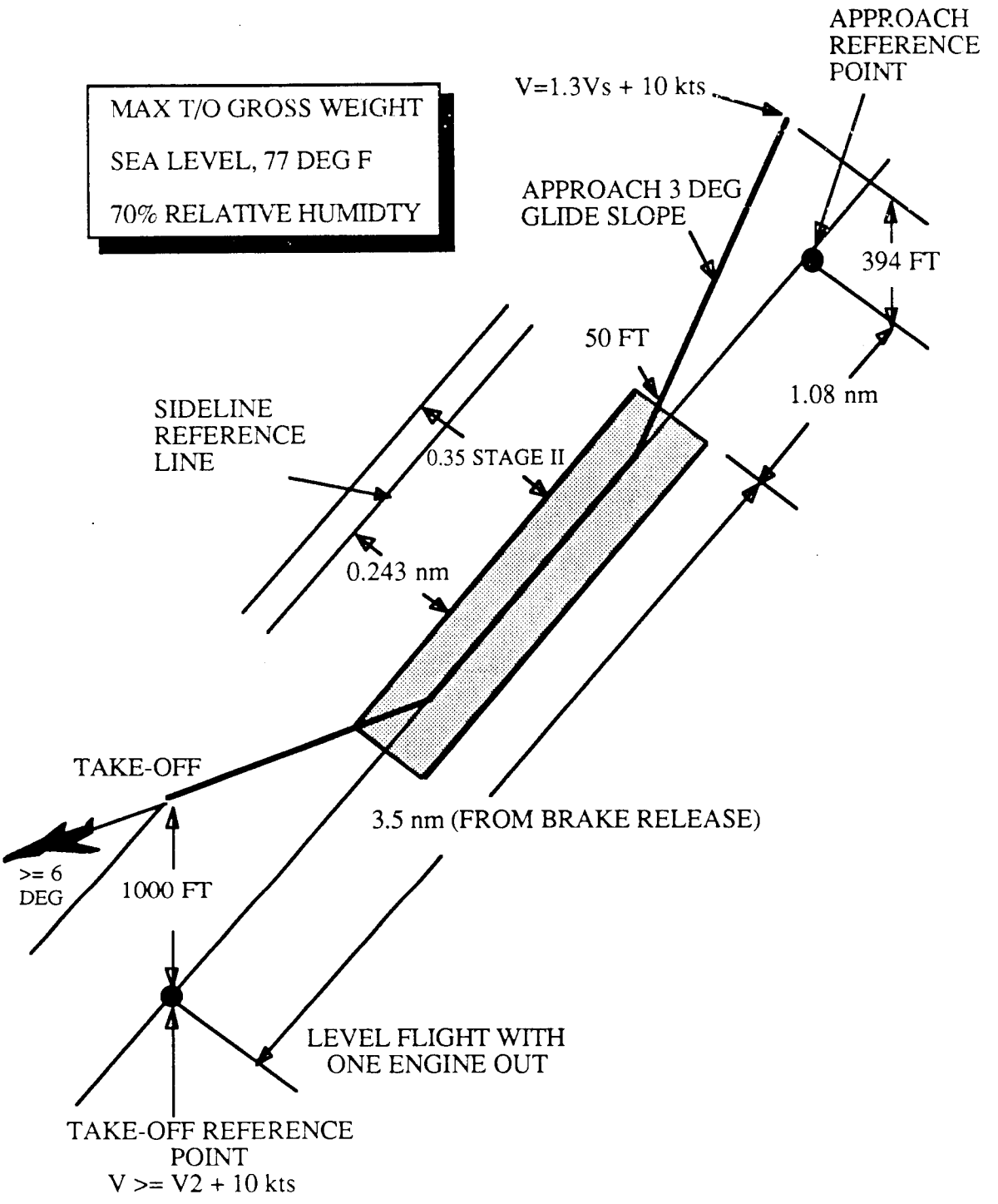

FIGURE 11-7

In the past, the weight, cost and drag penalties of ejectors have eliminated them from widespread usage, but the takeoff thrust required and the associated airport noise will probably take priority. The reader is again referred to Figure 11-6 which shows Flying Diamond noise reduction techniques.

11.2.5 Noise Regulations

FAR 36, Appendix C, Section 36.5 gives the maximum noise levels for various types of aircraft for takeoff, approach, sideline and landing conditions. The measurement stations are given as:

Takeoff:
21325 ft from the start of the takeoff roll on the extended centerline of the runway.
Approach:
At a point 6562 feet from the threshold on the extended centerline of the runway.
Sideline:
On a line parallel to and 1476 feet from the extended centerline where the noise level after lift off is greatest or 0.35 nm for three or more turbojet engines with Stage 2 levels.
Landing:
1.08 nm from point where the aircraft could clear a 50 ft obstacle on the extended centerline of the runway.

These measurement points can be visualized with the help of Figure 11-7. The "Stage" level is a function of the takeoff weight as seen in Figures 11-8 though 11-10. The maximum takeoff weight of the Joined wing coincides with the 108 EPNdB FAR requirement. EPNdB is an acronym for Equivalent Perceived Noise level which takes into account the sensitivity of the human ear to frequency and tone annoyance, together with the duration of exposure to the noise (Reference 1) Figure 11-5 demonstrates the ability of current technologies to reduce sideline noise to meet FAR36 requirements.

key factors in helping reduce the internal noise of a 2-stage turbofan by 20 dB in addition to the ideas presented above was the elimination of inlet guide vanes, divided or non-circular intakes and introduction of acoustic insulation (Reference 26).

11.2.2 Combustor

Noise emanating from the combustor region has been difficult to isolate and little is known about it. One item which is known is that combustors generate low frequency noise and are less annoying than the high frequency buzzsaw whine of the compressor and/or fan.

11.2.3 Turbine

Broad-band and discrete tones are also present in this stage of the engine. To combat these a lesser ratio of stationary to rotating blades than in the fan should be used due to the lower Mach number of the hot flow. High blade loading should be avoided. Large stage spacing is recommended.

11.2.4 Jet

Jet noise (from the nozzle) is probably the most prominent of all engine noise sources especially during the takeoff phase. Key factors here are exhaust flow velocity and temperature profiles. Early civilian turbojet engines such as the ones used on early DC-8's were loud due to the flow of high temperature, high velocity exhaust gases. The popularity of the high-bypass ratio turbo fan grew not only from its lower fuel consumption but also from its quieter exhaust. The idea was (and still is) to surround the hot jet core with cool bypass air. The problem of the high noise radiation from the hot jet core still exists. One way to combat this problem is to use an inverted-velocity-profile (IVP) coannular jet which has the hot flow at high speed but over a greater area surrounding the low temperature, low speed flow. The hot core which was once a concentrated flow is now disbursed to the atmosphere at a higher rate thus quieting the exhaust. Other suppression techniques include ejectors, thermo-acoustic shields, mechanical chute suppressors and advanced operational procedures, the latter to be discussed later. Mechanical suppressors serve to slow the jet flow as close to the nozzle as possible such that the shear between exhaust flow and atmospheric air is minimized. Noise emission from the nozzle is directly related to the thrust output by the engine and thus the velocity. In fact, the noise is a function of the exhaust velocity to the 8th power. The thermo-acoustic shields act as heat and sound energy absorbers and reflectors, respectively. The exhaust temperatures are decreased and sound energy is reflected away from the ground rather than towards it. Ejectors create another path of exit for exhaust thus have mixing characteristics like the IVP coannular jet.

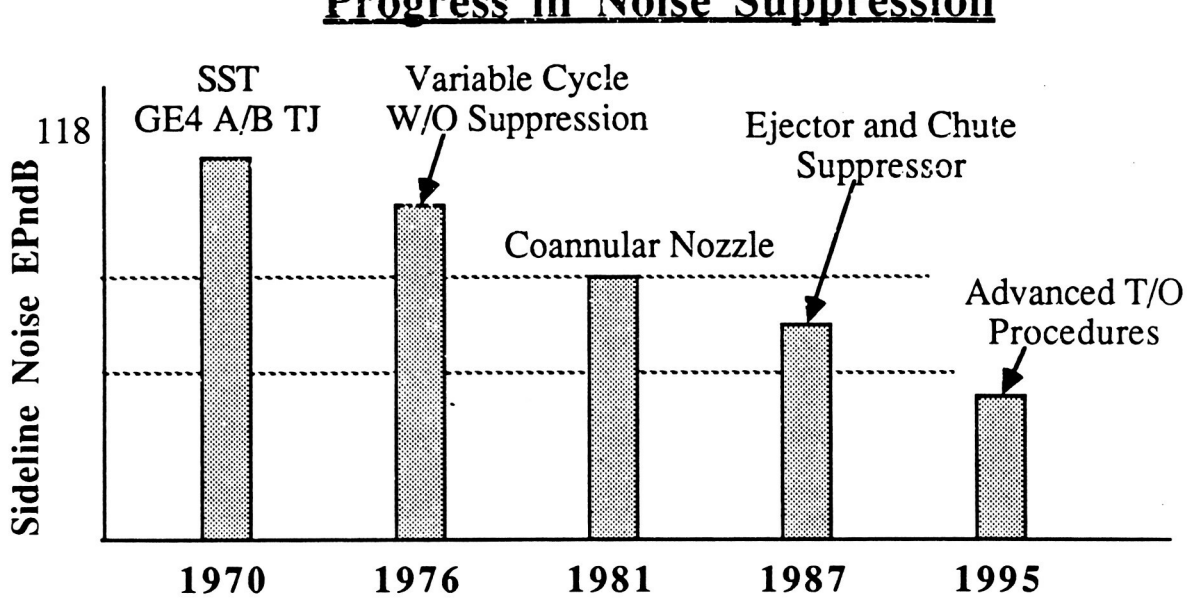

Progress in SST T/O Noise Reduction for 900,000 Pound T/O Gross Weight

FIGURE 11-5

In California, home of major international airports likely to serve the HSCT, the CNEL shall not exceed 65 dBA at airports' property boundaries (Reference 1) CNEL is the acronym for Community Noise Equivalent Level which is a noise rating method using an average level which exceeds a threshold value and is integrated over 24 hours (Reference 32) FAR36 gives exception to Concorde making its guidelines Stage 2 rather than the quieter Stage 3 and states:

> "...noise levels of the airplane are (or should be) reduced to the lowest levels that are economically, reasonable, technologically practicable, and appropriate for the Concorde type design."

This statement translates into a proposition that if supersonic transport (or HSCT) manufacturers/designers reduce noise levels as much as possible then exemptions and/or exceptions to the law might apply.

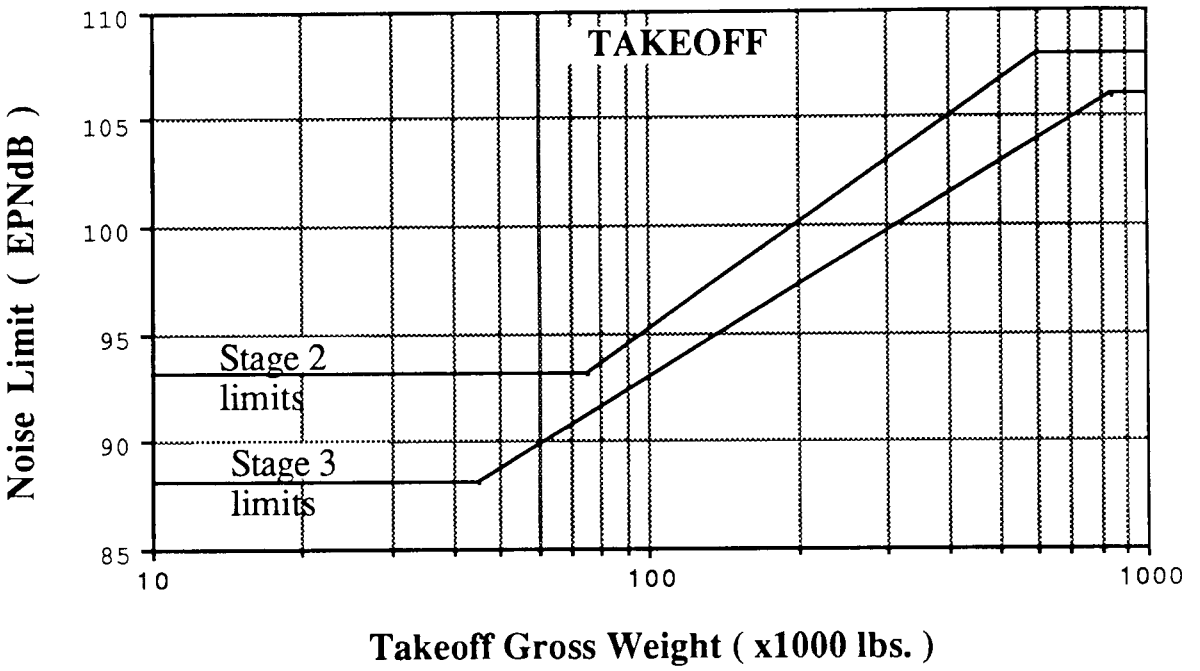

FIGURE 11-8

FAR 36-8 Noise Certification Limits

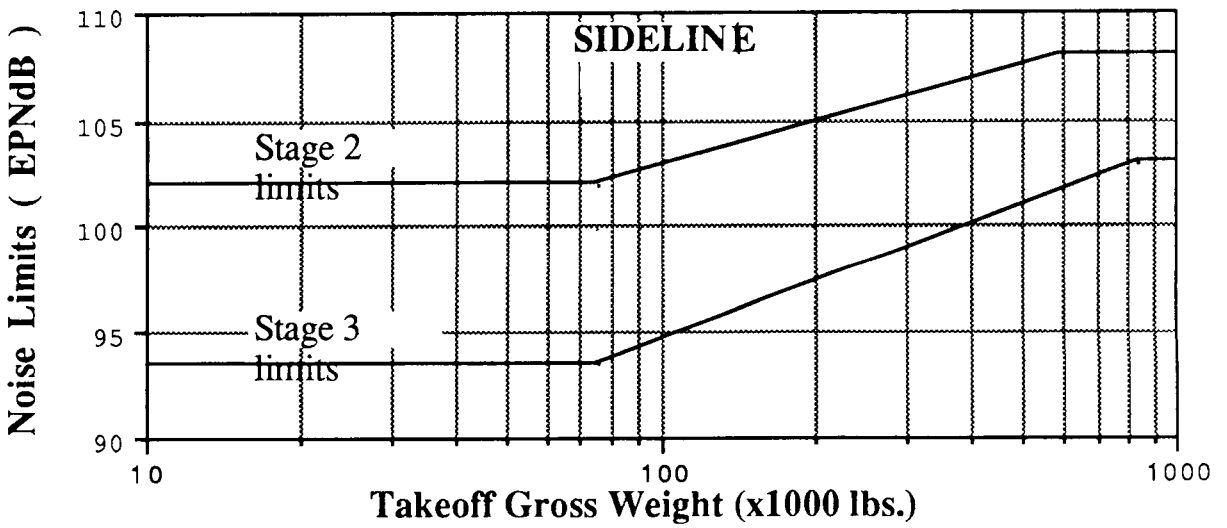

FIGURE 11-9

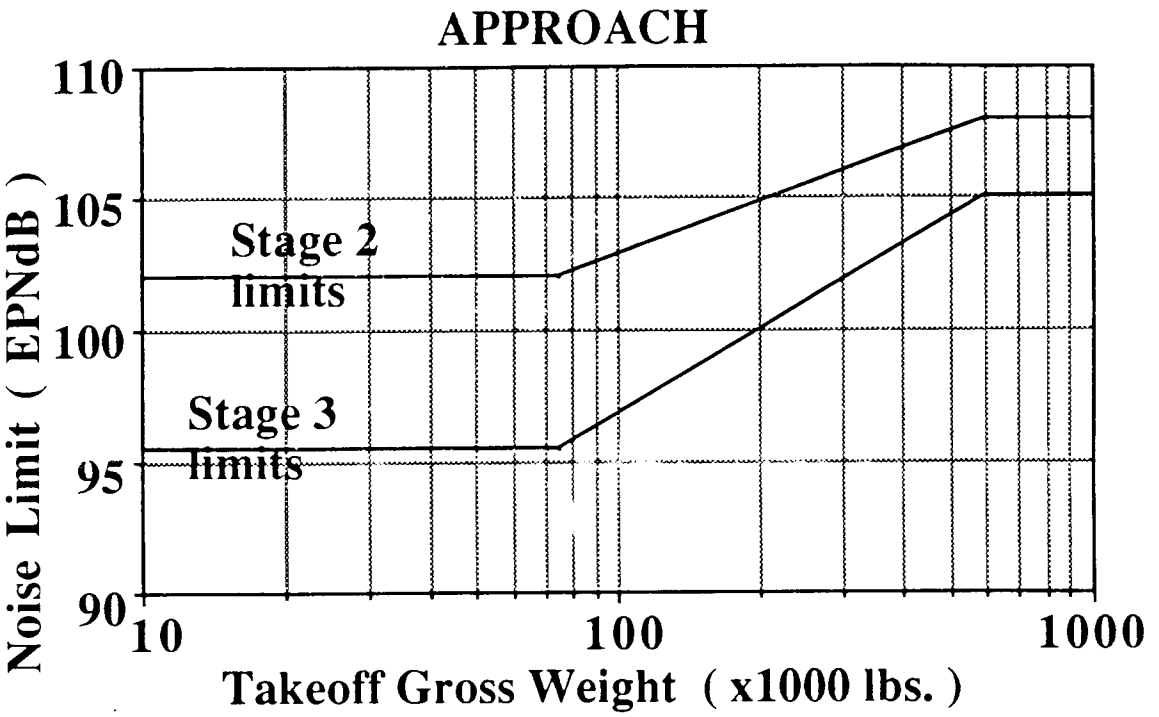

FIGURE 11-10

1..2.7 Trends

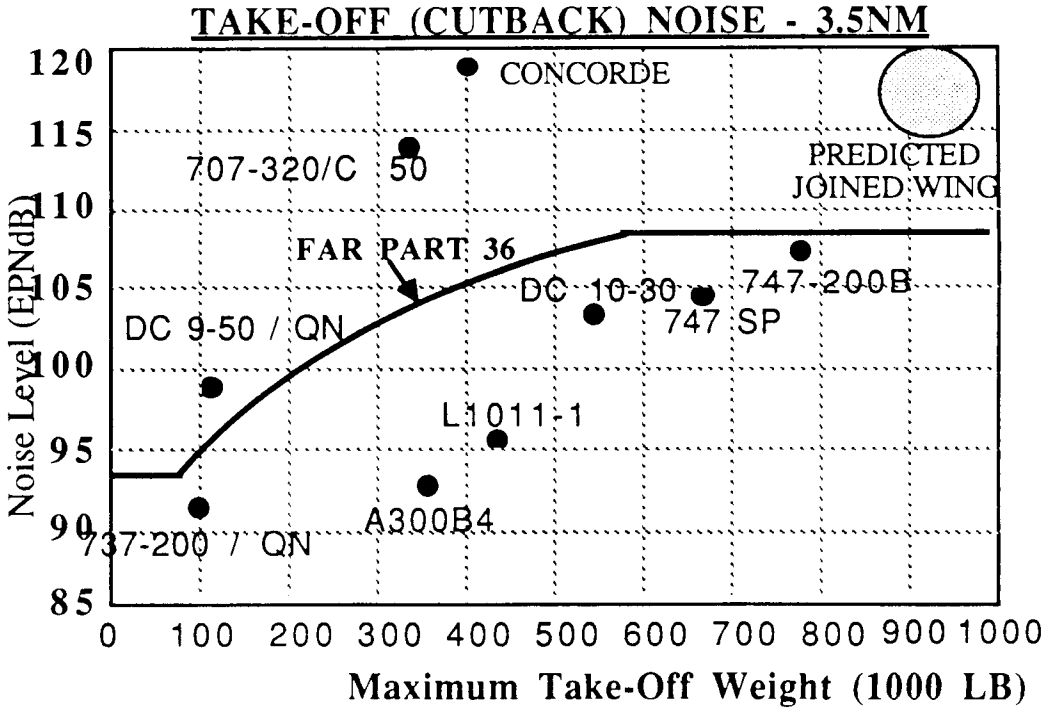

FIGURE 11-11

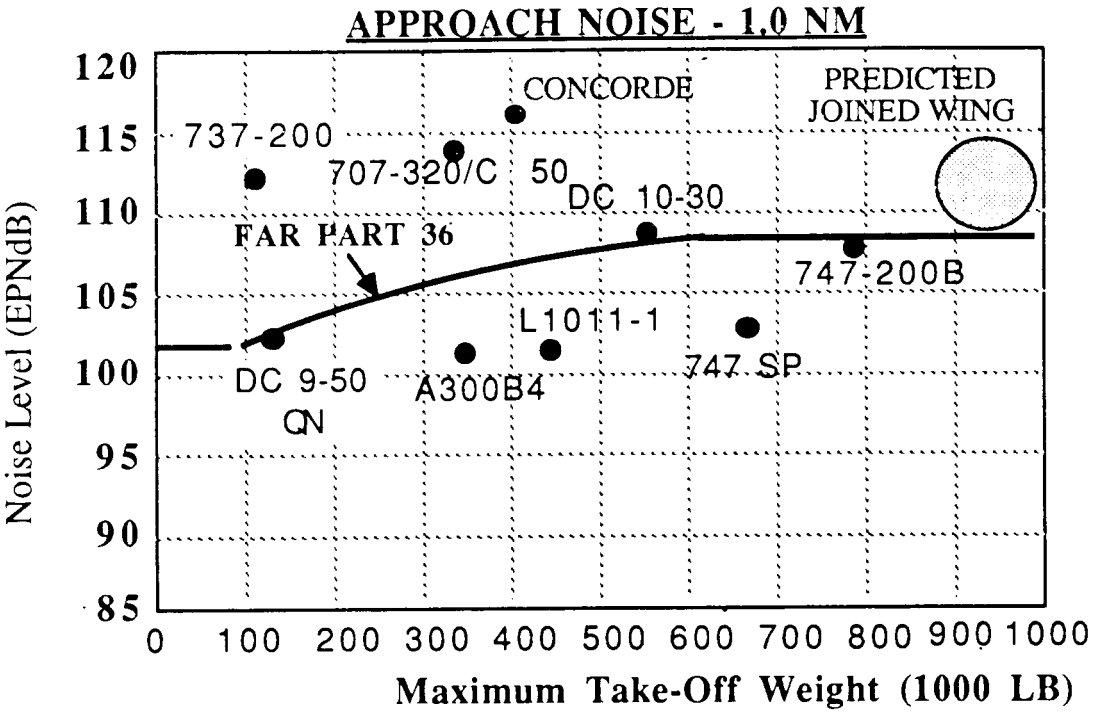

FIGURE 11-12

Figures 11-11 and 11-12 show noise levels for many commercial aircraft in the modes of approach and takeoff to familiarize the reader with the current trends in meeting or exceeding FAR requirements. Also on these figures is a design "point" for the Flying Diamond. The graphic symbol is large for the airplane because of the degree of estimation. The authors of this report believe if Concorde had today's technology in noise supression it would be several decibels quieter, however, the thrust required by the Flying Diamond will push its noise emission to levels equal to or greater than Concorde. Concorde's noise is louder than all other aircraft on the figures, though. Furthermore, reference 31 states:

> "Experience at London, Washington and New York suggests that it (Concorde) is not as annoying to the public as one might think. Certainly complaints levelled specifically against Concorde have dropped dramatically at all three airports once the novelty has worn off. At New York in particular the local inhabitants seemed to have been surprised when the aircraft was eventually allowed in, that Concorde in general caused them less annoyance than other aircraft which had been operating without hindrance."!!

Conflicting with that report is a statement made by an Ontario Airport official who said that after the Concorde landed there once it was then restricted, on the basis of its noise output, from landing at Ontario again (Reference 33).

11.2.8 Airport Noise Reduction Suggestion(s)

A 1982 NASA study (Reference 34) of a Mach 2.62, blended-wing, 290 passenger, 4423 nm range transport concept reduced takeoff noise emissions from 105.7 EPNdB to 103.4 EPNdB using advanced takeoff operations. These tests were performed assuming the use of four double bypass VCE engines with IVP nozzles and 20-chute suppressors. The advanced procedure which had the greatest reduction in sideline noise had the following features: 1) a rotation speed at 200 knots (vs 185 standard), 2) a climb speed of 250 knots (vs 223), 3) stepped flap settings from 20 degrees to 10 degrees at V2 (vs a constant 20 degrees) and 4) autothrottle setting from 100% to 84% thrust at V2 and then to 41% thrust 18,000 ft from brake release. A graphical representation of this procedure can be seen in Figure 11-13. The climbout is essentially constant at an angle of 2 degrees. The significance of this advanced procedure lies in the cutback of thrust to noise-crucial yet safe levels during the climbout. This procedure produced the smallest 108 EPNdB and 104 EPNdB countour areas of 0.82 and 1.25 square nautical miles, respectively. The best landing approach by this report was one of a 6 degree glide slope with net thrust held at approximately 15% until the threshold of the runway versus the standard 3 degrees slope at a 20% power setting. This landing profile is plotted in Figure 11-14. Even though these numbers may not be valid for the Joined wing HSCT there are lessons to be learned. A stepped thrust profile on takeoff and a steep glide slope on approach is highly recommended.

Advanced Takeoff Procedure

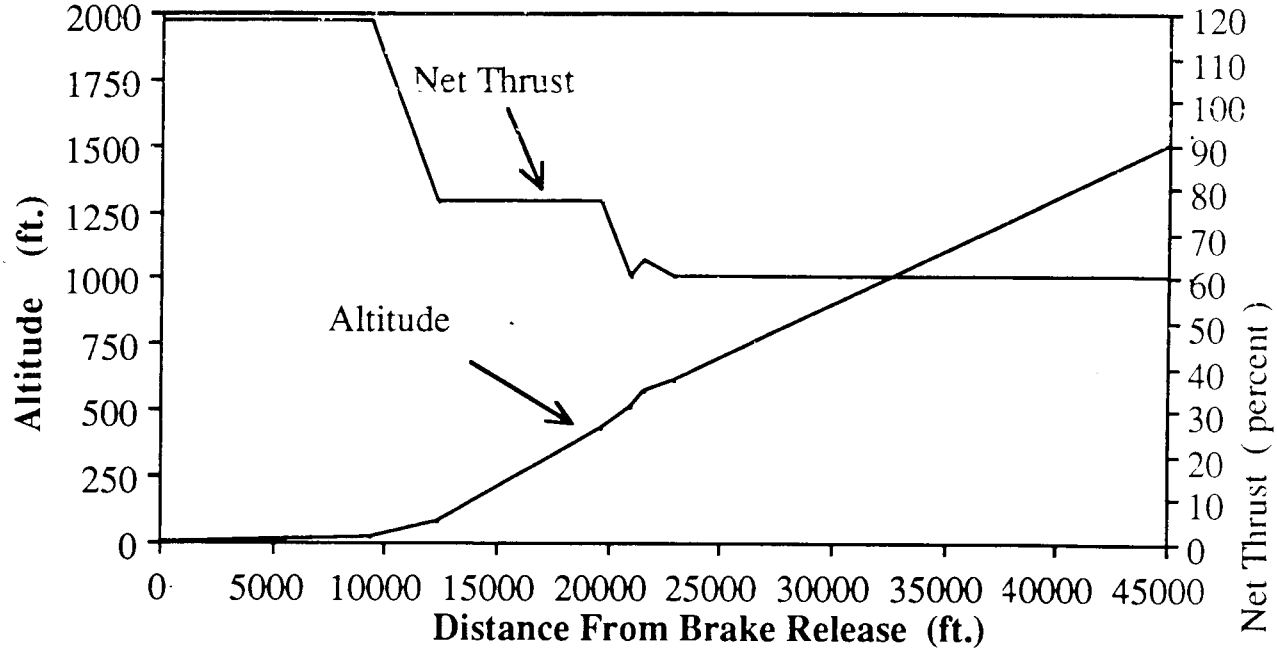

FIGURE 11-13

Landing Glide Angle of 6 degrees, IAS = 158 Knots

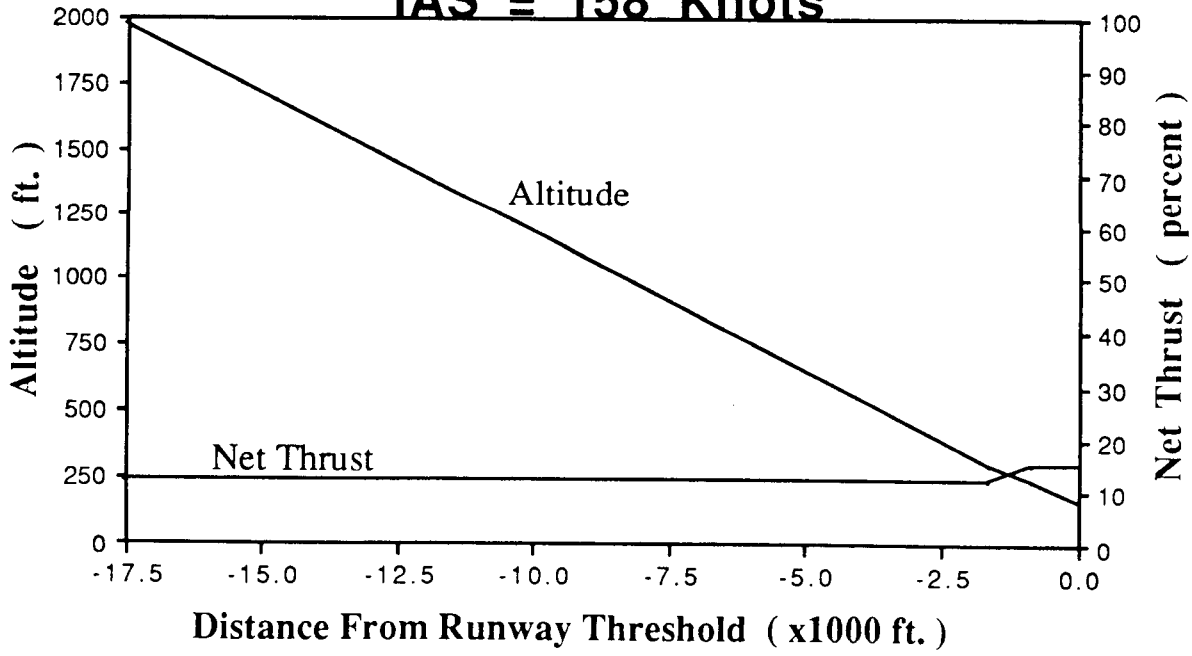

FIGURE 11-14

12.0 POLLUTION

Methane is what is termed an alkaline or paraffin. It constitutes 50 to 90% of natural gas. The reaction of methane with oxygen produces carbon dioxide and water in the balanced equation:

$$CH_4 + \frac{3}{2}O_2 \quad >>> \quad CO_2 + 2H_2O \quad .$$

Complete combustion of methane in air appears as follows:

$$CH_4 + 2O_2 + 2(3.76)N_2 \quad >>> \quad 2(3.76)N_2 + CO_2 + 2H_2O$$

Incomplete combustion of methane yields carbon black which is used in rubber compounding and printing ink. Oxygen deficient burning of methane also produces carbon monoxide and when heated above 9000 C it converts or dissociates to its carbon and hydrogen components (Reference 51).

Complete combustion in air, however, yields the usual carbon monoxide, hydrocarbons, nitric oxides, sulfur oxides (depending on the sulfur content of the fuel) and particulates. The following table shows emissions of the major gases from the burning of methane as a percent of the total gas or particulate matter emitted in 1968. The data was taken from Perkins of reference (Reference 52).

Fuel Combustion Of Natural Gas

Pollutant (--)	Ptationary Pources (% of 1968 totals)	Aircraft (% of 1968 totals)
Particulates	0.7	negligible
CO	negligible	2.4
SO_X	negligible	negligible
NO_X	21.8	negligible
HC	0.9	1.3

The term "stationary sources" denotes electrical power plants. One notices that emissions of nitrogen oxides were the dominating pollutants from combustion of natural gas and was the major concern of the Flying Diamond.

Nitrogen oxides are the most significant contributors to photochemical smog but unburned methane has a low (< 0.2 ppb/min) nitric oxide photooxidation rate which is the rate at

which hydrocarbons cause NO to be oxidized to NO_2. If this rate is used for the basis of smog production, one can say the release of unburned methane will not add to smog.

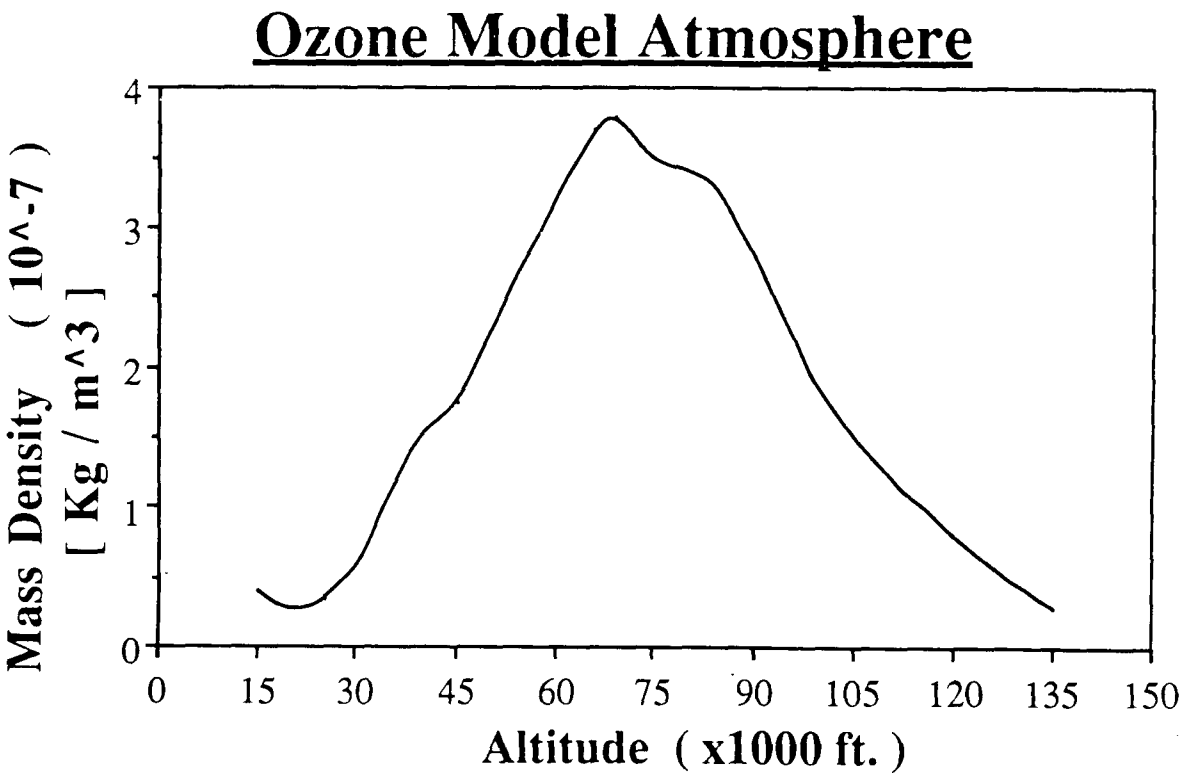

FIGURE 12-1

It has been suggested that a fleet of supersonic transports operating at high altitudes would effect the ozone layer. One article (Reference 38) recommended that such a fleet should operate above 95,000 ft as the 80,000 ft to 95,000 ft layer contains ample free oxygen to provide stability to the 65,000 ft to 80,000 ft layer which varies in quantity of free oxygen atoms -- one of the key factors to the reformation of ozone. Minimal ozone, however, resides in the 80,000 ft to 85,000 ft (Reference 38). This conflicts with another study (Reference 35) which testified to the highest concentrations of ozone being in the 60,000 ft to 80,000 ft range, their approximate ozone distribution being represented in Figure 12-1. If the exhaust emissions of the Joined wing HSCT deplete ozone then it would be advantageous to fly in a region where there exists the least amount of ozone. Some attention might be paid to weather patterns and seasons since reference 39 states that ozone

concentrations are 10% lower than normal before a storm and 20% higher than normal after a storm, and that concentrations are greatest at the higher latitudes in Spring.

There was an article (Reference 42) found which had proof nitric oxides did not affect ozone. A study done in the early '60's of nuclear tests revealed that the large quantity of nitric oxide created from a total of some 340 megatons of nuclear explosions over a four year period showed no evidence of any decrease of any decrease in ozone. Such a large quantity of NO_x would be "perhaps three times that of upper estimates predicted from 500 SSTs flying 7 hours a day for a year." The scientists of this study had 22 stations in the Arctic and 2 stations in the Antarctic recording 12,000 ft altitude nuclear detonation activity during the years of 1961 and 1962. Nuclear explosions were also made in the Pacific at equatorial latitudes where introduction of large concentrations of NO_x with sunlight were supposed to be even more contributory to catalytic ozone reduction. This article is perhaps enforced by the fact residence times of NO and NO_2 in the atmosphere are on the order of 3 to 4 days. Evidence gathered as of the writing of this report is inconclusive as to the altitude of maximum ozone and whether operation of the methane-burning ATR will significantly contribute to the depletion of ozone or production of smog. It is useful, however, to note the current standards and pollution reduction tecniques given below.

Emission standards for SST as of 1979 for new manufactured models (conventional engines) were 3.9, 30.1 and 9.0 pounds hycrocarbon, carbon monoxide and nitric oxides per 1000 pound thrust per cycle, respectively (Reference 32). Beheim (Reference 40) and Petrash (Reference 41) said that hydrocarbons and carbon monoxide were the dominant emissions at idle conditions while oxides of nitrogen and smoke were dominant at takeoff. Petrash (Reference 41) suggests to increase the burning zone, increase the residence time by reducing the flow velocity or by delayed mixing, add more fuel to the fire to raise local temperature and improve fuel atomization to burn lean will reduce idle emission of HC and CO. Running fuel lean, enhancing mixing, increasing flow velocity and again better fuel atomization will reduce the NO_x and smoke emission dominating the cruise or high power regimes. The combustor characteristic were realized in the Vorbix combustor of a JT9-D engine. CO was reduced by about 50%, HC was reduced by a factor of 10% and oxides of Nitrogen by 35%. Catalyzed combustion was also suggested as it aided in nearly pollutant-free combustion.

13.0 Economics

As subsonic travel is loosing its ability to keep up with the pace and needs of today's traveler, the modern and future business person will turn towards ever faster and efficient means of transportation. Concorde sought to fill this need but with current trans-Atlantic fares of $5,500 (Reference 35), and its inability to fly into many U.S. airports because of noise and intolerable sonic boom overland, Concorde has not found its niche. Responding to the demand will be the Joined wing HSCT, however, if the monetary risks of building such an airplane are too high, as was the case with the early 1970's U.S. SST, the program will die. It is the objective of this section to examine the costs and feasibility of the Joined wing.

13.1 Airframe Cost Evaluation

13.1.1 Method

The cost estimation was performed with a paper published by the Rand Corporation (Reference 36) The report was the result of the reduction of cost data on post World War II cargo, tanker, fighter, bomber and trainer aircraft as well as aircraft in the 1970 era -- A-7, F111-A, C141 and OV-10. These aircraft were composed mostly of aluminum alloy, 5,000 to 113,000 lbf in AMPR weight (to be described later) and had maximum speeds of Mach 0.5 to Mach 2.2. The method yields development and production costs of aircraft airframes and subsystems such as engines and avionics, in a long-range planning context and should be used for comparison of relative costs of alternative aircraft.

13.2.2 Limitations/ Inclusions

The computer program supplied by Rand, the Development and Procurement Costs for Aircraft (DAPCA) computer program, only treated costs of the three major flyaway hardware sybsystems of airframes, engines and avionics. It did not include costs of spares, personnel, AGE and any other special equipment required. The development phase was defined as the nonrecurring manufacturing effort undertaken in support of engineering. It included manufacturing labor, material for mock-ups, test parts and static test items. Development costs of, say, M aircraft included development support, flight test operations and cumulative cost of M flight test aircraft plus N operational aircraft. Neither test facilities nor manufacturing facilities were included. Flight test operation costs included costs incurred by the contractor to carry out flight tests, engineering, planning, data

reduction, manufacturing support, instrumentation, spares, fuel, oil, pilots, facilities and insurance. Tooling costs encompassed tool design, planning, fabrication, production of test equipment, maintenance of tooling, production planning and various changes which might take place during the production phase. Material costs included that for raw material, hardware and purchased parts for the major structure. The method reduced material cost per pound of aircraft with quantity produced because of a built-in 88% learning curve. Prototype costs covered limited tooling, few test articles, off-the-shelf engines and avionics but did not furnish production planning. Avionics costs, like materials, had a learning curve associated with them. The variance of engine type was limited to turboprops and varying levels of 1950-1970 state-of-the-art tuboject/fans. One of the paper's disclaimers stated,

> It is emphasized that far greater uncertainty exists when the (cost) equations are applied to aircraft whose technological or performace characteristics are outside the range of the sample.

Clearly the Joined wing HSCT planform lies outside the range of the sample therefore, great uncertainty will plague calculations done for the HSCT.

13.2.3 Input Parameters

The four major parameters required by the method were the desired production quantity, maximum speed of the aircraft, Aeronautical Manufacturers' Planning Report (AMPR) weight and the production rate. AMPR weight was defined as

> the empty weight of the airplane less 1) wheels, brakes, tires and tubes, 2) engines, 3) starter, 4) cooling fluid, 5) the rubber on nylon fuel cells, 6) instruments, 7) batteries and electrical power supply and conversion equipment, 8) electronic equipment, 9) turret mechanism and power operated gun mounts, 10) remote fire mechanism and sighting and scanning equipment, 11) air-conditioning units and fluid, 12) auxilliary power plant unit, and 13) trapped fuel and oil.

Also required as input information were engineering, tooling and manufacturing hourly rates, profit for the project, type of engine(s) used and maximum thrust or shaft horsepower of each engine. The hourly rates should incorporate direct labor, overhead, burden, general and administrative costs and other miscellaneous direct charges. The profit for the project was assumed to be a fee of 10% of the cost to the contractor. The engine type chosen was the most technologically advanced engine able to be handled by the method. To parallel the ongoing Douglas HSCT report (Reference 2) a production quantity of 275 airframes was used. The production rate was chosen to be 5 per month in order to have the project last 4 years. AMPR weight of the Joined wing was 390,000 pounds while the maximum design speed was Mach 4.5 at 80,000 ft altitude (standard day).

Engineering, tooling and manufacturing hourly rates used were 37.75, 27.20 and 21.60, respectively. It was desired to produce 1 prototype and 2 flight-test Flying Diamonds. The cost calculation excluded estimates of avionics but included triple material 1970 material cost as the Joined wing will use 1988 (or better) composites.

13.1.4 Output Parameters

Figures 13-1 through 13-4 show prototype, development, total aircraft and unit cost breakdown. The total prototype cost came to 2.446 billion dollars. All costs quoted in this text are in 1988 dollars since 1988 hourly rates were input and also include the 10% fee. Engine development was the major percentage of the prototype cost as seen in Figure 13-1. This was due to the use of off-the-shelf engines to perform like an ATR. Engineering was the dominant cost of the development phase evidenced by Figure 13-2 and was expected to be dominant since the Flying Diamond will require a much more refined design effort. The total development cost was projected to be 13.987 billion dollars. The cumulative average total cost for 275 production Flying Diamond aircraft was 136.4 million dollars . Figure 13-3 shows manufacturing as the major contributor to this cost with engineering and material costs close behind. The reader is again reminded of the tripled material cost due to the expected use of advanced composites. Material costs then dominate the unit cost breakdown of Figure 13-4 . The cumulative average total unit cost over the 275 aircraft project was 71.151 million dollars. Compared to the recent acquisition of two 747 jumbo jets for 266 million dollars, the estimate for the Flying Diamond seems low but one must keep in mind the scope of the DAPCA program regarding its statistical data base and engine allowances, the exclusion of avionics costs and equal weighting of development support, flight test, engineering/tooling/manufacturing hours, engine development/production factors.

Prototype Cost Breakdown

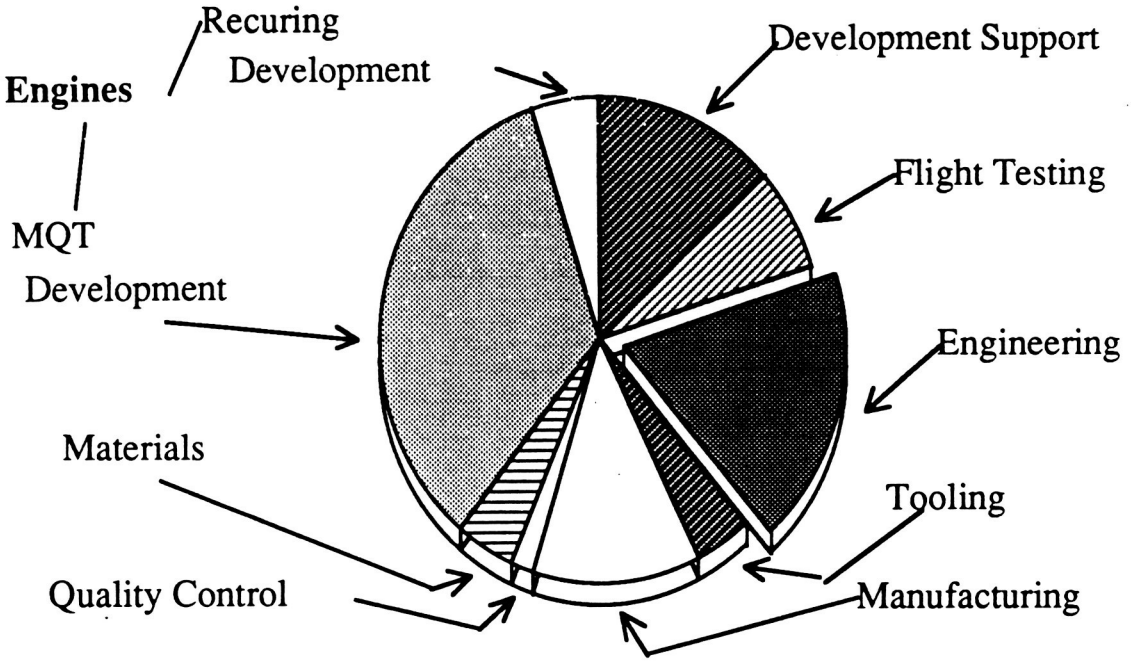

FIGURE 13-1

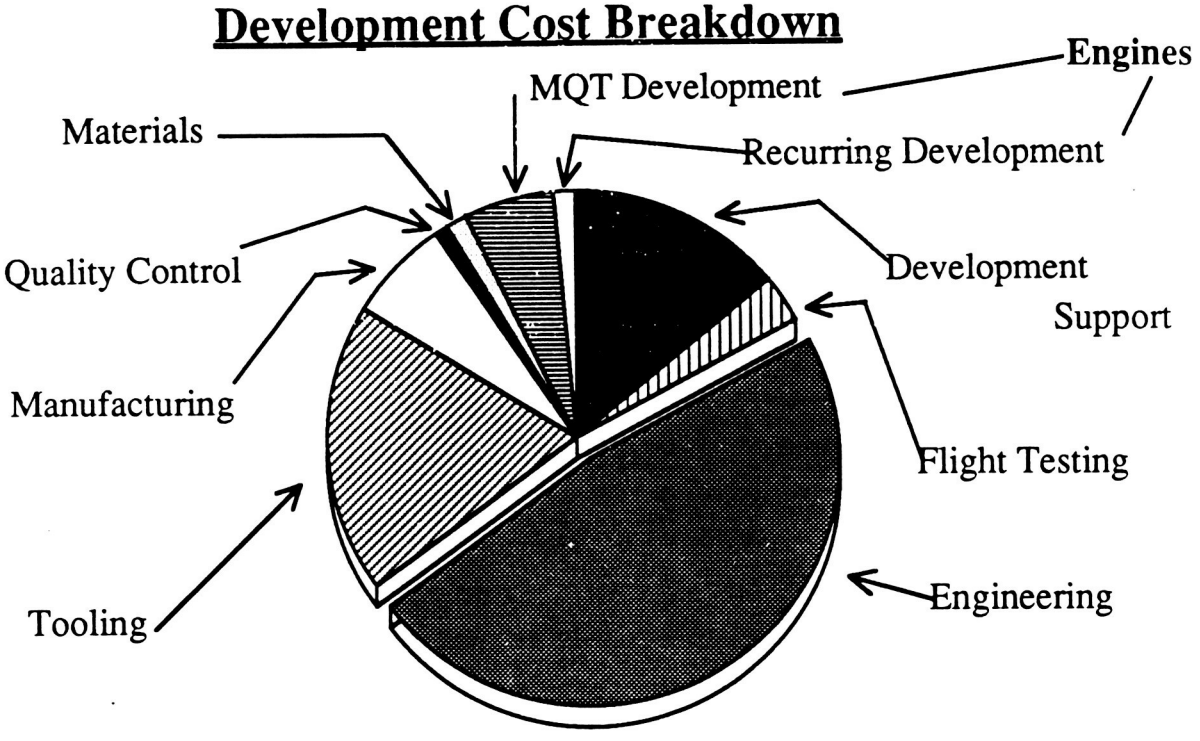

FIGURE 13-2

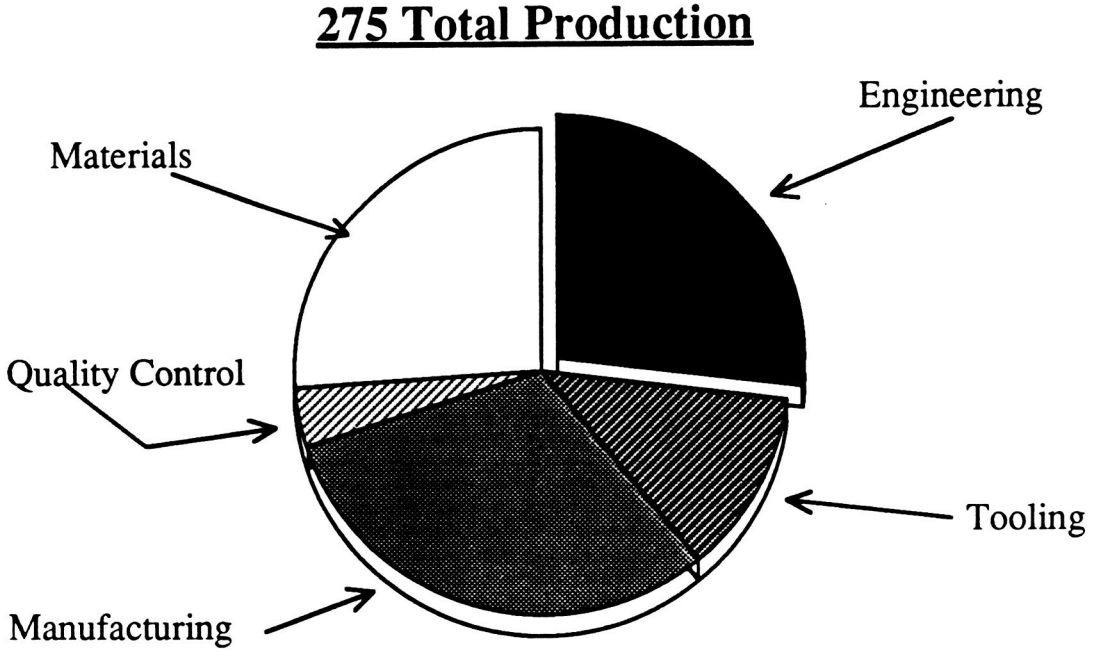

FIGURE 13-3

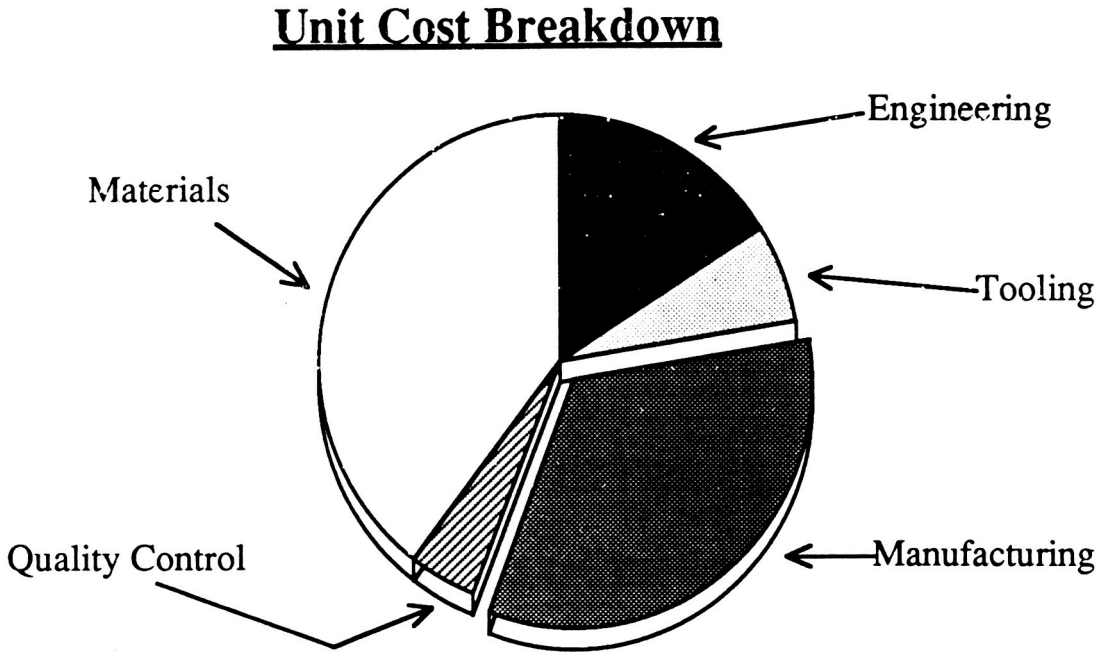

FIGURE 13-4

13.2 Other Economic Considerations

Another study of HSCTs done by Douglas aircraft (Reference 35) examined some of the other economic aspects such as market analysis, utilization, fuel and vehicle worth. Market analysis yielded expectations that by the year 2000, the Pacific Basin will exceed the European Economic Community by 0.8% in economic growth while the North/mid-Pacific and North Atlantic markets will represent two-thirds of the total world international traffic. HSCT will accomodate these regions since routes in these regions have trip distances of 6,000 to 7,500 miles and since Mach 4.5 travel such as that of the Joined wing will cut 7,500 mile trip time from 14.4 hours to 3.7 hours. Mach 4.5 cruise also sees benefits in utilization. The change in annual seat-miles per aircraft with Mach number tends to its minimum value at Mach 4.5 where annual seat-miles per aircraft are at about 1,800. Douglas' report states, "Of all the (cost) elements, fuel represents the most significant cost driver." The acquisition of methane was seen to be projected as equal to that of Jet A fuel, each costing 10 cents per pound, but only methane would be able to deliver the performance necessary at Mach 4.5 cruise. In terms of vehicle worth, or in other words, passenger revenue, direct and indirect operating costs and a 10% return on investment to

the operator, Mach 4.5 LNG-fueled HSCTs produce vehicle worths 200% greater than advanced subsonic transports but also have the greatest sensitivity towards change in fuel price -- "a 1 cent per gallon change in methane...results in a $2.3 million change in vehicle worth." What could save the day for HSCTs would be if turnaround times were 1 hour for such a time would generate $75 million in additional vehicle worth according to the Douglas report.

14.0 Additional Design Features

14.1 Design for Safety

The Joined Wing HSCT was designed with passenger safety as a major requirement. The structural design of a joined wing is a safety feature by itself, having the wing torque box near the front of the plane. However, other safety features have to be designed into the aircraft. To begin, all of the fuel is kept away from the passengers, as shown in the inboard profile of Figure 14-1.

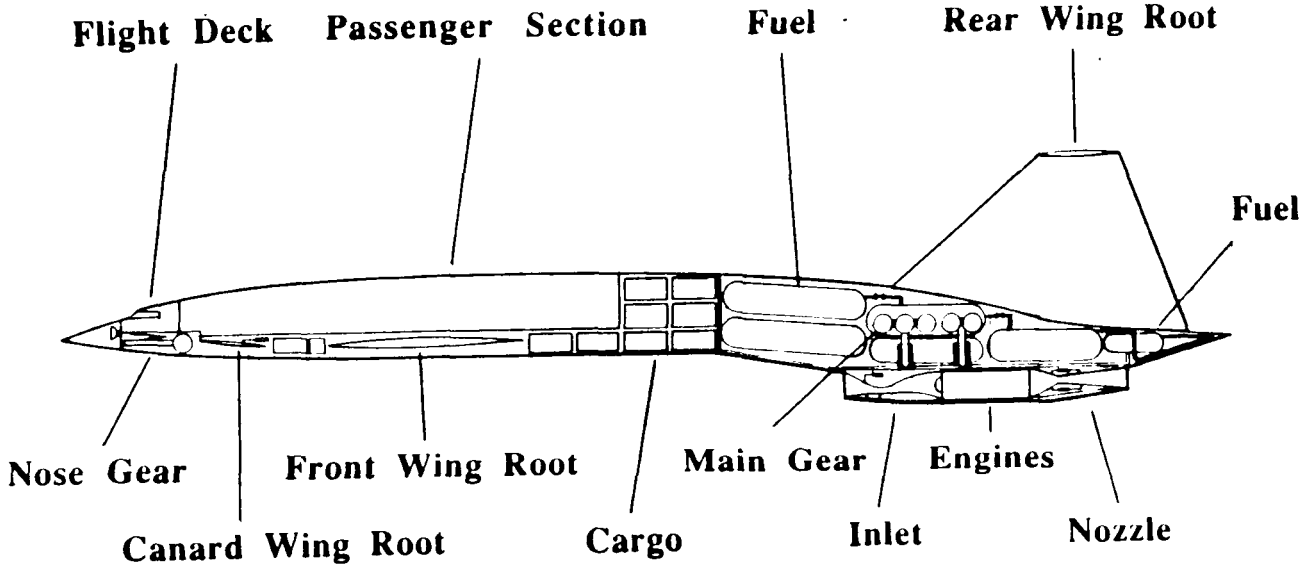

FIGURE 14-1

The number of emergency exits required is not specified by FAR 25. It only states that all the passengers must be able to exit safely within 90 seconds. Other aircraft were researched to determine how many emergency exits would be needed for the Joined Wing. It was decided to use six Type I emergency exits and one Type II emergency exit located throughout the aircraft. There will be one flight attendant seated near each emergency exit to insure proper evacuation procedures are followed. The aircraft will also carry life-vests and rafts since over-water flight will be done. The layout of the escape system is shown in

Figure 14-2. With these design features and properly trained attendants, the 90 second exiting time required by FAR Part 25 can be achieved.

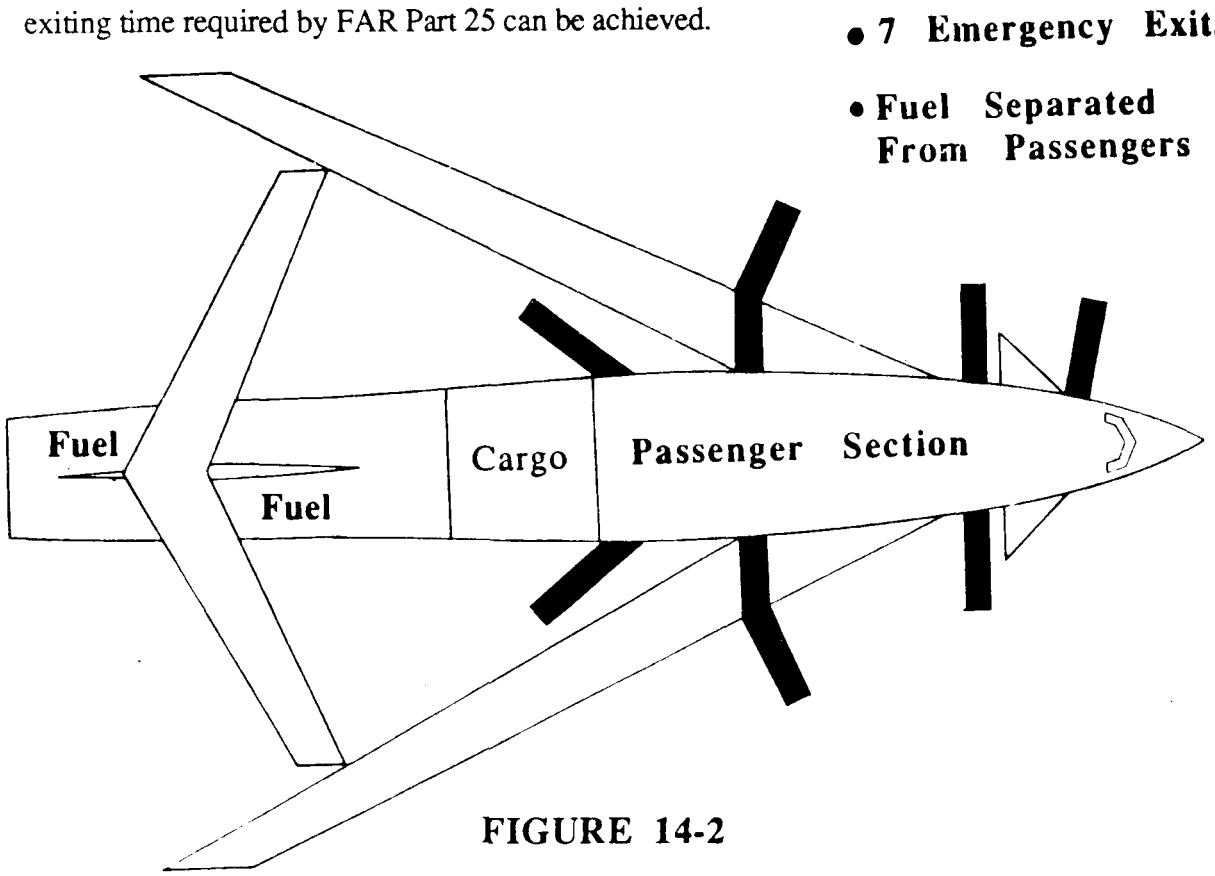

FIGURE 14-2

14.2 Turn-around Time

The Joined Wing HSCT will be able to meet the RFP requirement of a one hour turn-around time. There are three main exits on the left side of the aircraft to allow passengers to load and unload quickly (Figure 14-2). The passengers will be given approximately 20 minutes for each procedure. This leaves 20 minutes for slack and any cleaning that is necessary. The single location of the lavatories and the galleys will help the aircraft achieve a one hour turn-around time. Since the lavatories are contained in one section, the wastes can be directed into one convenient location underneath the section. The food for the galleys is stored in a location directly beneath the galley location and will be brought up, when required, by an elevator type mechanism. Used food containers will be put down in a similar way. While the passengers are loading and unloading, the ground re-supplying takes place. The galley and lavatory storage section is emptied and re-supplied with food and empty waste containers via a pre-readied container which will connect directly to the lavatories and galley. This operation is shown in Figure 14-2. The cargo loading and unloading scheme will also allow a one hour turn-around time. Loading and unloading cargo occurs simultaneously with operation in one direction only. There are two loading

doors and two unloading doors. This system operates as shown in Figure 14-2. The motors to drive this system are ground based so that no unnecessary weight is carried during the flight. Refueling is carried out by several trucks during this time. Simple maintenance is done through access panels located in throughout airplane. The avionics equipment are in modules so that the entire component can replaced quickly and then fixed for future use. With these operating procedures and cooperation from the passengers, the one hour turn-around time requirement can be achieved.

15. References

1. Cuniff, Patrick F., Environmental Noise Pollution, John Wiley & Sons, Inc.., New York, 1977

2. Ott, James, *HSCT Research Defines Weight, Fuel Issues*, Aviation Week and Space Technology, March 28, 1988, pp. 88-90

3. Anon., Information on Levels of Environmental Noise Requisite to Protect Public Health and Welfare with an Adequate Margin of Safety, United States Environmental Protection Agency, March 1974

4. Carlson, Harry W., *Simplified Sonic Boom Prediction*, NASA TP 1122, Scientific and Technical Information Office, 1978

5. Seabass, R. and George, A.R., *Sonic Boom Minimization*, The Journal of the Acoustical Society of America, Volume 51, Number 2, Part 3, 1972, pp. 686-694

6. Morris, John, *An Investigation of Lifting Effects on the Intensity of Sonic Booms*, The Journal of the Royal Aeronautical Society, Volume 64, Number 598, October 1960, pp. 610-616

7. Anon., *HSCT Studies, NASA Contract NAS1-18378, Report to Industry*, Langley Research Center, McDonnell Douglas, August 11, 1987

8. *Code of Regulations: Parts 1 to 59.* Office of the Federal Register, National Check Date Archives and Records Administration, Washington, 1986.

9. Higdon, Archie., Ohlsen, Edward H., Stiles, William B., Weese, John A., and Riley, William F. Mechanics of Materials. John Wiley & Sons, New York, 1985.

10. Houghton, E. L., and Carruthers, N. B. Aerodynamics for Engineering Students. Edward Arnold Ltd., East Kibride, Scotland, 1982.

11. Nicolai, Leland M. Fundamentals of Aircraft Design. METS Inc., San Jose, California, 1984.

12. Pazmany, Ladislao. Landing Gear Design for Light Aircraft. Pazmany Aircraft Corporation, San Diego, California, 1986.

13. Peery, David J. and Azar, J. J. Aircraft Structures. McGraw-Hill Book Company, New York, 1982.

14. Roskam, Jan. Airplane Design Part I: Preliminary Sizing of Airplanes. Roskam Aviation and Engineering Corporation, Lawrence, Kansas, 1985.

15. Roskam, Jan. Airplane Design Part II: Preliminary Configuration Design and Integration of the Propulsion System. Roskam Aviation and Engineering Corporation, Lawrence, Kansas, 1985.

16. Roskam, Jan. Airplane Design Part III: Layout Design of Cockpit, Fuselage, Wing, and Empennage: Cutaways and Inboard Profiles. Roskam Aviation and Engineering Corporation, Lawrence, Kansas, 1985.

17. Roskam, Jan. Airplane Design Part IV: Layout Design of Landing Gear and System , Roskam Aviation and Engineering Corporation, Lawrence, Kansas, 1985.

18. Roskam, Jan. Airplane Design Part V: Component Weight Estimation. Roskam Aviation and Engineering Corporation, Lawrence, Kansas, 1986.

19. Roskam, Jan. Airplane Design Part VI: Preliminary Calculation of Aerodynamic, Thrust, and Power Characteristics. Roskam Aviation and Engineering Corporation, Lawrence, Kansas, 1987.

20. Roskam, Jan. Airplane Flight Dynamics and Automatic Flight Controls. Part I. Roskam Engineering and Aviation Corporation, Lawrence, Kansas, 1982.

21. Roskam, Jan. Methods for Estimating Stability and Control Derivatives of Conventional Subsonic Airplanes. Roskam Aviation and Engineering Corporation, Lawrence, Kansas, 1983.

22. Torenbeek, Egbert. Synthesis of Subsonic Airplane Design. Martinus Nijhoff Publishers, Delft, The Netherlands, 1986.

23. Driver, Cornelius, *Eagle, Supersonic Aircraft Conceptual Design,* Eagle Engineering, Inc., Hampton Division, Purdue University Lecture Series, September 1987

24. Cook, J.C. and Goforth, T., *Seismic and Underwater Responses to Sonic Boom,* The Journal of the Acoustical Society of America, Volume 51, Number 2, Part 3, 1972, pp. 729-741

25. Wilson, Bell B., *Animal Response to Sonic Booms,* The Journal of the Acoustical Society of America, Volume 15, Number 2, Pat 3, 1972, pp. 758-764

26. Nelson, P.M., Transportation Noise Reference Book, Chapter 21, pp. 8-9, 1987

27. Clarkson, Brian L. and Mayes, William H., *Sonic-Boom-Induced Building Structure Responses Including Damage,* The Journal of the Acoustical Society of America, Volume 51, Number 2, Part 3, 1972, pp 742-756

28. Feiler, Charles E., *Noise Reduction*, Aeropropulsion 1979, NASA CP-2092

29. Morgan, H.G. and Hardin, J.C., *Airframe Noise-- the Next Aircraft NOise Barrier*, Journal of Aircraft, Volume 12, July 1975, pp. 622-624

30. Fink, Martin R., *Noise Component Method for Airframe Noise, Journal of Aircraft,* Volume 16, Number 10, October 1979, Article #77-1271R, pp. 659-665

31. Clark, F.G. and Gibson, A., Concorde: The Story of the World's Most Advanced Passenger Aircraft, Paradise Press, Inc

32. Anon., Summary 707-727-737-747 Noise and Emission Reduction Activities, Boeing Commercial Airplane Company, Seattle, Washington, 98124, January 1978.

33. Ronald J. Kochevar, Assistant Airport Manager, Ontario International Airport, Ontario, California, Personal interview 1988

34. Molloy, John K., Grantham, William D. and Neubauer, Milton J., Jr., *Noise and Economic Characteristics of an Advanced Blended Supersonic Transport Concept,* Langley Research Center, Hampton, Virginia, NASA TP2073, September 1982

35. Graf, Donald A., *Hypersonic Civil Transports, Environmental and Economic Feasibility,* Douglas Aircraft Company, McDonnell Douglas Corporation, Long Beach, California, AIAA-87-2952 (presented at AIAA/AHS/ASEE Aircraft Desing, Systems & Operations Meeting, September 14-16, 1987, St. Louis, Missouri)

36. Levenson, G.S., Boren, H.E., Jr., Tihansky, D.P. and Timson, F., *Cost Estimating Relationships for Aircraft Airframes*, Report R-761-PR, February 1972, Rand Corporation, Santa Monica, California

37. Parker, Sybil P., "Methane", Encyclopedia of Chemistry, McGraw Hill, New York, 1983

38. Bunin, Bruce L., *The Required Technology Combinations for High Speed Commercial Aircraft,* Douglas Aircraft Company, McDonnell Douglas Corporation, February 17, 1987, Aerospace Engineering Conference and Show

39. Johnson, F.S., *SST's, Ozone and Skin Cancer,* Astronautics and Aeronautics, Volume 2, Number 7, p. 16, July 1973

40. Beheim, M.A., Antl, R.J. and Poodney, J.H., *Advanced Propulsion, Cleaner and Quieter*, Astronautics and Aeronautics, Volume 10, Number 8, p. 37, August 1972

41. Petrash, Donald A., Diehl, Larry A., Jones, Robert E. and Mularz, Edward J., *Emission Reduction*, Aeropropulsion 1979, NASA CP-2092

42. Stein, Kenneth J., *Ozone Appears Unaltered by Nitric Oxide,* Aviation Week and Space Technology, November 6, 1972, p. 28-29

43. Smetana, Fredrick O. *Computer Assisted Analysis of Aircraft Performance*, McGraw Hill Inc, 1984

44. Julian Wolkovitch, ACA Industries, Torrance, California, Personal interview 1988

45. Hoak, D.E., Ellison, D.E., et. al., USAF Stability and Control DATCOM, Flight Control Division, Air Force Flight Dynamics Laboratory, Wright Patterson Air Force Base, Ohio, 45433

46. Anon., Flight Dynamics Software, given by Paul Lord, Aerospace Engineering Department, California State Polytechnic University, Pomona, Pomona, California 1987

47. Wolkovitch, Julian, *The Joined Wing: An Overview*, ACA Industries, Inc., Torrance, California, AIAA-85-0274, AIAA 23rd Aerospace Sciences Meeting, January 14-17, 1985, Reno, Nevada

48. Wolkovitch, Julian and Montalbo, Roland, *A Second Look at the Joined Wing*, ACA Industries, Inc., Torrance, California, Symposium on Unconventional Aircraft Concepts, April 24, 1987, Delft, Holland

49. Spearman, M. Leroy, Supersonic Stability and Control, NASA Langley Research Center, Hampton, Virginia, Purdue University Lecture Series, November 1987

50. Wolkovitch, Julian, Joined-Wing Research Airplane Feasibility Study, AIAA-84-2471, ACA Industries, Inc., Torrance, California, 1984

51. Perkins, Henry C., *Air Pollution,* McGraw Hill Inc., New York, 1974

52. Morris, S.J., et. al., Douglas Aircraft Company, McDonnell Douglas Corporation, February 17, 1987, Aerospace Engineering Conference and Show, AIAA-87-2938